NORTHWESTERN UNIVERSITY

Excitons in Cuprous Oxide: Photoionization and Other Multiphoton Processes

A DISSERTATION

SUBMITTED TO THE GRADUATE SCHOOL

IN PARTIAL FULFILLMENT OF THE REQUIREMENTS

for the degree

DOCTOR OF PHILOSOPHY

Field of Physics and Astronomy

By

Nicholas Laszlo Frazer

EVANSTON, ILLINOIS

August 2014

ABSTRACT

Excitons in Cuprous Oxide: Photoionization and Other Multiphoton Processes

Nicholas Laszlo Frazer

In cuprous oxide (Cu_2O), momentum from the absorption of two infrared photons to make an orthoexciton is conserved and detected through the photon component of a resulting mixed exciton/photon (quadrupole exciton polariton) state. I demonstrated that this process, which actually makes the photon momentum more precisely defined, is disrupted by photoionization of excitons. Some processes are known to affect exciton propagation in both the pump and exciton stages, such as phonon emission, exciton-exciton (Auger) scattering, and third harmonic generation. These processes alone were not able to explain all observed losses of excitons or all detected scattering products, which lead me to design an optical pump-probe experiment to measure the exciton photoionization cross section, which is $(3.9 \pm 0.2) \times 10^{-22}$ m^2. This dissertation describes the synthesis of cuprous oxide crystals using oxidation of copper, crystallization from melt with the optical floating zone method, and annealing. The cuprous oxide crystals were characterized using time and space resolved luminescence, leading to the discovery of new defect properties. Selection rules and overall efficiency of third harmonic generation in

these crystals were characterized. Exciton photoionization was demonstrated through the depletion of polariton luminescence by an optical probe, the production of phonon linked luminescence as a scattering product, temporal delay of the probe, and time resolved luminescence. The results are integrated with the traditional dynamical model of exciton densities. An additional investigation of copper/cuprous oxide/gold photovoltaic devices is appended.

I can be reached by email at laszlo@laszlofrazer.com.

Acknowledgements

Most importantly, I want to thank my advisor Professor John B. Ketterson for his guidance and support. I also want to thank my other dissertation committee members, Professor Kenneth R. Poeppelmeier, Professor Richard D. Schaller, and Professor Nathaniel P. Stern. Kelvin B. Chang was an excellent collaborator throughout this work, and performed all the floating zone crystallization this thesis relied on. I also want to thank the following people for their contributions to my work in graduate school: Joon Jang, Shahin Mani, Mercouri Kanatzidis, Michael Schmitt, Alyssa Haynes, James Ibers, Brian Odom, Erik Lenferink, Adel Mesbah, Daniel Tice, Constantinos Stoumpos, Leo Ocola, David Czaplewski, Ralu Divan, Liliana Stan, Dan Rosenmann, Karena Chapman, Keith Nelson, Colby Steiner, Patrick Wen, Dylan Arias, Kuei-Fang Hsu, Varada Bal, Jerry Carsello, Carla Shute, Xinqi Chen, Johanna Schwartz, the authors of the references, and the authors of various open source software packages I used.

Table of Contents

List of Tables

List of Figures

CHAPTER 1

Introduction

An exciton is an excited state of a semiconductor. It occurs when the two charge carrying particles in a semiconductor, the electron and the hole, bind together. The binding can be analogous to the way electrons and protons form an atom [9]. Excitons are important to the fields of quantum computation, sensing, photocatalysis, and photovoltaics (A photovoltaic device is addressed in the appendices.).

The primary advantage of an exciton over an atom is that a hole has a much lower mass than a proton, so the exciton is intrinsically closer to the regime where quantum mechanical behavior is important. That relaxes some of the constraints for quantum behavior imposed on atomic systems. In particular, the difficult electromagnetic microKelvin to nanoKelvin cooling techniques needed for atomic physics research can be replaced by simply submerging the host crystal in liquid helium, placing the excitons in thermal contact with the cryogen.

The exciton has an additional practical advantage that, unlike an atom, it does not need to be isolated in a high vacuum system in order to get a reasonable trapping time. However, like positronium, the exciton is composed of a particle and its antiparticle, which tend to annihilate, producing photons. Cuprous oxide is an ideal system for fundamental exciton research because it is one of the few semiconductors that has positive parity symmetry for both the exciton and the valance band (Ag_2O is similar [10]), implying that the exciton cannot decay into a negative parity photon.

There are two loopholes to the parity rule: First, if the exciton is in the correct spin state and has the correct momentum, it can form a new particle. This is called an exciton polariton, which is a quantum superposition of a photon and an exciton. The photon portion of the particle may escape from the cuprous oxide. The exciton polariton forms via a weak quadrupole coupling. Second, the exciton may emit both a phonon (a quantum of sound) and a photon. Despite these decay channels, the exciton lifetime can be as long as 13 μs [11], much longer than the positronium lifetime of 0.1 μs.

This thesis was largely inspired by a diagram [12] which is presented in simplified form in Figure 1.1. In the diagram, three photons are absorbed into an electron/hole continuum state. However, it is unclear if the exciton state is occupied first. Third harmonic generation, where the exciton state does not play any role in the formation of the continuum state, is known and is characterized in detail in Chapter 6. Two photon absorption to produce an exciton state is also well known, with additional investigations ongoing. Breaking of the state prepared by two photon absorption is demonstrated in Chapter 7, leading to the conclusion that both interpretations of Figure 1.1 are correct.

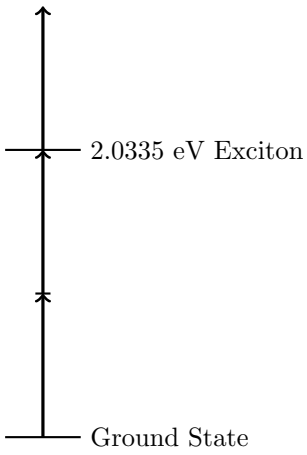

Figure 1.1. An energy level diagram where the excited state may or may not be occupied before the third photon is absorbed into a continuum state.

CHAPTER 2

Background: Excitons and Cuprous Oxide

There are several important and exciting aspects to the mechanics of excitons in cuprous oxide. Many of these have known complications, while other processes are barely understood. Here I try to link together the literature with a common quantum operator language and useful citations, with the reservation that some operators are not understood well enough to be practically useful.

2.1. The Exciton Hamiltonian

$\hat{X}^\dagger$ is the *1s* yellow exciton creation operator. $\hat{X}$ is the annihilation operator. $\hat{E}_K$ represents the exciton kinetic energy. $\hat{e}^\dagger, \hat{e}$ are for electrons, $\hat{h}^\dagger, \hat{h}$ are for holes, $\hat{\gamma}_E^\dagger, \hat{\gamma}_E$ are for photons with energy E, and $\hat{\Gamma}^\dagger, \hat{\Gamma}$ summarize the many phonons [13, 14]. $\hat{Y}^\dagger$ represents energy loss which has not been explained yet, which might be caused by the emission of one or more undetectable phonons. Ry is the exciton Rydberg energy. Some interesting terms in the exciton Hamiltonian are listed below. Not all interactions nor all of their parameters are included. For example, the higher lying exciton states [15] are ignored.

(orthoexciton) $$\hat{H} = (2.033\text{ eV})\left(\hat{X}_O^\dagger \hat{X}_O + \frac{1}{2}\right) + \hat{E}_{K,O}$$

(paraexciton) $$+ (2.021\text{ eV})\left(\hat{X}_P^\dagger \hat{X}_P + \frac{1}{2}\right) + \hat{E}_{K,P}$$

(two-body interactions) $$+ \sum_{\text{spins } i,j} V_{ij} \hat{X}_i^\dagger \hat{X}_j$$

(longitudinal phonon emission) $$- \int_{E_K=E_\Gamma}^{\infty} C\hat{\Gamma}^\dagger \hat{X}_{E_K-E_\Gamma}^\dagger \hat{X}_{E_K} dE_K$$

(longitudinal phonon absorption) $$+ \int_{E_K=0}^{\infty} D\hat{\Gamma} \hat{X}_{E_K+E_\Gamma}^\dagger \hat{X}_{E_K} dE_K$$

(phonon linked decay) $$+ F\hat{\Gamma}^\dagger \hat{\gamma}_{E_X-E_\Gamma}^\dagger \hat{X}$$

(phonon linked absorption) $$+ G\hat{X}^\dagger \hat{\Gamma}^\dagger \hat{\gamma}_{E_X+E_\Gamma} + I\hat{X}^\dagger \hat{\Gamma} \hat{\gamma}_{E_X-E_\Gamma}$$

(light absorption) $$+ \alpha_{E_\gamma} \hat{e}^\dagger \hat{h}^\dagger \hat{\gamma}_{E>2.62\text{ eV}}$$

(two photon absorption) $$+ \beta \hat{X}_O^\dagger \hat{\gamma}_{x\text{ eV}} \hat{\gamma}_{2.033-x\text{ eV}}$$

(electron-hole binding) $$+ J\hat{X}^\dagger \hat{Y}^\dagger \hat{e}\hat{h}$$

(polariton mixing) $$+ K\hat{X}_O^\dagger \hat{\gamma}_{2.033\text{eV}} + K\hat{X}_O \hat{\gamma}_{2.033\text{eV}}^\dagger$$

(photoionization) $$+ L\hat{X}\hat{e}^\dagger \hat{h}^\dagger \hat{\gamma}_{E>\text{Ry}}$$

(two exciton decay) $$+ M\hat{e}^\dagger \hat{h}^\dagger \hat{X}\hat{X}$$

(third harmonic absorption) $$+ N\hat{e}^\dagger \hat{h}^\dagger \hat{\gamma}_{x\text{ eV}} \hat{\gamma}_{y\text{ eV}} \hat{\gamma}_{E>2.62-x-y\text{ eV}}$$

(third harmonic absorption) $$+ P\hat{X}_O^\dagger \hat{\gamma}_{x\text{ eV}} \hat{\gamma}_{y\text{ eV}} \hat{\gamma}_{2.033-x-y\text{ eV}}$$

(strain) $$+ H_d$$

(magnetic) $$+ H_m$$

(electric field gradient) $$+ H_{\nabla E}$$

$$+ \cdots$$

2.2. Interactions

The two-body interaction potential between excitons V_{ij} is not known. There is a detailed proposal available for 2D femtosecond spectroscopy [16] which suggests four wave mixing can be used to perform $\chi^{(3)}$ spectroscopy to identify resonances owing to biexcitons. Estimates of the (probably spin dependent) binding energy range from 3.3 to 13 meV [16–19].

2.3. Phonon Emission

The phonon modes of cuprous oxide have been thoroughly explained [20, 21]. Phonon emission is a crucial cooling mechanism when excitons are produced via electron-hole recombination [22]. The cooling efficiency is dependent on the temperature of the exciton gas. Applying a strain can greatly increase phonon emission [23]. Excitons can decay by emitting a photon and a phonon. There is a usefull spectrum for identifying these processes [24]. Inverse processes are dramatically apparent in the absorption of thin samples [25].

2.4. Light Coupling

Cuprous oxide excitons have strict optical selection rules. A common approach to exciton formation is light absorption (producing an electron and a hole which are not bound) followed by the electron-hole binding process, where energy is lost through a mechanism which has not been studied in detail. Orthoexciton-polariton dispersion has been described [26], including magnetic field [27]. Two photon absorption is illustrated

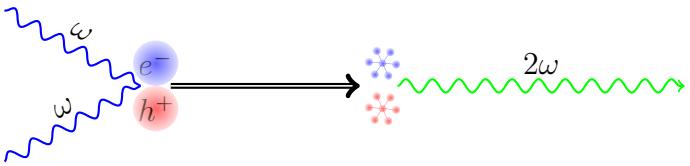

Figure 2.1. Two photon absorption can produce orthoexcitons. Depending on the absorption selection rules, a spin flip may be required to form a polariton subsequently. The blue wavy lines represent the absorbed photons. The circles represent the electron and hole. The stars represent the annihilation of the electron and the hole. Finally, the green wavy line represents polariton luminescence. The superposition of the exciton state and the luminescence to form a polariton is not illustrated.

in Figure 2.1. The strain, spin, momentum, and polarization dependent selection rules for two photon absorption and the related state symmetries have been well described [28]. The two photon absorption coefficient β, which governs the efficiency of two photon absorption βI^2, has been measured [29]. The two absorbed photons need not have the same wavelength [30]. There is a theory and some applications of the dependence of two photon absorption on the spectral phase [31, 12]. One dramatic demonstration that two photon absorption is not like second harmonic generation is two photon coherence storage [8]. There is also a polariton associated with the transition between the *1s* yellow orthoexciton and *1s* blue orthoexciton [15].

Symbol	Value (eV)
a	-2.15
b	-0.43
d	0.36

Table 2.1. Deformation Potentials of Cuprous Oxide [1]

2.5. Strain

For a strain tensor $\tilde{\varepsilon}$, and angular momentum operator $\mathbf{L}$, the strain terms of the Hamiltonian are [1, 32]

$$H_d = a \operatorname{Tr} \tilde{\varepsilon} + 3b\varepsilon_{ii} \left(L_i^2 - \frac{1}{3}\mathbf{L}^2 \right) - \sqrt{3}d\varepsilon_{ij} \left(L_i L_j + L_j L_i \right) \tag{2.1}$$

where a, b, c are shown in Table 2.1. This perturbation partially or totally lifts the degeneracy (or near degeneracy [33]) of the orthoexciton. Inhomogeneous strains play an important role in Chapter 5.

2.6. Magnetic Field

Like strain, magnetic field $\mathbf{B}$ can lift degeneracy. The magnetic term of the Hamiltonian in terms of electron/hole masses, g-factors, and spin operators $\mathbf{S}$ is [1]

$$H_m = -\frac{e\hbar}{2m_e} g_e \mathbf{B} \cdot \left(2\mathbf{S}_e - \frac{g_h}{g_e}\frac{m_e}{m_h} \left(2\mathbf{S}_h + \mathbf{L} \right) \right) \tag{2.2}$$

2.7. Auger Processes

The Auger process destroys two excitons, leaving an electron and a hole $\hat{e}^\dagger \hat{h}^\dagger \hat{X} \hat{X}$. The exciton dynamics are described by

$$\frac{dn}{dt} = -An^2 \tag{2.3}$$

Source	Method	Temperature (K)	Photons	Power Density W / m^2	Energy Density J/m^2	A (cm^3ns^{-1})
[34]	Absorptive	2-6	2	$2.5 \cdot 10^{12}$	0.25	$\leq 10^{-17}$
[35]	Temporal	2	1	$2.0 \cdot 10^4 - 2.0 \cdot 10^6$	$5.0 \cdot 10^{-6} - 5.0 \cdot 10^{-4}$	$(7.5 \pm 0.5) \cdot 10^{-17}$
[36]	Temporal	70	1	$1.5 \cdot 10^{11}$	0.9	$6.5 \cdot 10^{-17}$
[36]	Temporal	70	1	$1.2 \cdot 10^{10}$	0.072	$5.5 \cdot 10^{-17}$
[36]	Temporal	70	1	$8.6 \cdot 10^8$	0.005	$4.8 \cdot 10^{-17}$
[37]	Temporal	2	1	$7 \cdot 10^8 - 7 \cdot 10^{10}$	0.002-0.2	None
[38]	Temporal	2-212	1	$9.0 \cdot 10^{11} - 1.8 \cdot 10^{12}$	4.5-8.9	$\frac{(1.4 \pm 0.4) \cdot 10^{-14}}{T}$
[39]	Temporal	0.82	1	$2 \cdot 10^7 - 1 \cdot 10^9$	1-50	10^{-18}
[40]	Temporal	5-80	1	$\leq 1.3 \cdot 10^3$	CW	$3.7 \times 10^{-16} \times 3^{\pm 1}$
[41]	Spectral	2	2	$92 - 6.2 \cdot 10^3$	$1.4 \cdot 10^{-9} - 8.6 \cdot 10^{-8}$	$2.5 \cdot 10^{-16}$
[29]	Z-scan	2	2	$10^7 - 5 \cdot 10^{11}$	$3 \cdot 10^{-5} - 15$	$5.5 \cdot 10^{-17}$
[2]	Theory	0				$8 \cdot 10^{-21}$
[2]	Theory	T				$4 \cdot 10^{-21} T$
[3]	Theory	0				$5 \cdot 10^{-16}$
[3]	Theory	T				$1 \cdot 10^{-17} \sqrt{T}$
[42]	Temporal	3	2	$10^{16} - 10^{17}$	$3 \cdot 10^2 - 3 \cdot 10^3$	n/a

Table 2.2. Auger constants from the literature. The temperature column indicates the cuprous oxide lattice temperature, not the exciton temperature. The "Photons" column indicates the number of excitation photons needed to produce each exciton. Calculations [2, 3] have been disputed [4, 5].

where n is the exciton concentration and A is the Auger constant, which depends on the exciton state.

Table 2.2 lists Auger and related biexciton formation constants from the literature. Most of the literature focuses on producing excitons thermalized to the lowest possible temperature.

CHAPTER 3

Cuprous Oxide Synthesis

Preparing cuprous oxide is a very active field of research. There have been many recent publications on preparing cuprous oxide films [43–55], particles [56–69], wires [70–73], and even nano-"flowers" [74, 75] for applications such as photovoltaics, catalysis, sensing, and energy storage.

The supply of bulk crystals, however, is limited. Most studies rely on samples with undisclosed geological origins. These are typically small and have inconsistent quality. Anecdotally, often [110] faces are exposed. I have often used a sample obtained from the Ray Mine (presumably Arizona) purchased from Arkensone, 1300 E Arapaho Rd, Richardson, TX 75081 because this sample had conveniently exposed [100] faces (Figure 3.1). This is presumably related to its unusual cube-like shape. Northwestern has several other geological samples in stock with varying levels of documentation.

Several things motivate synthesis of cuprous oxide crystals:

- Synthesis is necessary for reproducible results. Acquired samples may include grain boundaries, atomic impurities, inclusions (large impurities), vacancies, and strain. Evaluating these properties is difficult and usually only possible after purchase.
- Reliable supply.
- Enabling destructive experiments.

Figure 3.1. Geological sample from the Ray Mine, before preparation.

- Choice of sample geometries.
- Control over sample properties through defect manipulation.
- Building collaborations with other research groups which need samples.

A desirable cuprous oxide sample

- Has large grains. The impact of grain boundaries is not well understood (though some recently discovered facts will be presented) so it is best to avoid them. "Large" means big enough to cut away, or $\gg 1$ mm in each direction. Single crystals have the additional advantage of well-defined optical selection rules.

- Is phase pure. Cupric oxide (CuO) and copper phases will not have the desired properties.
- Is free of vacancies. Vacancy luminescence [76] is evidence that vacancies have a destructive effect on excitons [77].
- Is free of atomic impurities substituting for Cu or O atoms [78–82]. From a solubility point of view, the primary concern is silver impurities [83]. Impurities are known to cause misleading luminescence [24].
- Is free of strain (Section 2.5).
- Is crystallographically oriented.

Interstitial atoms are not known in cuprous oxide. They are not energetically favored. Dislocations have been reported [84, 85] but their exact nature is unclear.

3.1. Melt Growth

Making large grains is the first challenge to tackle in cuprous oxide synthesis. All other problems are smaller scale and can be corrected after a large crystal has been formed. A widespread approach to large crystal formation is directional freezing of a melt, which tends to prevent the formation of new grains. After greater than thirty trials of directional freezing, we have observed no grain nucleations in cuprous oxide. Based on the phase diagram [86], cuprous oxide melts and freezes congruently (without a change in composition) which makes this process much easier.

3.1.1. Background: Crystal Growth Experiments

It was dramatically demonstrated that growth of cuprous oxide from a crucible (such as Bridgman of Czochralski methods) is difficult [87]. Magnesia (MgO) crystal crucibles have the best performance. Concerns with crucibles include reactivity and impurity uptake.

Crucible free methods have shown success. In early studies, single crystals were only obtained by using a seed and nucleation was sometimes observed [84, 88]. We found a seed was not needed and did not observe nucleation, probably because of superior furnace stability. Each experiment stage was conducted at sub-Torr pressures in oxygen. Our experiments showed use of a filler gas and higher oxygen pressures was desirable. Slower growth rates were reported to be superior, whereas we found no difference, again because of good furnace stability. Phase purity was achieved through annealing. Inclusions have been suggested to be "voids"[84] or "voids" and CuO [88].

A further study [86] identified inclusions such as "pores, dendritic CuO along columnar grain boundaries, polyhedral CuO precipitates and precipitate clusters within the grains" in material which was oxidized but not melted. Melt growth in low oxygen partial pressure was reported to reduce the frequency of defects, but not their variety. An electron micrograph shows a faceted convex cupric oxide precipitate on a melt-grown crystal. We have not been able to reproduce this. Our melt grown crystals have so few defects that they can be difficult to find in an electron microscope, and those which are present are typically concave after crystal preparation. The surface region was reported to be defect free. This is now known to be because of defect sintering with the surface. Annealing in a reduced oxygen environment did not achieve phase purity.

One study had difficulty with samples reducing to copper [89]. No effect for growth rates below 1 cm/hour was found, and no effect for rotation rate was found. Inclusions were systematically and quantitatively demonstrated. Stable growth was not achieved. The best region with respect to macroscopic inclusions was adjacent to reduced copper metal because copper vacancies are filled in by the copper metal. Surprisingly different from our results, the radial distribution of inclusions was constant. An inverse relationship between the number of inclusions and their size was noted. There is a good discussion of facets, which suggests that the [110] face has the lowest surface energy. Grains were found not to evolve during annealing. Strain was related to birefringence and photocurrent, and resistivity was found to increase with annealing [90] because of the removal of vacancies. It was suggested dislocations contribute to exciton dissociation.

A more recent publication compared polycrystalline, recrystallized, and annealed samples [91]. The photograph shown of a sample which has been oxidized into a polycrystal but not melted is partly green, suggesting the presence of malachite $Cu_2CO_3(OH)_2$. The origin of the carbon in the sample is not explained. Potentially the figures are mislabeled. This paper is one of the few to report a *1s* exciton absorption line. My own studies have found that this line is easily observed using a thick sample. Lines up to $n = 10$ are also described, presumably resolution limited. The study reports copper vacancy luminescence, showing no effect for annealing temperature, annealing time, or rotation rate, consistent with our results. Very rapid cooling time increases copper vacancy luminescence. A clear trend of increasing vacancy luminescence with growth rate is shown which does not match our results.

3.1.2. Rod Preparation

Selecting a high purity copper source is important for minimizing vacancies in the final product because certain impurities catalyze vacancy formation when they are located at copper sites of the cuprous oxide lattice [82, 76]. The copper sample must be in rod form for the floating zone method to work. These requirements determine the starting material geometry since high purity copper rods are only available in a few sizes. We performed the crystal growth process with rods from 1 to 10 mm in diameter. Rods must be prepared in pairs: feed rods and support rods.

The first step is machining the feed rod so it can be suspended in the furnace with a wire. I performed this using a lathe. The best method is to create a groove about 5 mm from one end of the rod and about half a radius deep. If too much force is applied to the rod, it may break. I recommend performing the machining on all rods, even though only half of rods will be used as feed rods, because some rods may break in later accidents. If you are growing a lot of crystals, perform the machining on all of them at once to save setup time. It may be tempting to drill a hole in the rod instead of forming a groove. Experience has shown the hole is difficult to make and fills in during oxidation. However, if you are preparing a rod much larger than 10 mm in diameter, drilling is the recommended method of creating a place to attach the wire. Cuprous oxide cannot be machined after oxidation because it is brittle.

After machining, the dirty rods are washed, etched in 1 M HCl for one hour to remove surface contaminants, and washed again. They are oxidized at 1045 °C for three days in air (Figure 3.2). The furnace ramp rate is 5 °C/minute for convenience. During oxidation, the sample is supported with copper foil, which is later removed. This prevents contamination

from a crucible. The copper foil is supported by inverted alumina (Al_2O_3) boats. Use of other ceramic boats may produce entertaining but totally useless results because the copper will react with the boats.

The purpose of oxidation is to reduce the thermal conductivity of the sample. Our experiments show crystal defects are not reduced in the final product by starting with a better-oxidized material [76]. In other words, cuprous oxide melt reaches equilibrium rapidly. Equilibrium does not imply stoichiometry at high temperatures.

The 1 M HCl acid etch is repeated for another hour, removing a CuO layer. The sample was then ground with sand paper. The oxidized rod is about 95% the density of Cu_2O. It is noticeably larger than the unoxidized starting material. From the point of view of crystal growth, the oxidized rods are an excellent high density starting material, but from an optical properties point of view the density is very low.

3.1.3. Floating Zone Method

This step was performed by Kelvin Chang using a Crystal Systems CSI FZ-T-10000-H-VI-VP with four 300 W tungsten halide incandescent lamps. Each sample is melted and frozen using radiative heating. The method is very well controlled, but the only *in situ* measurements possible are photography/video through a small aperture because of the high reactivity of the sample. Our standard recipe used feed and seed rods rotating at 7 rpm in opposite directions, and growth at 7 mm/hour. These parameters had no effect on copper vacancy luminescence [76]. Other parameters should be chosen based on the goal.

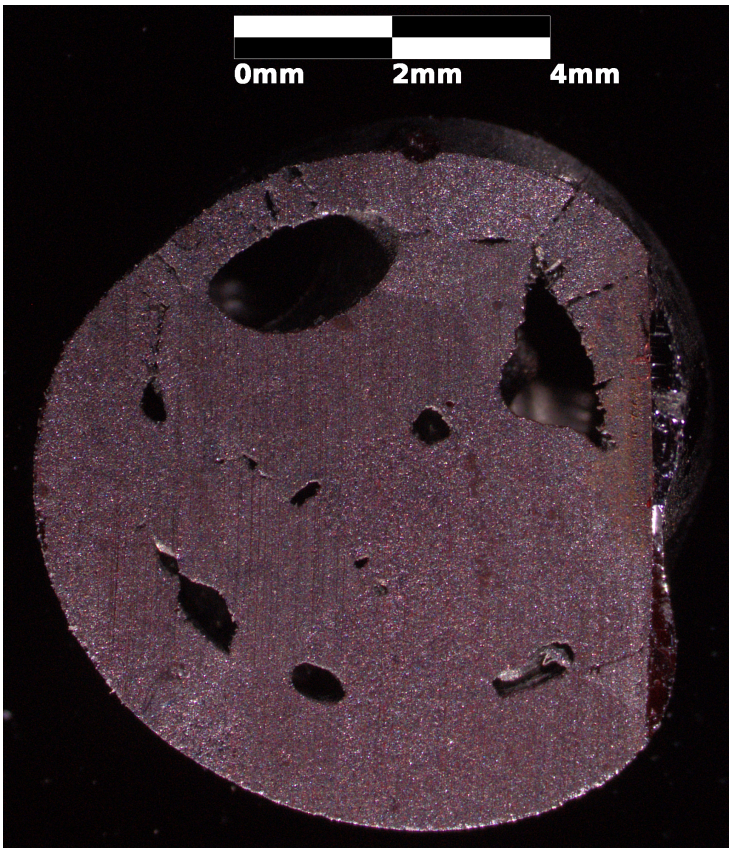

Figure 3.2. A radial cross-section of a thermally oxidized copper rod. This sample has not been polished. There are multiple voids. These samples are typically polycrystalline, though grains are not visible without polishing.

3.1.4. Floating Zone Variables

These aspects of floating zone crystal growth were exhaustively explored:

- Growth Rate
- Rotation Rate
- Lamp Power
- Oxygen Partial Pressure at One Atmosphere
- Starting Copper Purity

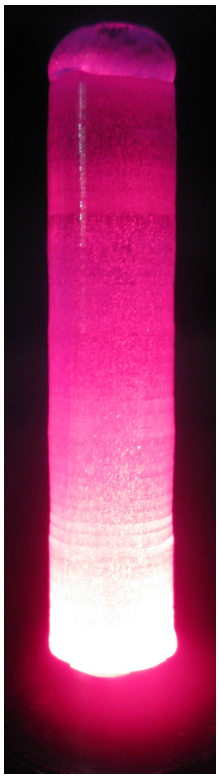

Figure 3.3. The recommended method of making dramatic images of floating zone grown cuprous oxide crystals is to cut one end flat and shine a fiber light into it. The cuprous oxide crystal acts as a waveguide. This sample has growth rings on the surface and inclusions in the interior. It was prepared from 99.9% purity 6.35 mm diameter Cu grown at 10 mm/hour in nitrogen. The feed rod was rotated at 14 RPM and the seed rod was rotated at 15 RPM. Growing in an oxygen free environment does not produce the highest quality crystal, but it does eliminate cupric oxide from the surface, leading to an attractive image of the as grown sample.

- Repeated Melting Cycles

3.1.5. Surface Tension

Surface tension must counteract gravity in order for the floating zone method to work. Laplace wrote in his *Mécanique Céleste* that the static equilibrium relationship between surface tension and gravity is

$$\frac{1}{P(x,z)} + \frac{\sin\phi}{x} = 2 + \beta z \tag{3.1}$$

where P is the radius of curvature of the interface at a given point, $\phi(x)$ is the angle between the tangent of the interface and the horizontal (x) axis,

$$\beta = -\frac{g\sigma b^2}{\gamma}, \tag{3.2}$$

the negative sign is for a hanging (pendant) drop, g is the gravitational acceleration, σ is the difference in density between the material and the medium, $b = P(x = 0)$, and b is the unit of length. Cylindrical symmetry is used. The quantity of interest, the surface tension, is denoted γ. In principle, an image such as Figure 3.4 could be used to determine the surface tension of liquid cuprous oxide, but in practice the lighting conditions are poor when imaging molten cuprous oxide, so the interface curvature cannot be adequately determined. Extreme precision and a numeric solver [92] are required to get an accurate measurement with this method.

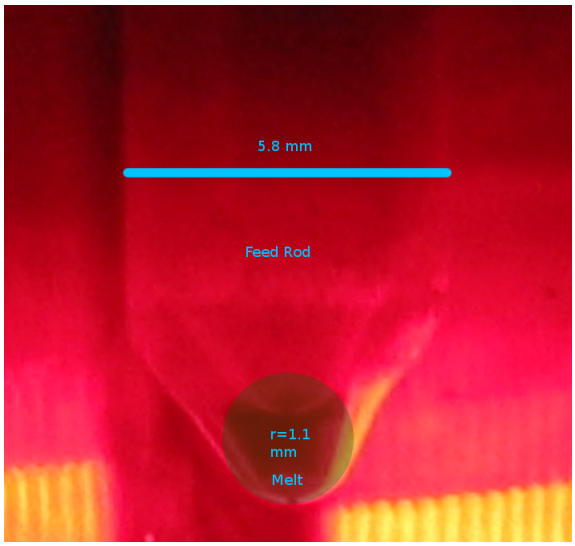

Figure 3.4. An illustration of a Cu_2O pendant drop with b marked by a circle.

The minimum required surface tension for a floating molten zone has been determined numerically [93] to be

$$\gamma > 2\rho g x^2 0.65^2 \tag{3.3}$$

Where $\rho = 6800$ kg/m^3 is the material density, g is the acceleration due to gravity, and $x = 0.0035$ meters is our room-temperature sample radius. Thermal expansion is assumed to be negligible [94–97]. It was determined experimentally that no stable zone can be formed in 60% oxygen, but a zone can be formed with care in 50% oxygen, with the concentration measured using flow rate meters. The total pressure was one atmosphere. This indicates that at these oxygen pressures the surface tension is about 700 mN/m. This is a high value compared to room-temperature liquids.

No literature data on the surface tension of cuprous oxide is available. Molten copper metal has a very high surface tension which decreases rapidly with oxygen gas pressure

[98]. This is consistent with our results if the copper/oxygen phase transition has no impact on surface tension. Surface tension is temperature dependent, and temperature varies throughout the melt in a floating zone. It is desirable not to heat much above the melting point because in most materials this will lower the surface tension. It also increases the weight of the molten region. Centrifugal forces in the molten zone are negligible compared to gravitational and surface tension forces.

We eventually concluded that crystal growth in an oxygen rich environment is advantageous [76]. The decrease in surface tension with higher oxygen partial pressure limits how oxygen-rich the environment can be for a given crystal rod radius. However, this is not a problem because

- Increasing the oxygen partial pressure shows diminishing returns.
- Annealing is a more effective, if slower, method of manipulating vacancies.

Growing rods of different radii and determining the failure oxygen partial pressure could be a way to measure the relation between surface tension and oxygen pressure in more detail. Small diameter rods can be prepared in a more oxygen rich environment, but I think it is more advantageous to stick to samples with a radius of a few millimeters for ease of handling.

3.2. Polishing

Preparing a high quality surface is crucial for conducting optical measurements of a bulk material, or for performing electron beam lithography. For optical measurements, it is desirable that nearly all the incident light is transmitted. Considerable reflection owing

to the high index of refraction of cuprous oxide [99] limits optical coupling in the absence of a dielectric antireflective coating.

For electron beam beam lithography (Appendix A), sample flatness must be good compared with the resist thickness ($\approx$ 100 nm). This ensures a uniform film of resist is created during spin coating. In addition, during beam writing on the resist, it is necessary to maintain focus of the electron beam on the resist. The shape of the sample must be compensated for. The curvature of samples I prepared was adequately small for creating devices of the scales I was interested in without any correction. However, the curvature is not zero. To evaluate curvature of a sample polished on both sides, I recommend using Newton's rings. Place a sample in a microscope with transmission lighting. If the surfaces of the sample are not perfectly parallel, rings will appear from interference between transmitted light and light which has been repeatedly internally reflected. Traditional Newton's rings are colorful or require a monochromatic light source. Cuprous oxide is an optical long pass filter. Combined with the spectral response curve of a human eye or CCD camera, the light measured is approximately monochromatic. A particularly severe (but barely visible) case of Newton's rings can be seen in the the lower left of Figure 3.9. As the right hand side shows, not all samples exhibit rings, indicating curvature less than 10^{-4}.

Mostly I learned the polishing process from Shahin Mani. Good quality results can be consistently produced with practice. Results are not precisely reproducible. They seem to depend on wear on the polishing materials. I have not yet seen a perfectly flat polished surface. Acid based polishing procedures also exist [85].

3.2.1. Polishing Supplies

- Saw mount such as an aluminum block.
- 1 inch diameter aluminum rod polishing mount.
- 1 inch inner diameter polishing ring to keep the mount perpendicular to the polishing wheel.
- Washable marker.
- SPI Crystalbond 509. One package will last many years.
- Blunt tweezers.
- Safety glasses.
- Gloves.
- Tech Cut 5 Saw.
- Diamond metal bonded wafering blade 6"x0.020"x1/2" #60-20080.
- Grit sheets, ANSI P800, P1200 and P2500 (22, 15, and 10 microns) such as Buehler 305232025. The P2500 is consumed rapidly.
- Buehler MicroCloth. These have a finite shelf life.
- Buehler 1 micron MetaDi diamond suspension 406530.
- Buehler MetaDi Fluid Polishing Extender 155001.
- Polishing wheels.
- Pressurized gas.
- Upright stereomicroscope with a large vertical travel.

3.2.2. Recommended Polishing Protocol

(1) Determine the geometry desired for the final sample. I recommend approximate 1 mm thick wafers. Crystallographic orientation can be determined using a known seed, with facets [89], or with Laue X-ray diffraction. I used Laue. The accuracy is about 5°, which is adequate since optical selection rules typically behave like $\cos^2\theta$ and are therefore insensitive to small deviations from zero. Instructions from here assume there is an exposed face with the desired orientation.

(2) Allow a hot plate to heat to a high temperature (at least 15 minutes).

(3) Place a saw mount on the hot plate.

(4) Add a small chip of SPI Crystalbond 509 to the mount face. Do not drip any down the sides of the mount. Very thick samples will need much larger quantities of Crystalbond to ensure they do not shear off later.

(5) Once the Crystalbond has just melted, place the sample flat-face down on the Crystalbond using tweezers. Gently press down.

(6) Use tongs to lift the aluminum mount and place it in a beaker of water. If many samples are being processed at once, flow water through the beaker. Do not submerge the sample or Crystalbond.

(7) Once the mount is cool, inspect the sample. If the sample is thin, the contact region must be completely coated with Crystalbond or the sample will shatter later.

(8) Place the saw mount in the Tech Cut 5 vice. In the past, a South Bay Technologies diamond wire saw was used. The Tech Cut 5 is much faster and does not require expensive replacement blades. It has slightly higher wastage.

(9) Cut the sample with the diamond metal bonded wafering blade at 0.5 inches per minute with 2000 RPM.

(10) Mount the sample again on the polishing mount. Ensure Crystalbond is not preventing the mount from passing through the polishing ring.

(11) Label the mount with a washable marker. Labels can be scrubbed off with ethanol. Do not use a VWR lab marker.

(12) Inspect grit sheets and polishing wheel for damage, debris, or excessive wear.

(13) Grind the sample with grit sheets on a wheel in flowing water. Use the polishing ring to keep the sample square. Start with coarse grits and work towards fine grits. Usually only P1200 and P2500 are required. If the sample is very rough, use a coarser grit. Grind slow and briefly with coarse grits. Faster speeds are okay for fine grits. Grind until the sample surface is uniform. This will remove any cupric oxide or excess Crystalbond from the face. If you do not grind long enough, polishing will fail. Coarse grit sheets never wear out. P2500 grit sheets wear out rapidly. If progress is not being made, back track to a coarser grit.

(14) Dry the sample with pressurized gas. A blow dryer intended for hands will be ineffective because cuprous oxide is strongly hydrophilic.

(15) Inspect the sample with a microscope. At 40X you should see a gray surface with only very slight scratches. Inclusions in the sample may be apparent at this point. Further work will not remove them, but grinding more will remove scratches.

(16) Inspect the MicroCloth. It should be fuzzy and free of bubbles or dents.

(17) Put the MicroCloth on a wheel. Apply a few drops of MetaDi. This substance acts like a lubricant. It prevents wear on the pad but it can also wash away diamond suspension if used excessively.

(18) Apply diamond suspension. The MicroCloth must be kept moist throughout polishing to prevent destruction of the MicroCloth and/or sample.

(19) Spread the suspension with the polishing ring.

(20) Insert the polishing rod into the ring and polish the sample on the MicroCloth. A high polishing speed may be used. The diamond suspension must be maintained. Polishing takes 6 ± 3 minutes. Troubleshooting:

- Black stuff or fiber on the sample: Wash the MicroCloth with water and dry it. If this continues, replace the MicroCloth.
- Scratches will not go away: Return to grinding with grit sheets.
- Excessive friction: Add diamond suspension or a very small quantity of MetaDi Fluid Polishing Extender.
- Streaks/Rings: Wash sample with soap and water.
- Sample breaks: Sample not mounted flat, insufficient Crystalbond, worn out polishing materials, or sample is less than 100 micrometers thick.

(21) Wash the sample with soap and water.

(22) Dry the sample with pressurized gas.

(23) A quick first inspection can be performed by examining the reflection of a ceiling light off the sample.

(24) With the microscope, it should be easy to see the red interior of the sample. Keep in mind the polished surface is highly reflective.

(25) Rinse the MicroCloth with water, dry it, and store it.

(26) Remove the sample by returning it to the preheated hot plate. After a few minutes it will easily lift off. If you are very patient, immersion in acetone at room temperature will also remove the sample.

(27) Polish the reverse side if desired (typically it is).

(28) Sonicate the sample in acetone (removes remaining Crystalbond) and then ethanol. Methylene chloride has also proven helpful for removing particularly stubborn dirt, but is more hazardous. Water is not recommended, especially as a final cleaning step, because Cu_2O is strongly hydrophilic.

(29) Place the sample in a sieve and blow dry it. Since it is no longer mounted, be careful not to blow it away. Do not blow on methylene chloride.

(30) Place the sample in a labeled container.

(31) Ensure the hot plate is off.

3.3. Vacancy Luminescence

A vacancy is an atom missing from an otherwise perfect lattice. The possible vacancies in a Cu_2O lattice are copper vacancies V_{Cu} and oxygen vacancies V_O. Copper vacancies can have up to one negative charge. Oxygen vacancies may have up to two positive charges. Luminescence associated with carriers binding to vacancies has been extensively reported. There is an excellent evaluation of how experimental conditions influence luminescence [100].

3.4. Copper Vacancies

My investigation of copper vacancies with Kelvin Chang has been published [76].

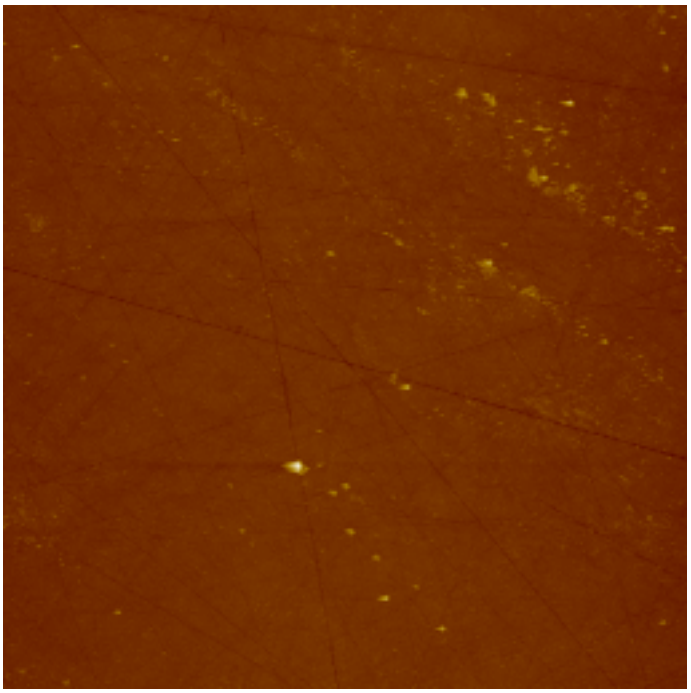

Figure 3.5. AFM image by Varada Bal of polished cuprous oxide. The image is 50 μm wide. The vertical scale is 200 nm. The image demonstrates the sample is quite flat and remaining scratches are shallow.

3.4.1. Introduction

The mechanism for controlling the concentration of copper vacancies V_{Cu} from the copper phase is [86]

$$V_{\mathrm{Cu}}^{\mathrm{Cu_2O}} + \mathrm{Cu}_{\mathrm{Cu}}^{\mathrm{Cu_2O}} + \mathrm{O}_{\mathrm{O}}^{\mathrm{Cu_2O}} \rightleftharpoons \mathrm{Cu}_{\mathrm{Cu}}^{\mathrm{CuO}} + \mathrm{O}_{\mathrm{O}}^{\mathrm{CuO}} \tag{3.4}$$

Each term describes a lattice site. The main symbol describes what occupies the site. The subscript describes what would occupy the site if the lattice were defect free. The superscript describes the phase in which the site resides. For example, the first term describes a vacancy, located at a copper site, in the Cu_2O phase. The final term describes an oxygen

atom, located at an oxygen site, in the CuO phase. Vacancies can be split between sites [82]. In essence, copper vacancies in cuprous oxide can be exchanged for cupric oxide outside cuprous oxide. An alternate representation, in terms of copper vacancy number concentration x, is

$$\mathrm{Cu}_{2-x}\mathrm{O} \rightleftharpoons x\mathrm{CuO} + (1-x)\mathrm{Cu}_2\mathrm{O}. \tag{3.5}$$

Suppose the goal is to eliminate all V_{Cu} from the Cu_2O lattice. According to this equation, the correct way is to drive the formation of CuO. In practice, that means exposing the sample to an oxygen rich environment at elevated temperatures. The temperature must be below the Cu_2O / CuO phase transition temperature for that oxygen pressure, but hot enough to be kinetically relevant [101]. Contrast this with the intuitive, but experimentally incorrect, approach of exposing the cuprous oxide to low oxygen pressures to try and drive it towards stoichiometry.

3.4.2. Methods

Our investigation was primarily driven by cooling protocols. It appears that the history of the samples prior to freezing has no effect on the results. Cuprous oxide was prepared at a high temperature, within the Cu_2O region of the phase diagram [86], then cooled. Time spent in the CuO region of the phase diagram at kinetically relevant temperatures was manipulated. Then the sample was polished and its vacancy luminescence was measured.

Evidence for vacancy removal was initially found by growing the crystal in an oxygen-rich atmosphere, which causes the sample to enter the CuO phase at a higher temperature.

Annealing studies manipulating cooling rate (either at 5 °C/minute, which removes vacancies through Reaction 3.4, or by quenching) were performed to provide better control.

In the floating zone furnace, the temperature profile is determined by

- Radiative heat transfer
- Thermal conduction in the Cu_2O rod
- Translation of the rod through the furnace
- Convection in the Cu_2O melt
- Driven flow in the Cu_2O melt from rod rotation
- Gas convection
- Driven gas flow

Our furnace model has been studied in detail previously [102]. The temperature profile could be numerically modeled in detail [103] if the thermal properties of Cu_2O were well known near the melting point. Annealing is simpler and provides more flexible control over the sample's history. Extended annealing in air within the Cu_2O region of the phase diagram [86] did not remove vacancies (we investigated annealing for one to five days) but gradual cooling through the CuO phase did. Annealing also increases the homogeneity of copper vacancies in the crystal. This is explained in detail in Chapter 5.

3.5. Oxygen Vacancies

Oxygen vacancies are generally less important in synthetic samples than copper vacancies. However, this is sometimes less clear in geological samples, such as the one from the Ray Mine (Figure 3.1). Elimination of oxygen vacancies V_O is obtained through the

reaction

$$V_{\mathrm{O}}^{\mathrm{Cu_2O}} + 2V_{\mathrm{Cu}}^{\mathrm{Cu_2O}} \longrightarrow \text{null}. \tag{3.6}$$

which for oxygen vacancy number concentration y is also written

$$\mathrm{Cu_2O_{1-y}} + 2\mathrm{Cu_{2-y}O} \longrightarrow (3-y)\mathrm{Cu_2O} \tag{3.7}$$

This equation uses y to describe the number of oxygen and copper vacancies eliminated in a 1:2 ratio; it does not describe the overall ratio of vacancies or the total oxygen vacancy concentration. Exhaustion of copper vacancies by this mechanism seems unlikely.

Quenching experiments showed copper vacancy creation is possible [76]. At this point there is no evidence that oxygen/copper vacancy triplets can form spontaneously by the reverse of Equation 3.6.

Another hypothetical possibility is

$$(1+y)\mathrm{Cu_2O} \rightleftharpoons \mathrm{Cu_2O_{1-y}} + 2y\mathrm{CuO} \tag{3.8}$$

This is quite similar except that Reaction 3.4 has been used to exchange V_{Cu} for CuO, which is less mobile. It seems much more plausible that this reaction is reversible.

Oxygen vacancy luminescence measurements indicate oxygen vacancies are rapidly eliminated by annealing at 1045 °C in air within the $\mathrm{Cu_2O}$ region of the phase diagram [86]. They can return if the sample is cooled slowly through the CuO phase. Samples grown in higher oxygen gas concentration environments have increased oxygen vacancy luminescence. This is opposite of the effect for V_{Cu} and much weaker. Interestingly,

oxygen vacancy formation on cooling in a furnace is suppressed if the annealing stage is extended. About four days is sufficient. I attribute this result to removal of an unknown defect through annealing. This defect apparently catalyzes V_{O} formation.

Since V_{O} are typically uncommon, their luminescence was studied using a HeNe pump laser at liquid nitrogen temperature [100]. In this case, the laser is selectively absorbed by oxygen vacancies [104] rather than producing free electrons and holes.

3.6. Inclusions

Cupric oxide is pervasive in thermally oxidized copper metal. In such samples, depending on the thickness there may be enough present to make the cuprous oxide opaque. There can also be cavities.

3.6.1. Removal Through Melting and Annealing

Since cuprous oxide is produced from oxygen in its environment via

$$4\,\mathrm{Cu} + \mathrm{O_2} \longrightarrow 2\,\mathrm{Cu_2O} \tag{3.9}$$

It may be intuitive to try and take cupric oxide which may have formed via Reaction 3.4 or

$$2\,\mathrm{Cu} + \mathrm{O_2} \longrightarrow 2\mathrm{CuO} \tag{3.10}$$

and remove it by using the reaction

$$4\,\mathrm{CuO} \longrightarrow 2\,\mathrm{Cu_2O} + \mathrm{O_2} \tag{3.11}$$

Figure 3.6. A SEM image of an inclusion in the thermally oxidized support rod of a longitudinally sliced and polished floating zone grown Cu_2O rod. The floating zone grown region is essentially featureless in the SEM. This inclusion is a cavity rather than CuO, though it may have a CuO surface layer. Notice the fine faceting on the interior of the inclusion.

This works very well in melt owing to the rapid mixing of the material (Figure 3.7) and elimination of grain boundaries that reduce the surface energy of inclusions (Figure 3.8) but does not totally eliminate cupric oxide because of the action of Equation 3.4 during cooling. In a mostly oxidized solid sample, Equation 3.11 merely converts the

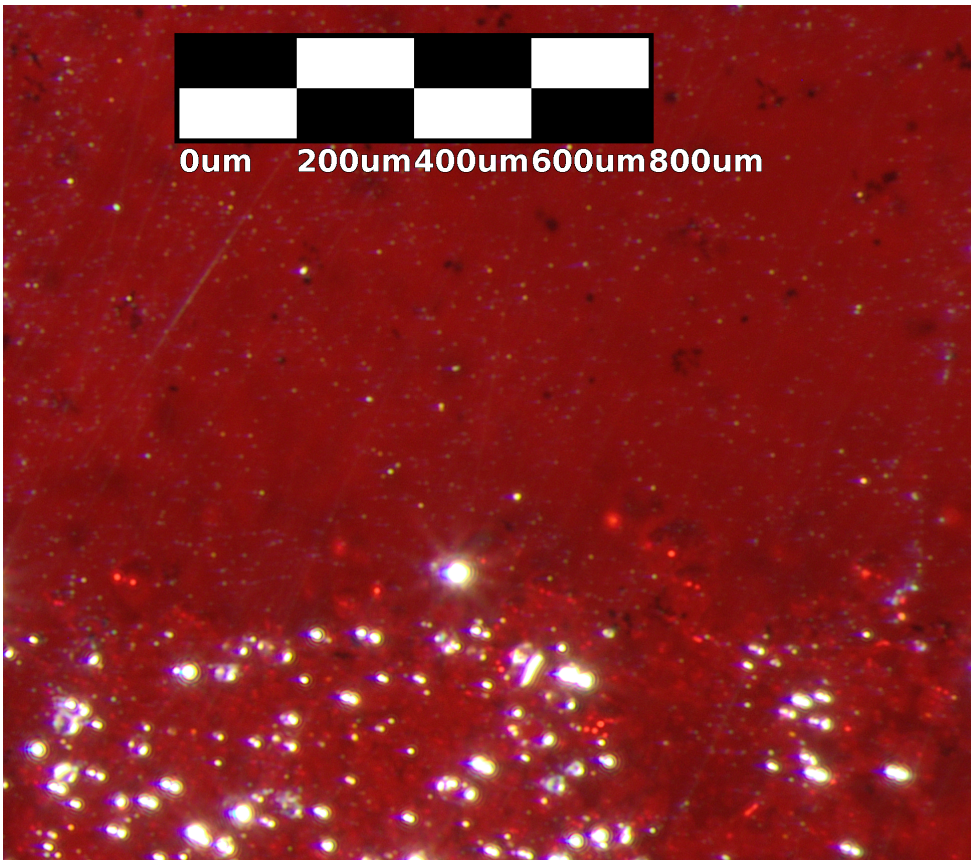

Figure 3.7. Melting and recrystallization dramatically improves the phase purity of cuprous oxide. This microscope image shows the boundary between the region of a rod which was melted (top) and its unmelted support (bottom). Dark regions are CuO in the bulk. Light regions are surface defects, which scatter light. Surface defects in the unmelted region are much more prevalent than even bulk defects in the previously melted region.

excess oxygen into a gas-filled cavity. In order to produce phase-pure cuprous oxide, it is necessary to separate out the phases.

The method we developed to perform the phase separation is to cool samples with a thickness $\lesssim$ 1 mm in air from 1045 °C at 5 °C per minute. This gradual cooling rate allows Equation 3.4 to operate close to equilibrium. Equilibrium means the V_{Cu} diffuse to the location where CuO will have the lowest energy before undergoing Reaction 3.4.

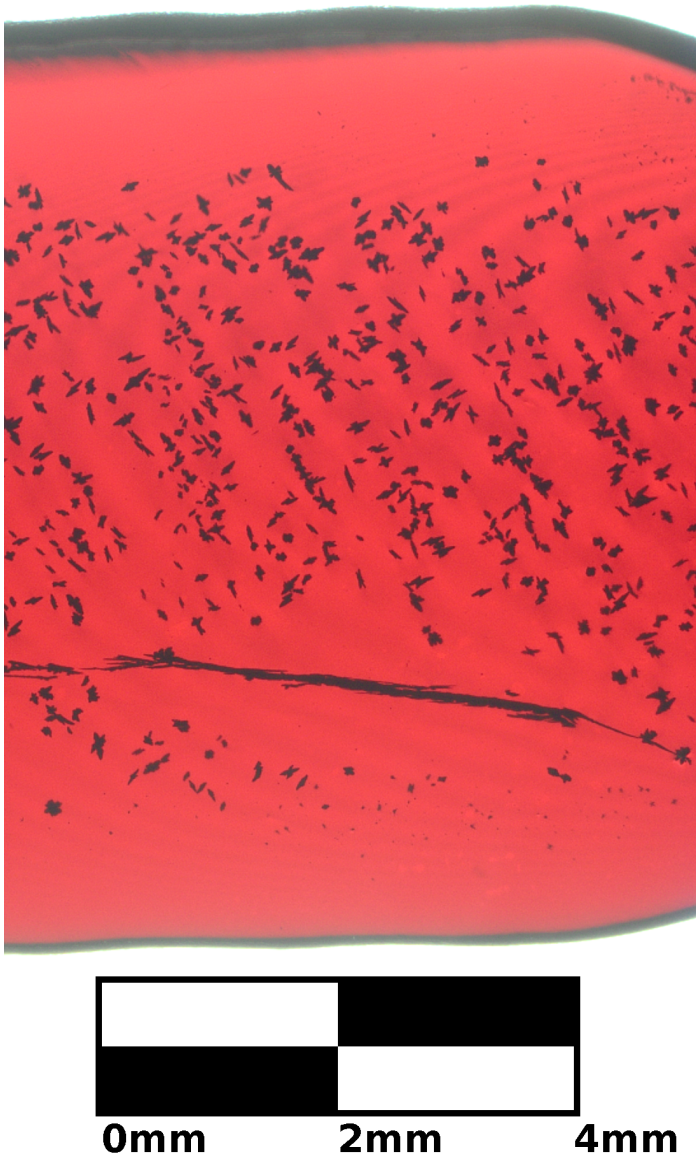

Figure 3.8. Inclusions accumulate along grain boundaries. The area around the grain boundary has been cleared of inclusions. Grain boundaries are occasionally barely visible on the surface of as-grown crystals. Grain boundaries are easily spotted during grinding, and can be reliably verified with Laue diffraction. Crystals grown from a monocrystal seed are grain boundary free.

Meanwhile, existing interior CuO is eliminated via the reverse reaction. The end result is that all CuO is at the surface, where it can easily be removed through the polishing process.

Figure 3.9 shows that annealing improves the inclusion volume fraction in the interior from 0.28 ± 0.02 to 0.00051 ± 0.00007, which is *a factor of* 540 ± 70 *improvement* in this particular sample. This is on top of the previous improvement owing to recrystallization. CuO quantities in annealed samples are too small to measure with powder diffraction, but they can be measured very accurately using a transmission microscope. The inclusion fraction in annealed samples does vary. It is quite costly to collect statistics on this variation, but in all cases observed the inclusion fraction is greatly improved.

Samples that are annealed and rapidly quenched show tiny, widespread CuO inclusions which have not had sufficient time to aggregate, except for a small area near the surface. A quenched sample is shown in Figure 3.9. Unlike other samples (Figure 3.8), quenched samples are transparent near grain boundaries but opaque in the bulk.

3.6.2. Rotation Rate

In floating zone crystal growth, the molten floating zone is stirred by the counter-rotation of a solid support rod and a solid feed rod. Faster rotation decreases thermal gradients and improves melt homogeneity. Inclusions form on cooling into the cupric oxide region of the phase diagram [86], rather than during crystallization. They are never in contact with the melt. Nevertheless, faster rotation increases inclusion homogeneity and volume fraction.

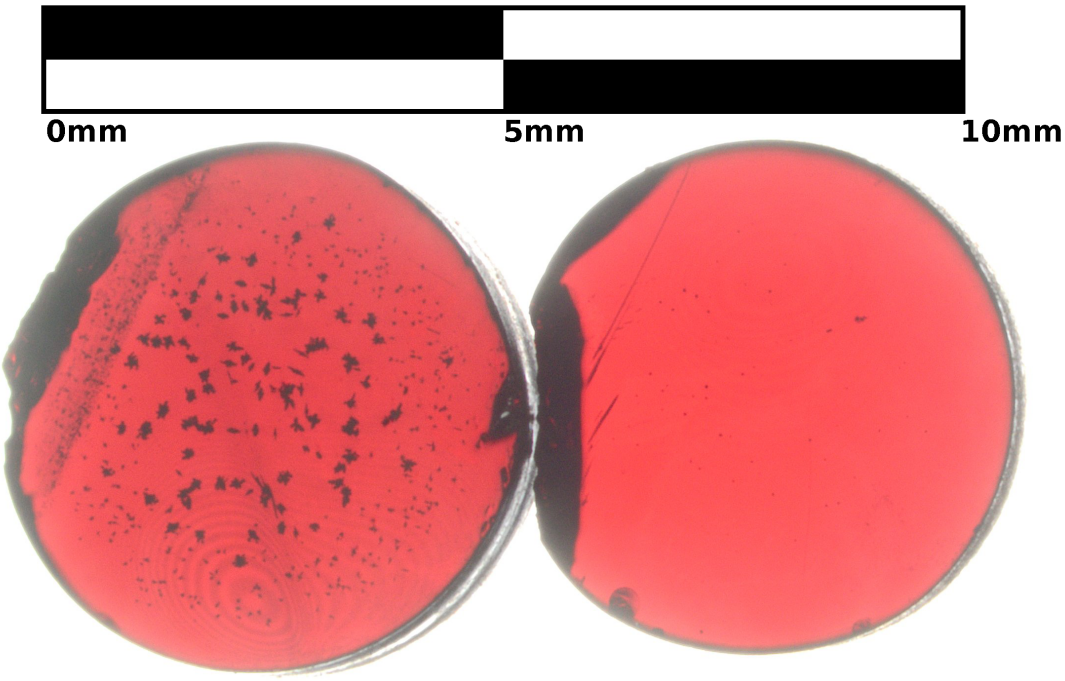

Figure 3.9. Left: Unannealed, floating zone grown sample. Right: Sample annealed at 1045 °C for five days with a 5 °C per minute furnace ramp rate. Black regions on the right sample are remaining surface defects. These samples were taken from the same rod. Vacancy homogeneity is described in Chapter 5.

Cuprous oxide was grown with a counter-rotation rate of 70 rpm per rod and also at 7 rpm per rod. A vertical slice through the approximate center of the rod was examined with threshold particle analysis [105]. There are 2.2±0.3 times as many inclusions in the region grown with faster rotation ($p<0.00001$, one tailed Exact Poisson Test). Inclusions are 1.9±0.2 larger in volume when the slower rotation rate is used ($p<0.05$, two sample t-test). This does not make up for the difference in the number of inclusions; the volume fraction of inclusion is greater for fast rotation. Due to sintering at the surface and slower cooling in the interior, most of the included cupric oxide is near the center of the rod. However, they are spread out 20% further radially when the rotation rate is faster

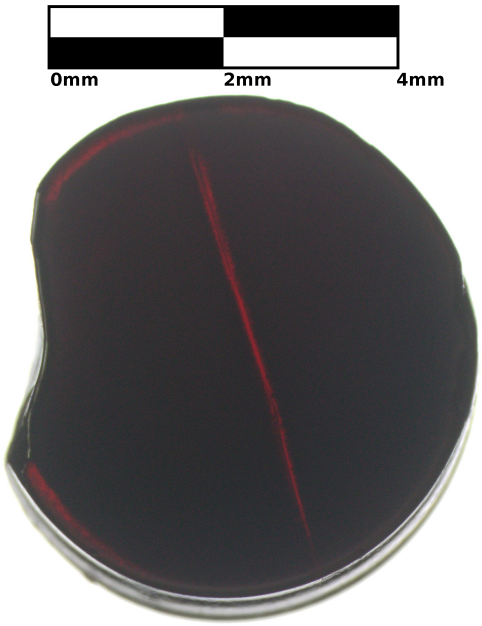

Figure 3.10. A sample which was annealed for one day and quenched. This sample is comparable to those in Figure 3.9. The sample is opaque because copper vacancies convert into small CuO inclusions on quenching.

($p<0.01$, F-test). I recommend using a slow rotation rate to minimize the volume fraction of the inclusions and make the inclusions more concentrated so they are easily avoided. Fast rotation may cause collapse of the molten zone if the rods are poorly aligned.

3.7. Impurities

Density functional theory shows that impurities substituted for Cu can change the vacancy formation energy of V_{Cu}. The results depend on the substituted atom and the defect configurations, and result in both positive and negative formation energies [82].

Cuprous oxide grown from copper purchased with various purity ratings [76] showed that higher purity copper led to decreased copper vacancy luminescence. The homogeneity of the samples also improved with purity. A repeated melting cycle had no effect,

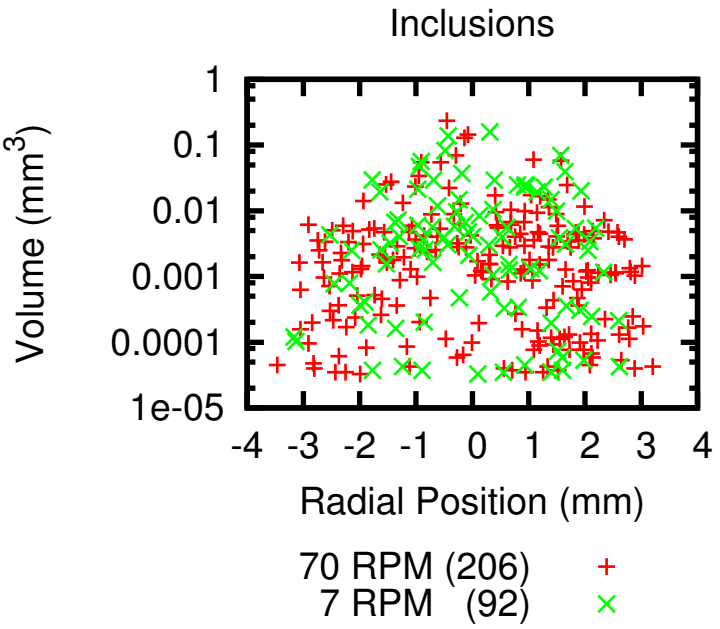

Figure 3.11. Rotation rate during floating zone crystal growth changes cupric oxide inclusions.

suggesting that the floating zone purification effect was not important. The nature of the impurities was not known, but the solubility of various atoms in cuprous oxide has been studied [83].

Some geological samples show "bound exciton" luminescence which has been attributed to impurities [106]. It is not known which impurities are responsible, and synthetic samples do not show the luminescence. This phenomenon is undesirable since it indicates a reduction in the exciton lifetime.

3.8. Raman Spectroscopy

3.8.1. Introduction

Dawson et al. describe the Raman spectrum of cuprous oxide [107]:

> We believe the bands at 148 and 610 cm^{-1} ... appear because of a selection rule breakdown [owing] to nonstoichiometry.

They theoretically argue these modes are "silent in a perfect lattice." This work determines that the bands are not caused by vacancies.

3.8.2. Method

A cuprous oxide crystal was grown in an optical floating zone furnace. During growth, the oxygen concentration surrounding the melt was changed. This produced a sample with spatially varying stoichiometry. I carried out Raman measurements on this sample to determine if they were related to the stoichiometry.

The relative copper vacancy density along the longitudinal direction was determined by exciting with a 532 nm laser and detecting luminescence integrated from 909-920 nm. The Raman spectrum was measured with a confocal Raman spectrometer using 514 nm excitation and a 100X objective. The confocal system was focused on the surface of the sample at each location to reduce laser beam absorption.

3.8.3. Results

A typical Raman spectrum is shown in Figure 3.12. It is similar to references [107, 108], but different from [109, 110], which show much sharper lines. Since floating zone refined samples are much more stoichiometric than the unrefined sample used by [107] it was surprising that the 610 cm^{-1} line was easily detected. However, the 148 cm^{-1} line was inconsistently detectable.

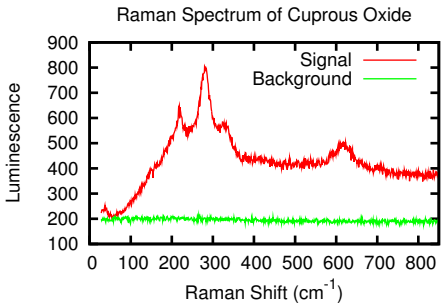

Figure 3.12. A typical Raman spectrum.

	Luminescence	148 cm^{-1}	610 cm^{-1}
Luminescence		-0.3	-0.5
148 cm^{-1}	.4		**0.95**
610 cm^{-1}	.2	**.0003**	

Table 3.1. Top Right: Correlation coefficients between Raman lines. Bottom Left: p-Values for the correlation coefficients. The statistically significant correlation is **bold**.

The Raman spectra was compared with nearby luminescence spectra in an attempt to find a correlation between the two supposed stoichiometry-linked signals. The intensity of the Raman spectrum is sensitive to the accuracy with which the instrument is focused because the laser beam is strongly attenuated by the sample. To eliminate this lurking variable, the Raman lines at 610 cm^{-1} and 148 cm^{-1} were integrated from 600 to 660 and 140 to 170 cm^{-1} respectively, then each was divided by the $2E_u$ line, which was integrated from 210 to 230 cm^{-1}. The $2E_u$ line is strong and is caused by fundamental lattice vibrations; therefore it is a good proxy for the efficiency of signal collection.

There is no significant correlation between the forbidden Raman luminescence and the copper vacancy luminescence. Table 3.1 does show a highly significant correlation

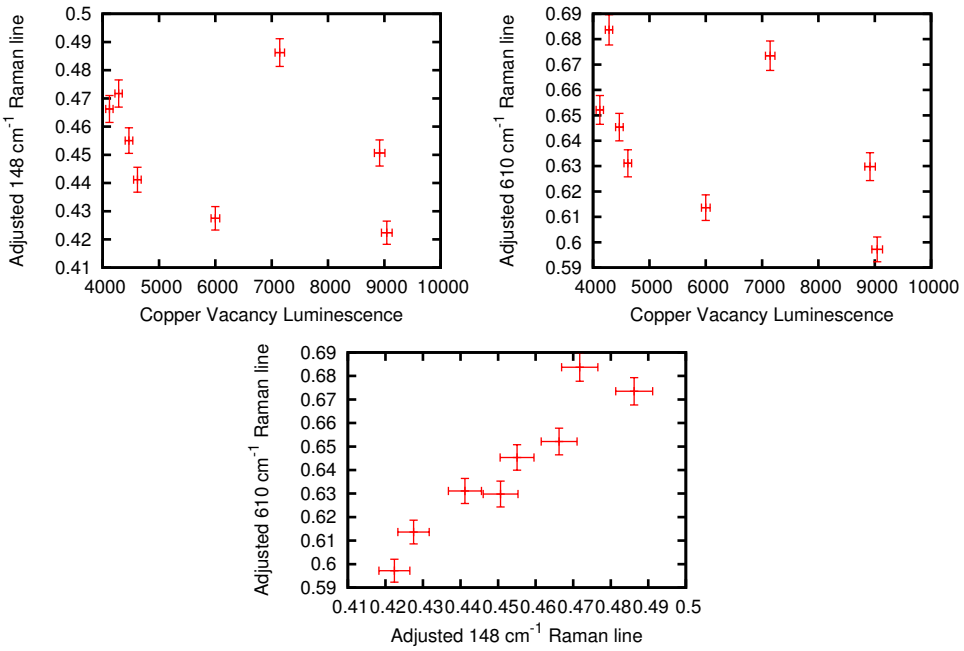

Figure 3.13. Data showing the lack of a relationship between the forbidden Raman luminescence and the copper vacancy luminescence. The units are arbitrary.

between the two forbidden lines; this is expected since they are both normalized to $2E_u$ and likely are caused by similar mechanisms. The data is shown in Figure 3.13.

The data does not support the hypothesis that copper vacancies are the cause of the forbidden Raman luminescence. Oxygen vacancy concentration in this sample should be negatively correlated with the density of copper vacancies (Section 5.3.3). Assuming this negative correlation, our data also does not support the hypothesis that oxygen vacancies are the cause of the forbidden Raman luminescence. Potentially other nonstoichiometries could explain the forbidden lines, such as interstitial or multi-vacancy centers [21].

3.9. Recommended Synthesis Protocol

(1) Obtain high purity copper rods to minimize exciton decay caused by impurities or the associated vacancies. 5 to 10 mm diameter is recommended. The useful length is limited to 100 mm by the design of the furnace.

(2) Perform rod preparation 3.1.2.

(3) Oxidize rod at 1045 °C for three days in air using a 5 °C per minute ramp rate. The ramp rate is for convenience. Rods thicker than 10 mm may require longer. This step reduces the rod's thermal conductivity.

(4) Floating zone grow the cuprous oxide from a single crystalline seed. Use four 300 W tungsten halide incandescent lamps. Grow at 17.5 mm/hour, the maximum growth rate. If a furnace with fewer than four lamps is used, a slower growth rate may be needed. Use a flowing air environment. Adding more oxygen has only negligible benefits and is inconvenient. Use a slow rotation rate such as 7 RPM.

(5) Slice the grown crystal into 1 mm wafers as described in the polishing protocol.

(6) Anneal the wafers on Cu_2O foil supports at 1045 °C for five days. Cool using a 5 °C per minute ramp rate. The cooling rate is important.

(7) Remove CuO from the surface.

CHAPTER 4

Luminescence Lifetime

Time resolved luminescence spectroscopy is a common, extremely sensitive method of evaluating sample quality and determining the exciton lifetime. It does not necessarily identify which defects or intrinsic properties are responsible for the measured luminescence lifetimes. Numerous similar studies on geological samples are listed in Table 2.2. This study is in the time regime where excitons are dilute.

4.1. Methods

Two samples were measured. The first one was prepared from .9999 purity copper precursor. The corresponding data is labeled "4N" in the figures. It was crystallized in air with a growth rate of 3.5 mm/hour and a counter-rotation rate of 7 RPM. It was [100] oriented and annealed for 5 days at 1045 °C with a 5 °C per minute ramp rate. It was also used in Chapter B. The second sample was prepared from .99999 purity copper precursor. The corresponding data is labeled "5N" in the figures. The growth rate was 4.5 mm/hour and the rotation rate was the same. It was [111] oriented and annealed in the same way. Its final thickness was 3.84 mm, which is thicker than the first sample. It was also used in Chapter 7. The difference between the samples which is substantative in this experiment is the copper precursor purity.

Each sample was excited by a Ti:Sapphire regenerative amplifier pumped 2 kHz repetition rate 35 fs OPA with the signal and idler sum frequency mixed to produce 500 nm. 500 nm was selected for two reasons:

(1) 514 to 532 nm is commonly used in the literature. The bandwidth of this laser is broad enough that this is essentially similar to 500 nm.

(2) The wavelength is short enough that no substantial light leaks through the sample from the long wavelength tail of the laser spectrum.

The pump beam was filtered with a BG39 colored glass filter and a 480 nm bandpass filter with a 120 nm width. 180 microWatts of beam power reached the sample in an unfocused, 1 mm diameter beam. The sample was in vacuum at 2.8 Kelvin.

Luminescence was collected in transmission geometry through a spatial filter and 550 nm colored glass long pass filter. Detection was performed with a 150 mm spectrograph with a 50 groves/mm grating and a streak camera with a 50 ns time window. For this time window the time resolution is about 0.2 ns. The spectrograph cannot be calibrated to a precision better than 10 nm and it cannot resolve orthoexciton polariton luminescence from phonon-linked orthoexciton luminescence. These two luminescence lines combined are labeled "Exciton" in the figures. The directly comparable, time averaged luminescence spectrum in Figure 4.1 shows that most of the luminescence is phonon-linked. The time averaged luminescence is consistent with cold excitons prepared by one photon absorption.

Exciton, oxygen vacancy, and copper vacancy luminescence were modeled with the equation

$$I(t) = n\left(\frac{t-t_0}{r}\right) A e^{-\frac{t-t_0}{\tau}} + c \tag{4.1}$$

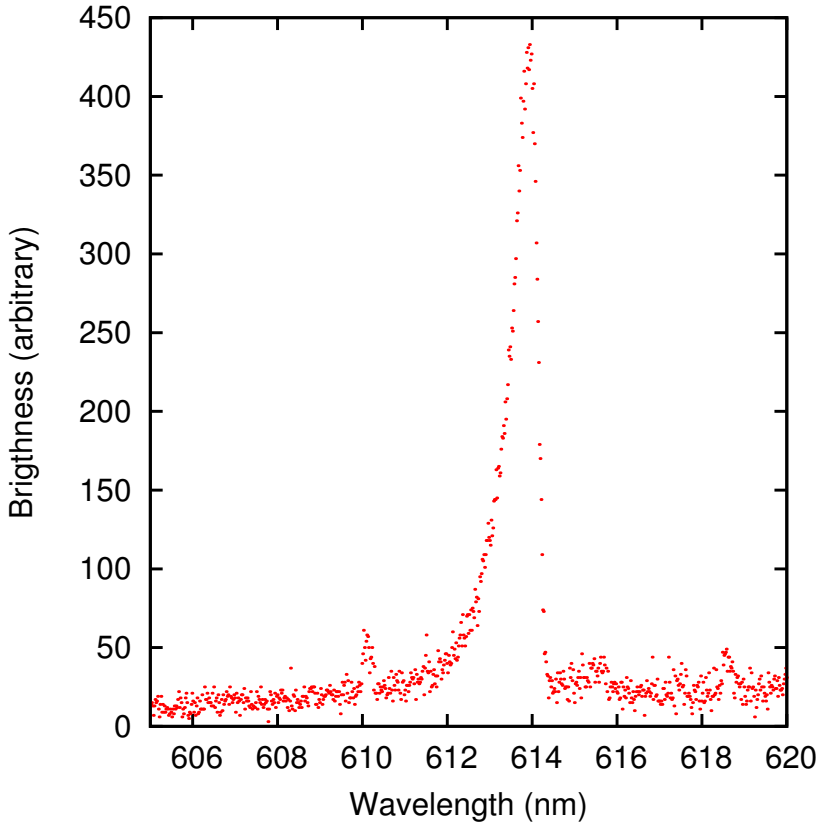

Figure 4.1. Time averaged luminescence for direct comparison to Figure 4.3.

where $n(x)$ is the normal cumulative distribution function (e.g. a Gaussian blurring in the rise time), t_0 is the luminescence start time, r is the rise time, A is the amplitude, c is a constant which handles continuous wave background and any very slow processes, and τ is the luminescence fall time. Since the path length through the spectrograph to the streak camera is wavelength dependent, the luminescence start time is wavelength dependent.

Exciton luminescence was integrated between the nominal wavelengths of 605 and 658 nm. Oxygen vacancy luminescence was integrated between 692 and 799 nm. Copper vacancy luminescence was integrated between 860 and 987 nm.

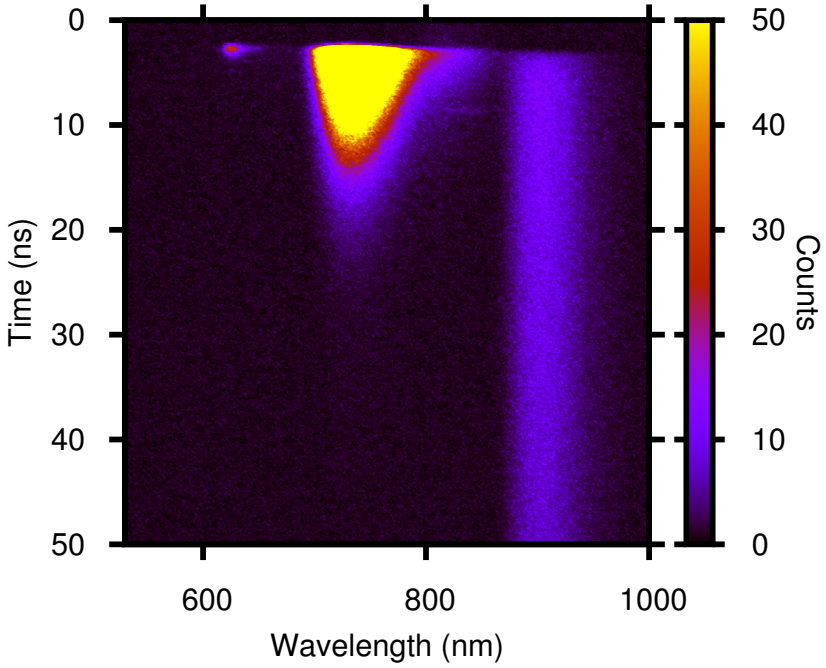

Figure 4.2. Time resolved luminescence from cuprous oxide synthesized from a 0.9999 purity copper precursor. The scale is adjusted to show the exciton and copper vacancy luminescence, but the oxygen vacancy luminescence is saturated on this scale. There is no saturation in the raw data.

4.2. Results

Figure 4.2 shows luminescence from the first sample. Exciton, oxygen vacancy, and copper vacancy luminescence are detected with respectively increasing lifetimes. The scale was picked so that the copper vacancy luminescence was clearly visible but the oxygen vacancy luminescence maximum is cut off in the color scale. The faint feature at about 8 ns and 800 nm is ambient Ti:Sapphire laser light.

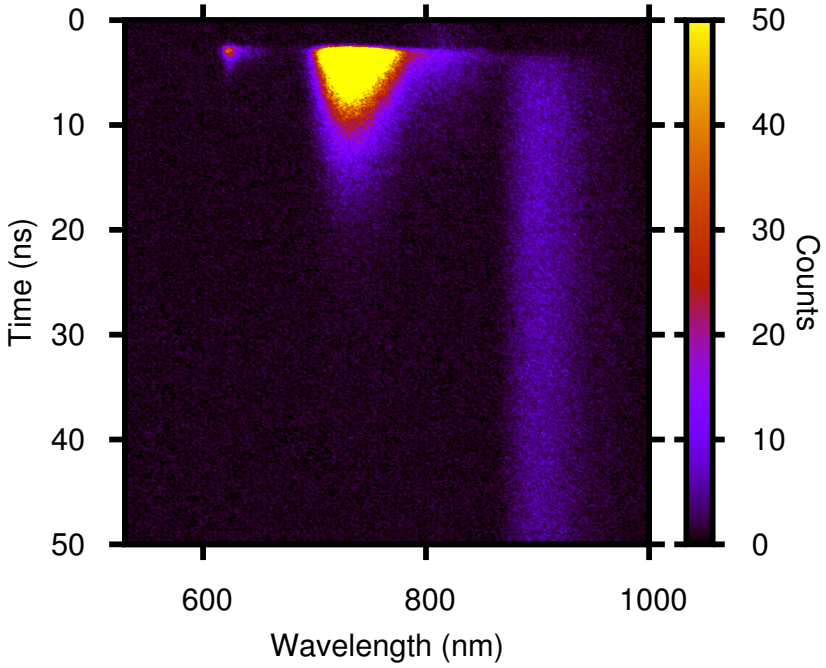

Figure 4.3. Time resolved luminescence from cuprous oxide synthesized from a 0.99999 purity copper precursor. The scale is adjusted to correct for a shorter exposure compared to Figure 4.2. A time averaged spectrum is shown in Figure 4.1.

Figure 4.3 shows the corresponding data for the second, higher purity sample. A shorter exposure was used since it was apparent this sample is qualitatively similar. Brightness scales are adjusted to be comparable. This sample has a longer exciton and copper vacancy lifetime, but a shorter oxygen vacancy luminescence lifetime.

Figure 4.4 shows the wavelength-integrated streak camera data and the results of regression of Model 4.1 for each luminescence type. Interesting deduced time constants are plotted as a logarithmic bar graph in Figure 4.5.

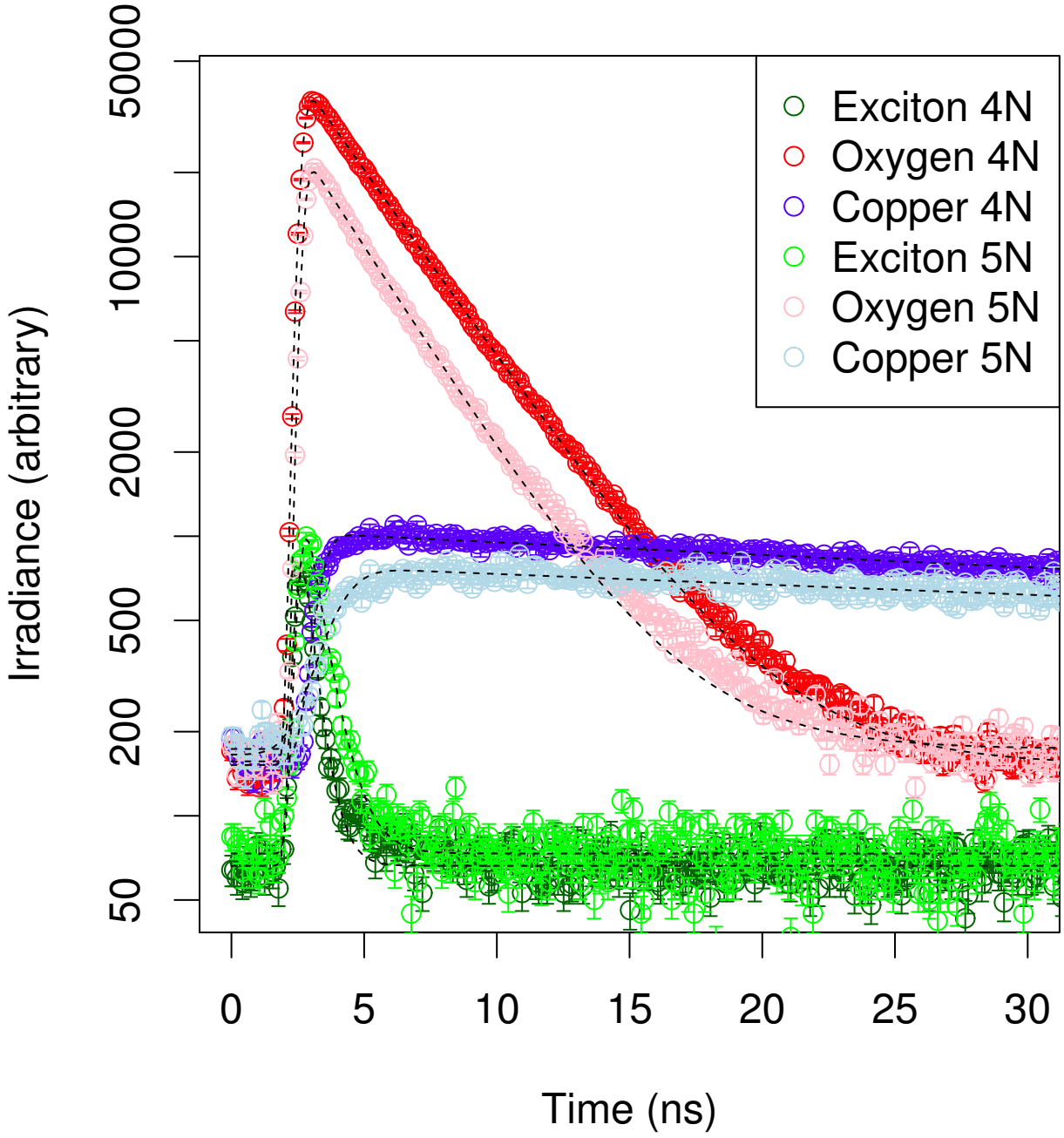

Figure 4.4. Wavelength-integrated, time resolved luminescence from samples prepared using copper of two different purities.

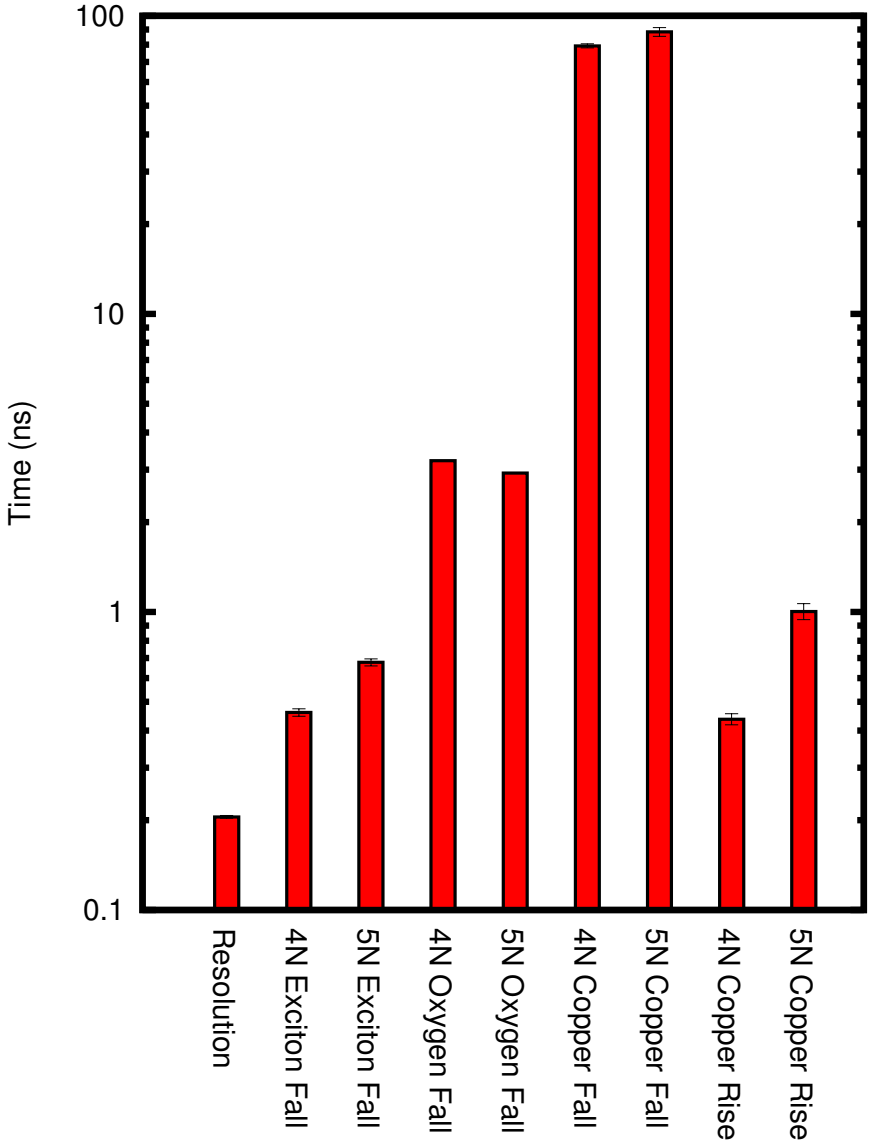

Figure 4.5. Time scales of luminescence from the orthoexciton, oxygen vacancies, and copper vacancies. The graph is on a logarithmic scale.

4.3. Conclusions

4.3.1. Excitons

Firstly, we do not observe the very long paraexciton lifetime of about 13 μs previously reported [11]. This is not surprising owing to the weakness of the paraexciton luminescence and the small time window. The time window is much larger than in my previous report [42]. The fall time of the exciton luminescence is resolved but is not long enough for the temporal shape of the decay to give hints to the cause of the decay; for example Auger decay and diffusive expansion give slightly different predictions for the time dependence of the luminescence decay. Using a higher purity copper precursor in the synthesis seems to increase the exciton lifetime by 47%. I attribute the exciton luminescence fall time to ortho- to paraexciton conversion because of the long copper vacancy luminescence lifetime.

4.3.2. Oxygen Vacancies

The oxygen vacancy luminescence occurs promptly and has a lifetime very different from the exciton or copper vacancy luminescence lifetime. Generally oxygen vacancy luminescence is weak in synthetic samples, but we see at short times it is very bright. Below gap pumping is known to selectively pump oxygen vacancy luminescence [100]. In aggregate, the properties of the oxygen vacancy luminescence suggest it is caused by pumping of the oxygen vacancy state without an intermediate exciton state [104]. The oxygen vacancy lifetime is lower in the sample grown from the higher purity crystal, suggesting that doped vacancies [82] have a longer excited state lifetime.

4.3.3. Copper Vacancies

The copper vacancy luminescence lifetime is very long. It seems implausible that this reflects the intrinsic lifetime of an excited copper vacancy. I interpret the copper vacancy luminescence lifetime as the lifetime of the dark paraexciton, which transfers energy to the copper vacancy defects. A previous report showed that at temperatures below 40 K, the exciton and oxygen vacancy luminescence had the same lifetime [77]. That experiment used a sample where oxygen vacancies were the primary defect. This experiment uses samples where copper vacancies are the primary defect.

Both the lifetime and the rise time of the copper vacancy luminescence are much larger in the sample prepared from the higher purity copper precursor. This is because impurities can catalyze the formation of copper vacancies [82]. The rise time indicates that the excitons must propagate for a while (longer than the ortho- to paraexciton conversion time) before they encounter a copper vacancy.

On the whole, the data suggests higher purity copper precursors lead to moderately better sample performance. The high purity sample shows more exciton luminescence and less vacancy luminescence, consistent with previous time averaged luminescence studies [76] and theoretical defect catalysis of vacancy formation [82].

CHAPTER 5

Evaluation of Cuprous Oxide Defects Through Exciton Luminescence Imaging

In this chapter, I describe the spatial distribution of defects in large cuprous oxide crystals to demonstrate the high quality of floating zone synthesis methods this dissertation relies upon. I also describe the underlying defect/exciton and defect/defect interactions, including evidence for variations in both the phonon energy and the exciton thermalization with the lattice.

5.1. Introduction

Owing to the positive parity of the valence and conduction bands, the primary luminescence mechanism in cuprous oxide is emission of two negative parity particles. The strongest process is the decay of an orthoexciton into a 0.014 eV $^2\Gamma_{12}^-$ phonon and a photon [13]. In addition, there is polariton luminescence from the quadrupole quantum mixing of the orthoexciton with a photon [111]. Under mechanical stress, the orthoexciton triplet state is split, and so is its luminescence [1]. The paraexciton can also begin to produce direct luminescence under stress owing to breaking of the negative parity of the band structure [1, 112]. These properties are unique to Cu_2O and Ag_2O, the two cuprite structure materials.

On the one hand, deliberate application of strain to cuprous oxide can be useful for increasing luminescence [113], trapping excitons in a potential [114, 113], initiating

transverse (negative parity) phonon emission [23], or distinguishing otherwise degenerate states [115]. On the other hand, unwanted strain increases Auger recombination [116, 117, 42] and breaks the unique symmetry of cuprite structured crystals. Under practical experimental conditions, cuprous oxide is metastable. The thermodynamic phase is cupric oxide [86] which appears in inclusions when cuprous oxide crystals are cooled too quickly [76]. In this chapter, interfacial stress between the cuprous oxide and the cupric oxide inclusions is a source of strain [90].

Observed serendipitously in this work, luminescence at 1.9477 eV has previously been described as "very weak" and resolvable only at temperatures below 4.2 K [13]. Very little is known about this luminescence, except that it is thought to be extrinsic. This is not discussed in most luminescence studies, probably because most CCD spectrometers have narrow spectral ranges that cannot cover this line and the better known luminescence lines simultaneously.

As discussed in Chapter 3, cuprous oxide is nonstoichiometric [118, 82, 119]. Excitons bind to vacancies in the crystal and then undergo radiative decay [77]. The dominant luminescence is from copper vacancies V_{Cu}^{-}. There are also two types of oxygen vacancy luminescence, from V_{O}^{1+} and V_{O}^{2+}. Vacancies are useful for increasing the conductivity of cuprous oxide [120–123]. However, the luminescence produced by vacancies indicates that vacancies reduce the lifetime of excitons [77, 124] (Chapter 4). The simultaneous existence of both copper and oxygen vacancies occurs because real samples are not perfectly equilibrated. Ultimately, low temperature equilibration conditions should lead to elimination of the minority defect (Equation 3.6).

5.2. Materials and Methods

5.2.1. Samples

A crystal of cuprous oxide was grown using the floating zone method as previously described (Chapter 3, [76]). The starting material was 99.9% Cu rods with a 5 mm diameter. The crystal was grown in air at 7 mm/h using two oxidized rods rotating at 7 rpm in opposite directions. In this chapter, an as-grown sample and a sample annealed at 1045 °C for 5 days with a 5 °C/minute ramp rate are compared to show the benefits of annealing. The samples were polished and are shown in Figure 3.9. In Reference [76], these samples are shown as Figure 8 (a, d) and contribute to Figure 7.

5.2.2. Luminescence Measurements

The samples were placed in a optical microscopy cryostat (Montana Instruments Cryostation). Thermal contact was established with VGE-7031 varnish. The stage temperature was about 5.7 K, with a stability of about 5 mK. The temperature dependence of cuprous oxide luminescence has been well characterized [100]. The samples were in vacuum. A scanning microscope with a 50X, 13 mm working distance objective was used to image the sample though a single window.

The sample was illuminated through the objective using a reflection from a beamsplitter with 4.3 mW (measured between the objective and the beamsplitter) of 532 nm light from a Coherent Verdi G18 laser. Luminescence from the sample passed back through the objective, was partially transmitted through the beamsplitter, passed through a 532 nm long-wavelength-passing dielectric filter, and was collected in a fiber. The spectrum was

recorded with an Andor 303 mm focal length Czerny-Turner spectrograph and DU420A-BEX2-DD CCD camera.

The background was subtracted from the spectrum. During background measurements, the laser beam was blocked. To obtain a consistent spectrum, it was necessary to wait approximately 15 minutes for the stage temperature to stabilize after the sample was illuminated.

Exciton luminescence for each sample was recorded at a 25×25 square grid of locations with a spacing of 20 μm for 30 seconds using a 1200 grooves/mm grating. This process took about 7 hours per sample. For the exciton luminescence, the manufacturer specifies an instrument resolution of 372 μeV.

Vacancy luminescence, which has no spectrally narrow features, was recorded using a 150 grooves/mm grating with a grid spacing of 28 μm. Since a more efficient, coarser grating was used, only one second was required to collect a good vacancy luminescence spectrum and it was possible to easily sample a larger number of locations.

Our previous study [76] was designed to compare room temperature copper vacancy luminescence across samples. To achieve this, each sample was placed at the same distance along the optical axis from the objective. In this experiment, I investigate variations in luminescence within samples, including lines best observed at temperatures below 10 K [100]. The design of the cryostation does not permit each sample to be placed at precisely the same location along the optical axis, so direct comparisons of luminescence brightness between samples are not possible. When changing between samples, the microscope was refocused to optimize the efficiency with which the luminescence was collected.

All measurements reflect conditions near the sample surface because the laser light has a short absorption length [25]. Since excitons and exciton polaritons propagate differently [111], the different types of luminescence come from slightly different volumes, with the highest density and greatest brightness occurring at the laser spot.

5.2.3. Analysis Methods

In summary, the phonon-linked luminescence is modeled. The residuals are used to determine the brightness, energy, and width of the orthoexciton polariton luminescence. Analysis is performed for each location in the hyperspectral image.

Excitons in these conditions are Maxwell-Boltzmann distributed [22, 125, 126]. They can decay into a phonon/photon pair if the phonon has negative parity. There are also three and four particle complications [13]. Phonon-linked luminescence was modeled using the Maxwell-Boltzmann equation for the spectral irradiance I as a function of energy E [127]:

$$I(E) = A\left(|E - E_c|\right)^{\frac{1}{2}} e^{-\frac{E-E_c}{k_B T}}; \tag{5.1}$$

Here A is the brightness, E_c is the orthoexciton ground state energy minus the phonon energy, and k_B is the Boltzmann constant. We only analyze the most efficient luminescence, which is linked to emission of the ${}^2\Gamma_{12}^-$ phonon. For each of 625 locations on each sample, the model was applied between 2.0180 and 2.0300 eV to avoid the region $E < E_c$, where the model is invalid, and to avoid the 2.0318 eV orthoexciton polariton luminescence which could skew the fit. The necessary computer program is listed in Appendix D.2.

The orthoexciton polariton luminescence, which intrinsically has a very narrow spectral width [15, 111], can typically be modeled by a Gaussian. The width of the Gaussian is determined by the spectrometer resolution. In this chapter, I am searching for deviations from the typical luminescence spectrum owing to sample defects. These deviations can cause a Gaussian model, or any other single peaked model, to fail, so for each location I computed the residual brightness after subtracting Equation 5.1. Next I computed the sum over energies of the residual brightness, the residual brightness square weighted mean energy, and the likewise weighted standard deviation energy of the spectrum between 2.0300 and 2.0335 eV. These three statistics describe the brightness, energy, and width of the orthoexciton polariton luminescence respectively. No assumption is made about the structure of the polariton luminescence in the analysis.

For the defect linked luminescence near 1.95 eV I do not have a line shape model. To evaluate it, I summed brightness in the spectrum between 1.9443 and 1.9478 eV.

I modeled vacancy luminescence with a double Gaussian. The first Gaussian described the copper vacancy luminescence. The second Gaussian described the V_{O}^{2+} luminescence. There are two limitations of the model: First, as in previous studies, silicon based detectors do not detect the low energy tail of the copper vacancy luminescence very efficiently. Second, the V_{O}^{1+} luminescence appears indistinctly between the other two peaks.

5.3. Results and Discussion

5.3.1. Exciton Luminescence

The cuprous oxide lattice has octahedral O_h symmetry (not chiral O symmetry). Crystals with this point group are not birefringent. Figure 5.1 is an example of bifrefringence in

as-grown crystals. Figure 5.2 shows that the as-grown sample studied in this chapter had birefringence near its cupric oxide inclusions, presumably owing to interfacial stress that lead to a local deformation of the crystal system [90], possibly to a tetragonal system. The annealed sample did not show birefringence for two reasons: First, annealing removes cupric oxide inclusions [76] and second, annealing relieves stress. These samples were selected for detailed study with the expectation that annealing would improve the quality of the exciton luminescence because strain would be removed.

Equation 2.1 describes the relationship between the strain tensor and the splitting of the orthoexciton. Typical spectra did not show strain splitting in the polariton luminescence or the phonon-linked luminescence (Figure 5.3). However, we did find a location where the polariton luminescence was slightly split (Figure 5.4). The observed splitting pattern is the same as the pattern observed from a previous study where strain was applied to a sample [115]. There is a slight excess in the luminescence near the top of the phonon-linked luminescence peak around 2.02 eV which may be explained by Bose-Einstein statistics.

The exciton temperature as determined from regression of Equation 5.1 was typically about 46 K. Some locations show a higher temperature, which I attribute to defects (Figure 5.5 a, b). The exciton temperature is higher than the thermometer temperature primarily because excitons do not completely thermalize with the crystal lattice before decaying. In addition, there may be a temperature gradient across the sample since it is heated by the laser.

Defects in the locations with elevated temperatures also reduce the brightness of the orthoexciton polariton luminescence (Figure 5.5 c, d). The brightness could be reduced

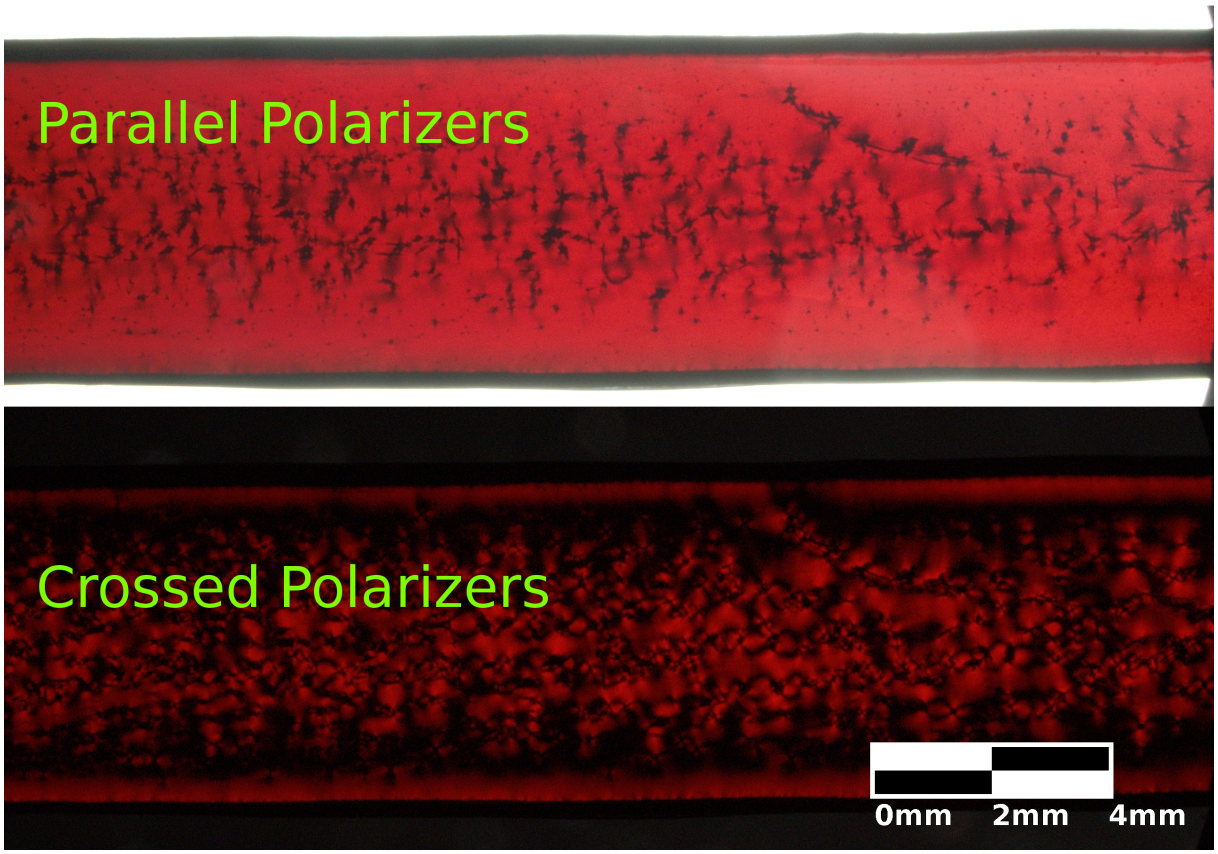

Figure 5.1. Two polariscope images showing inclusion induced strain leads to birefringence. For parallel polarizers, solid dark areas in the sample are inclusions. Blurry dark regions are birefringence. For crossed polarizers, the previously dark, strained areas of cuprous oxide become the only regions where light is transmitted. The as-grown surface also has strain induced birefringence, but strain caused by cutting and polishing is not detected.

because of lower transmission of the crystal surface, or it could be because of excitons decaying in some alternative way at defects. There are also very small shifts in the energy of the polariton luminescence from place to place (Figure 5.5 e, f) which may be explained by stress in the sample (Equation 2.1). Annealing reduced the variation in the mean polariton energy and in E_c across positions (one tailed F-tests), consistent with our expectation that annealing would reduce strain in the sample.

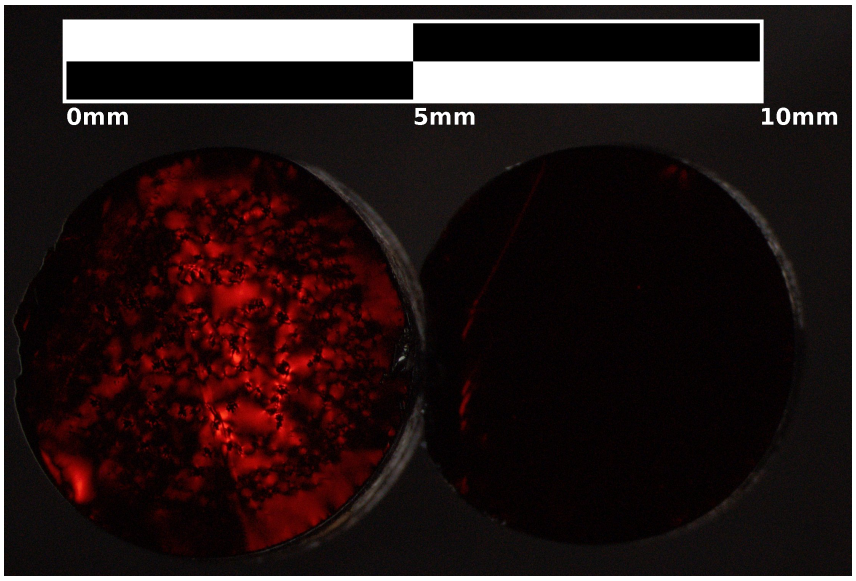

Figure 5.2. Microscope image of back illuminated samples between perpendicular polarizers. The as-grown sample to the left exhibits birefringence (red) owing to strain. The annealed sample to the right does not show birefringence because annealing removes strain. Unpolarized images of the same samples can be found in Figure 3.9.

The phonon-linked luminescence is caused by the decay of an exciton into a phonon and a photon. For a phonon with energy E_Γ, E_c in Equation 5.1 should be related to the polariton energy E_p by the consistent energy equation

$$E_p = E_c + E_\Gamma + E_{KE}. \tag{5.2}$$

Based on a polariton wavenumber of 2.63×10^7/meter [111], the difference between the polariton energy and the exciton ground state energy

$$E_{KE} = \frac{\hbar^2 k^2}{2(m_e + m_h)} \tag{5.3}$$

$$\approx 0.02 \text{ meV}. \tag{5.4}$$

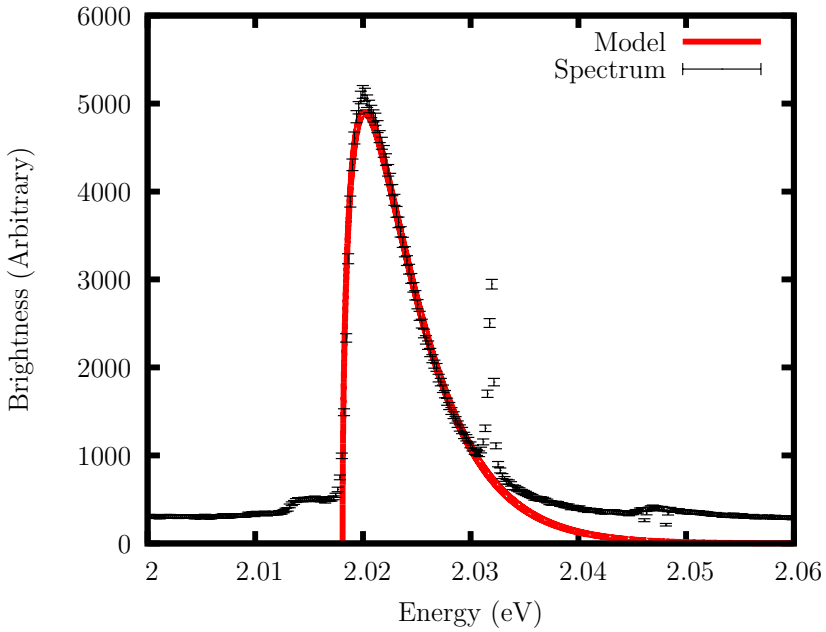

Figure 5.3. An example of a typical luminescence spectrum from the annealed sample. The model of the phonon-linked ${}^2\Gamma_{12}^-$ luminescence is a Maxwell-Boltzmann distribution starting at 2.0181 eV with a temperature of 48 Kelvin (Equation 5.1). The narrow peak is exciton polariton luminescence. The position on the sample is (0, 0).

Therefore I tentatively suggest that E_{KE} is negligible. In Figure 5.6, the phonon energy is determined from $E_p - E_c$. Surprisingly, the inferred phonon energy is strongly and positively correlated with the polariton energy. There is a tiny downward curvature in the data. The typical energy difference $E_p - E_c$ is 0.0136 eV.

Strain increases the radiative transition rate, which reduces the exciton lifetime (Section 2.5). If the intrinsic exciton polariton energy is E_0 and the intrinsic lifetime is t_0, but the measured energy is E, then a simple model of the expected decay rate for strains

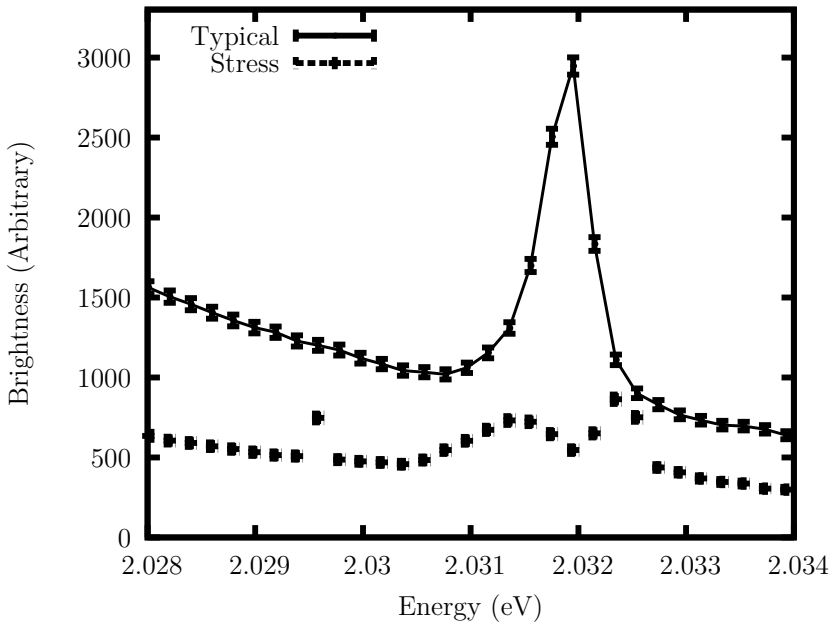

Figure 5.4. A typical, resolution limited spectrum of polariton luminescence and an atypical spectrum showing three peaks caused by stress. Both are from the annealed sample. In the images, the outlier is located at (480, 460) μm.

much less than the yield stress is

$$\frac{1}{t} = \frac{1}{t_0} + c|E_0 - E| \tag{5.5}$$

$$t = t_0 \left(1 - ct_0|E_0 - E| + \mathcal{O}\left((ct_0|E_0 - E|)^2\right)\right), \tag{5.6}$$

where c is a constant.

If the exciton lifetime is infinite, the excitons thermalize to the lattice temperature T_l. A value T_i characterizes the initial condition of the excitons before they have thermalized. If τ is the thermalization time constant then for lifetimes much longer than the spontaneous phonon emission time, the exciton temperature according to the heat equation

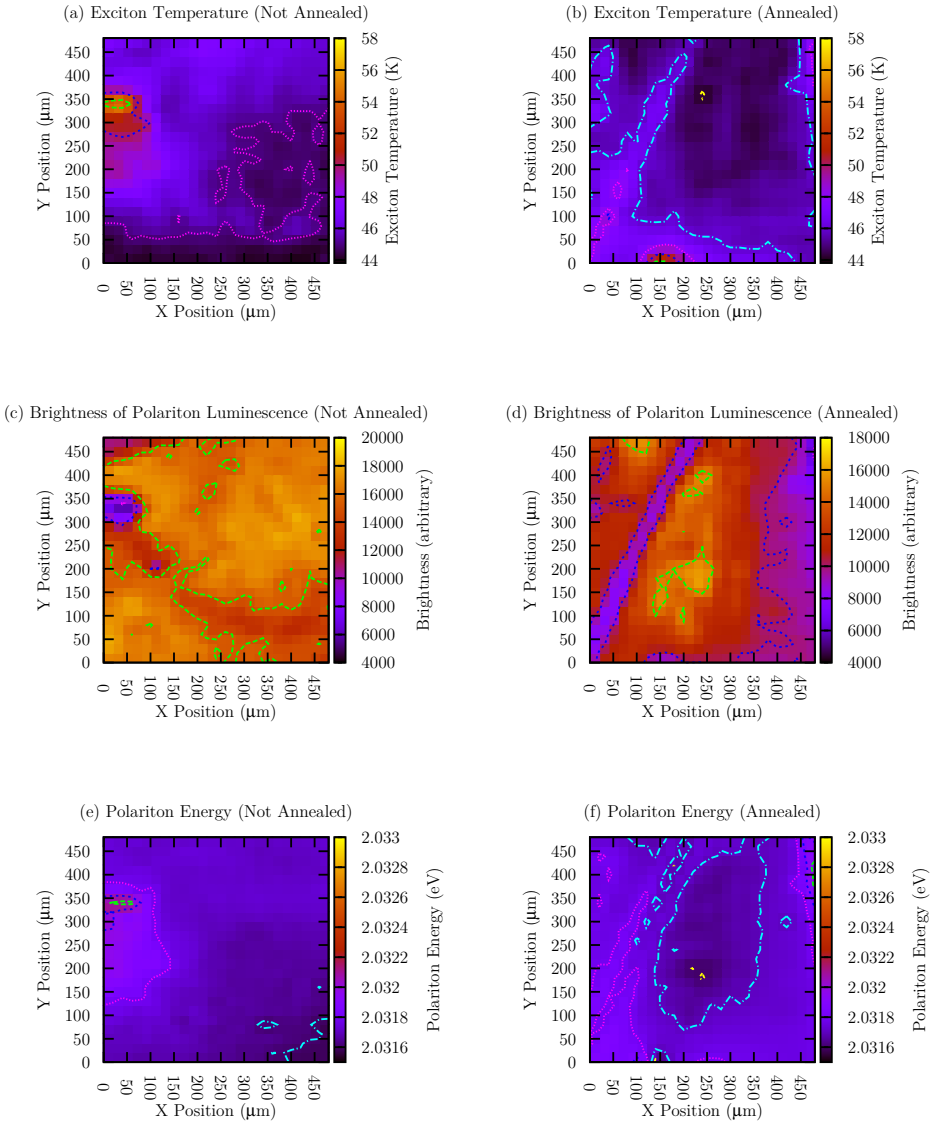

Figure 5.5. (a, b) Spatially resolved temperature of the exciton gas. Temperature is determined using the Maxwell-Boltzmann model (Equation 5.1) shown in Figure 5.3 for the spectrum at each location. The excitons are not expected to be in equilibrium with the lattice. In each sample, a few defects mildly increase the exciton temperature measurement. (c, d) Brightness of the orthoexciton polariton luminescence. Defects reduce the brightness of the luminescence. Brightness is not comparable between samples. (e, f) Energy of the orthoexciton polariton luminescence. Stress defects can lead to tiny shifts in the mean luminescence energy. (c, d) is compared with (e, f) to produce the pattern in Figure 5.7. (a, c, e) Sample without annealing. (b, d, f) Sample with annealing.

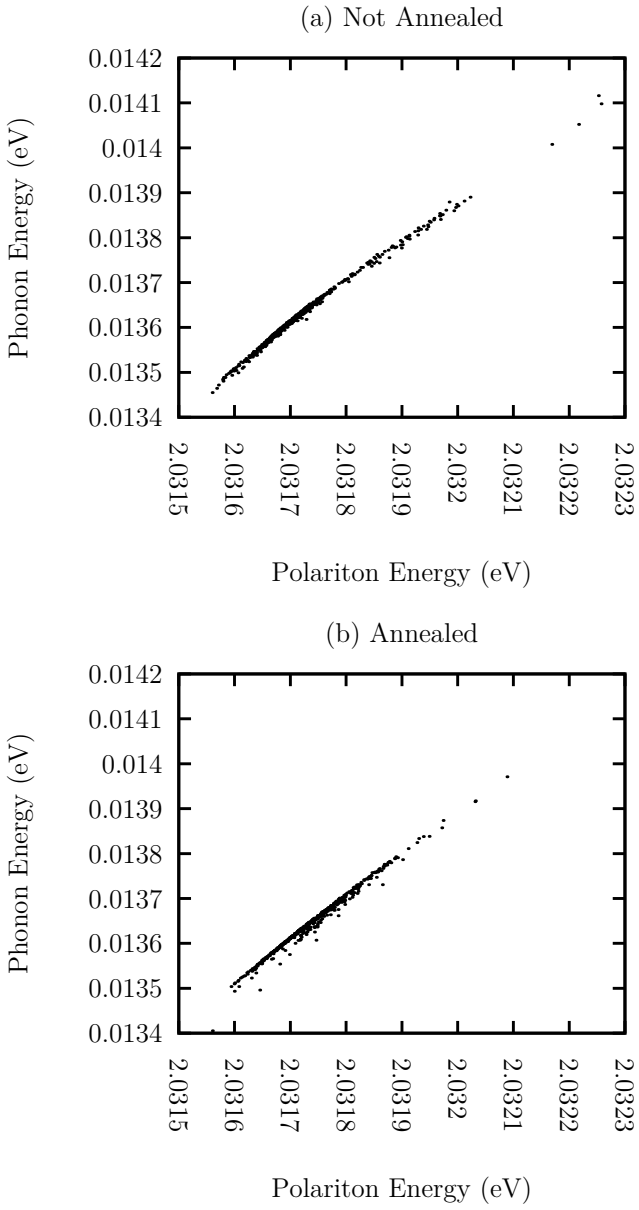

Figure 5.6. The phonon energy is inferred from the polariton energy minus the onset energy of phonon-linked luminescence. Phonon energy positively correlates with polariton energy. Annealing reduces the spread in the polariton luminescence energy and the spread of the onset energy of phonon-linked luminescence E_c (one tailed F-tests). (a) Sample without annealing. (b) Sample with annealing.

is

$$T(t) = (T_i - T_l)e^{-t/\tau} + T_l \tag{5.7}$$

$$T(E) = (T_i - T_l)e^{-\left(t_0 - ct_0^2|E_0 - E|\right)/\tau} + T_l. \tag{5.8}$$

This relationship is not valid for short lifetimes or large strains.

Figure 5.7 shows the simple model 5.8 is consistent with the measurements. In the regression, $(T_i - T_l)e^{-\frac{t_0}{\tau}} = 39$ Kelvin is a single parameter which indicates the amount of laser heating of the exciton gas. The thermometer measurement $T_l = 5.66$ Kelvin was assumed. E_0 was 2.0316 eV. Most measurements showed polariton energies higher than this value. The value of $\tau/(ct_0^2)$ determined through regression was 2.40±0.03 meV for the unannealed sample and 3.6±0.2 meV for the annealed sample. The physical meaning of $\tau/(ct_0^2)$ is the energy scale at which shifts in the exciton energy significantly decrease thermalization. Potential energy well depths should be kept below this value to obtain trapped cold orthoexciton polaritons.

The measured exciton polariton line width, as defined by the residual brightness square weighted standard deviation energy, of the polariton luminescence is typically consistent with the instrument resolution (Figure 5.8). However, there are a few outliers with a substantially larger measured line width. A large line width may indicate a large local variation in strain.

5.3.2. Two Phonon Emission Luminescence

The luminescence at 1.95 eV is typically very weak [13]. Our spatially resolved spectra show that this is caused by spatial averaging. The brightness can be larger (Figure

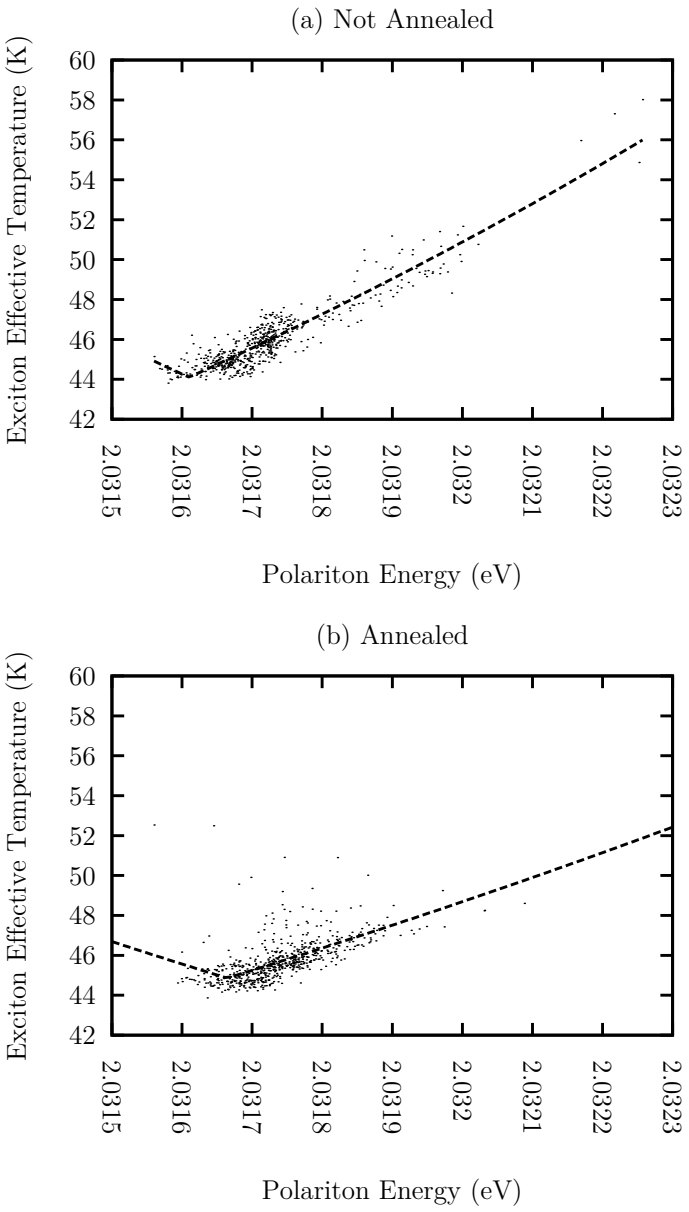

Figure 5.7. Strain can cause deviations from the intrinsic exciton polariton energy. It can also cause a decrease in exciton lifetime. Shorter exciton lifetimes imply less time for excitons to thermalize with the lattice, which leads to higher temperatures. The curve is based on Equation 5.8.

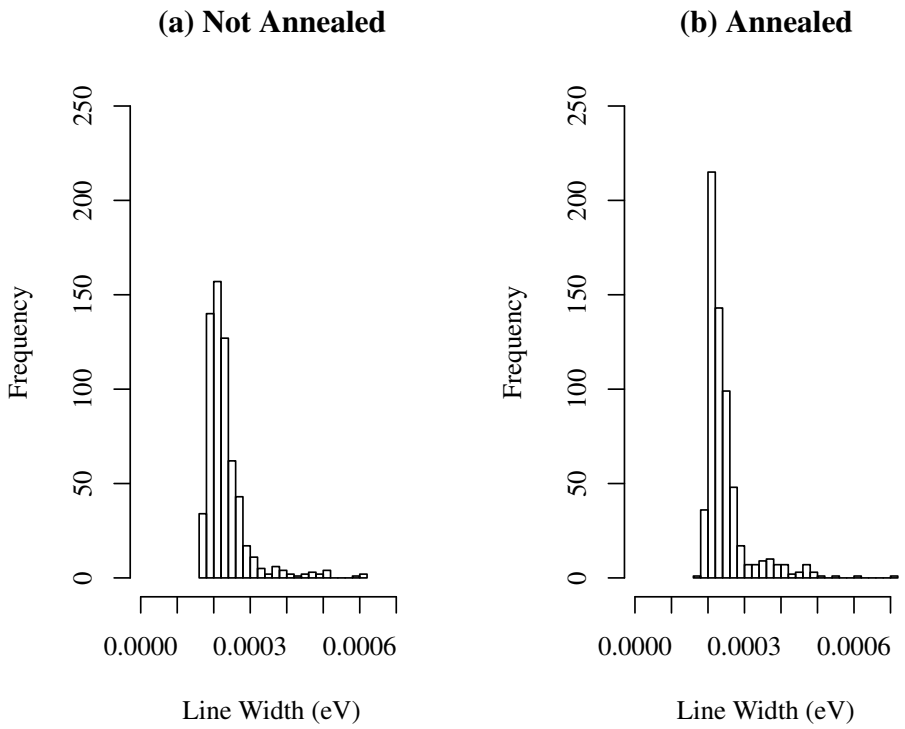

Figure 5.8. Histograms of polariton line width. In most cases, the line width is consistent with the instrument resolution. (a) Sample without annealing. (b) Sample with annealing.

5.9) at isolated locations (Figure 5.10). Petroff et al. [13] did not observe the luminescence above 4.2 K, which is slightly below the operating temperature for this experiment. Petroff identifies three two-phonon emission processes and one three-phonon emission process, but suggests that a lack of temperature broadening indicates that the 1.95 eV luminescence is not caused by phonon emission. I agree with Petroff that the cause of the luminescence is extrinsic, but point out that energetically it is consistent with emission of two 0.0431 eV ${}^1\Gamma_2^-$ phonons [13]. Two phonon transitions are also known in silicon [128] and graphene [129], though in graphene the context is quite different. This two phonon

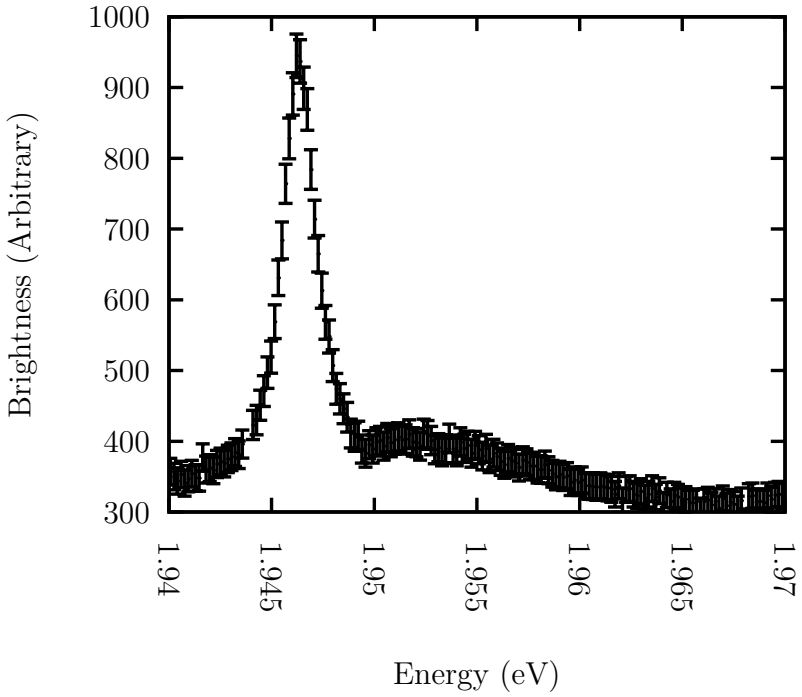

Figure 5.9. An example of two phonon emission luminescence from the annealed sample, picked from a particularly bright location. The main peak is the proposed two ${}^1\Gamma_2^-$ phonon emission luminescence. The slight hump to the right is caused by ${}^3\Gamma_{15}^-$ phonon emission luminescence. The position on the sample is (0, 40).

emission luminescence's energy lies just below the peak of the weak, broad ${}^3\Gamma_{15}^-$ phonon emission luminescence, which can also be found in Figure 5.9.

Hypothesizing that this localized luminescence may be caused by strains in the sample or by defects which cause strain, I expect to find a correlation between the spectral width of the exciton polariton and the brightness of the 1.95 eV two phonon emission luminescence (Figure 5.11). A significant positive correlation was found, however the coefficient of determination was only $R^2 = 0.2$ for the as-grown sample and $R^2 = 0.6$

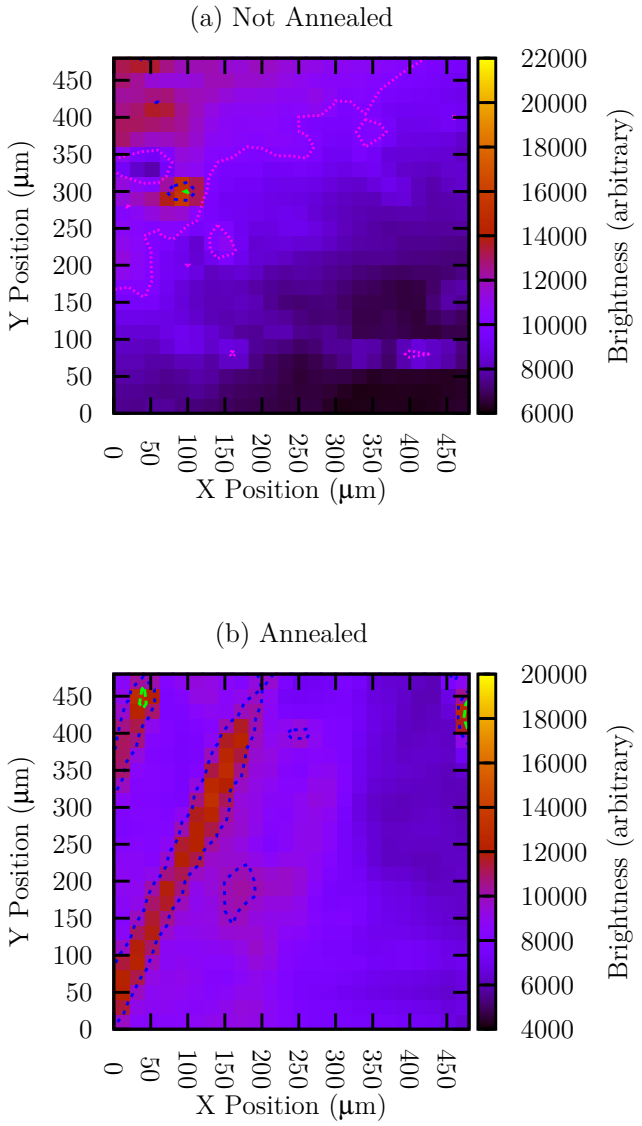

Figure 5.10. Intensity of two phonon emission luminescence at 1.95 eV showing bright defects. (a) Sample without annealing. (b) Sample with annealing.

for the annealed sample. Since the exciton polariton line width is normally less than the instrument resolution, it is challenging to find strong relationships.

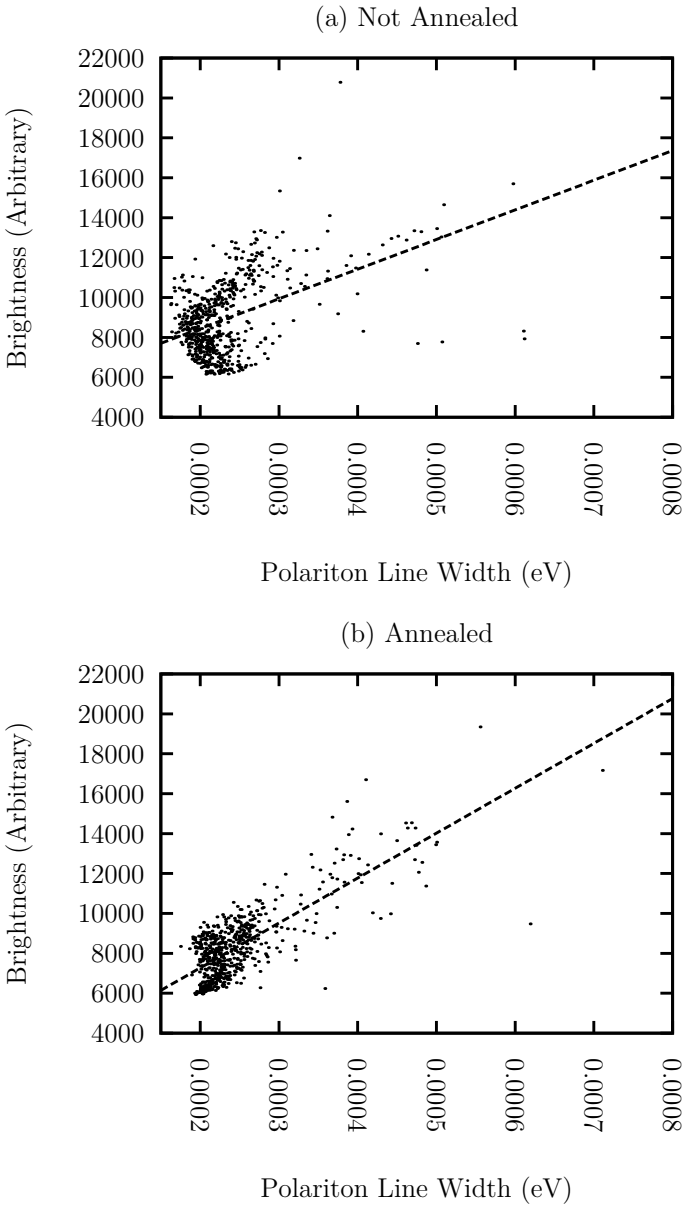

Figure 5.11. Brightness of two phonon emission luminescence versus polariton line width. The brightness increases as strain breaks the parity symmetry of the exciton. The polariton line width also increases for the same reason. (a) Sample without annealing. (b) Sample with annealing.

5.3.3. Vacancy Luminescence

Our samples primarily show copper vacancy luminescence, consistent with other studies using crystals grown with the floating zone method (1.4 eV, Figure 5.12). Higher energy oxygen vacancy luminescence (1.7 eV) is also present. I only observe the doubly ionized oxygen vacancy luminescence clearly. The singly ionized oxygen vacancy luminescence is mostly obscured by the two overlapping, stronger peaks. In the coarse detection mode, the exciton polariton and phonon-linked luminescence are also apparent, but they are not well resolved. Leakage of laser light through the long wavelength pass filter is also barely detected.

Some locations on the samples show decreased copper vacancy luminescence (Figure 5.13). Copper vacancies may be removed near cupric oxide inclusions through the reaction 3.4[76]. Oxygen vacancies (Figure 5.14) coexist with copper vacancies because cuprous oxide forms under nonequilibrium conditions, where the degree of net copper deficiency varies from place to place.

There is a negative correlation across locations between copper and oxygen vacancies in the annealed sample with $R^2 = 0.3$, but a weak positive correlation in the as-grown sample with $R^2 = 0.1$ (Figure 5.15). There are four ways stoichiometry in cuprous oxide can potentially be manipulated. The first two are interfacial exchange between Cu_2O and Cu or O. The third way, exchange with CuO, is facilitated by copper vacancies (Reaction 3.4). The fourth possibility is annihilation of unlike vacancies (Reaction 3.6). The as-grown sample was cooled rapidly to room temperature after crystallizing, preventing much diffusion from occurring. When the annealed sample was cooling, the vacancies in the lattice diffused. Annihilation is consistent with the development of a negative correlation

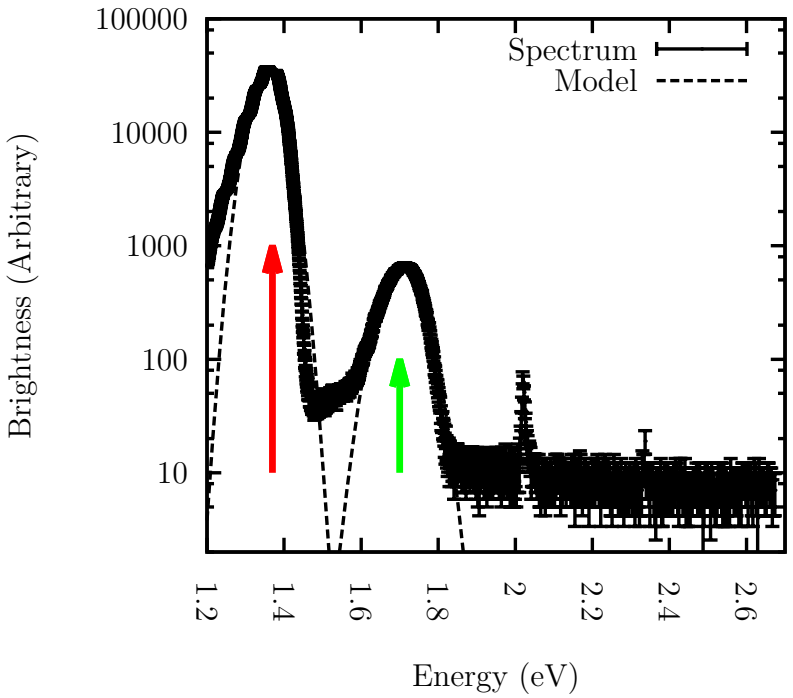

Figure 5.12. An example of a typical copper and oxygen vacancy luminescence spectrum from the annealed sample modeled with a two Gaussians. The copper vacancy luminescence is identified with a red arrow. The oxygen vacancy luminescence is identified with a green arrow. The scale is log-linear. The position on the sample is (0, 0).

after annealing. The remaining vacancy concentrations are determined by the spontaneous spatial variation in Cu deficiency, but the annealing and annihilation increases the length scale and magnitude of deficiency variations relative to overall deficiency.

5.4. Conclusions

Defect luminescence is a useful tool for evaluating advances in cuprous oxide synthesis [130–132, 124, 56]. Detailed luminescence imaging of cuprous oxide crystals grown by the floating zone method shows that there are few defects in the samples, supporting the other experiments in this thesis. Sample stress plays an important role in exciton dynamics and

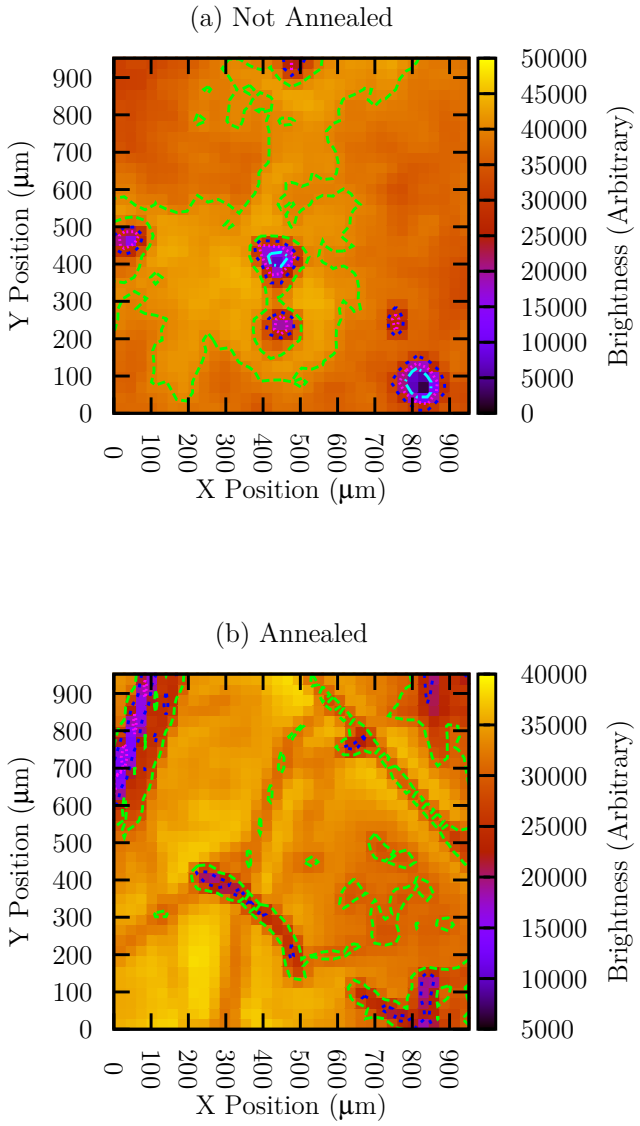

Figure 5.13. Spatially resolved brightness of copper vacancy luminescence. (a) Sample without annealing. (b) Sample with annealing.

luminescence (Section 2.5). The exciton polariton luminescence of our as-grown sample showed little evidence of stress, but the annealed sample was even better. Two ${}^1\Gamma_2^-$ phonon emission luminescence appears to be associated with defects in the crystal and is

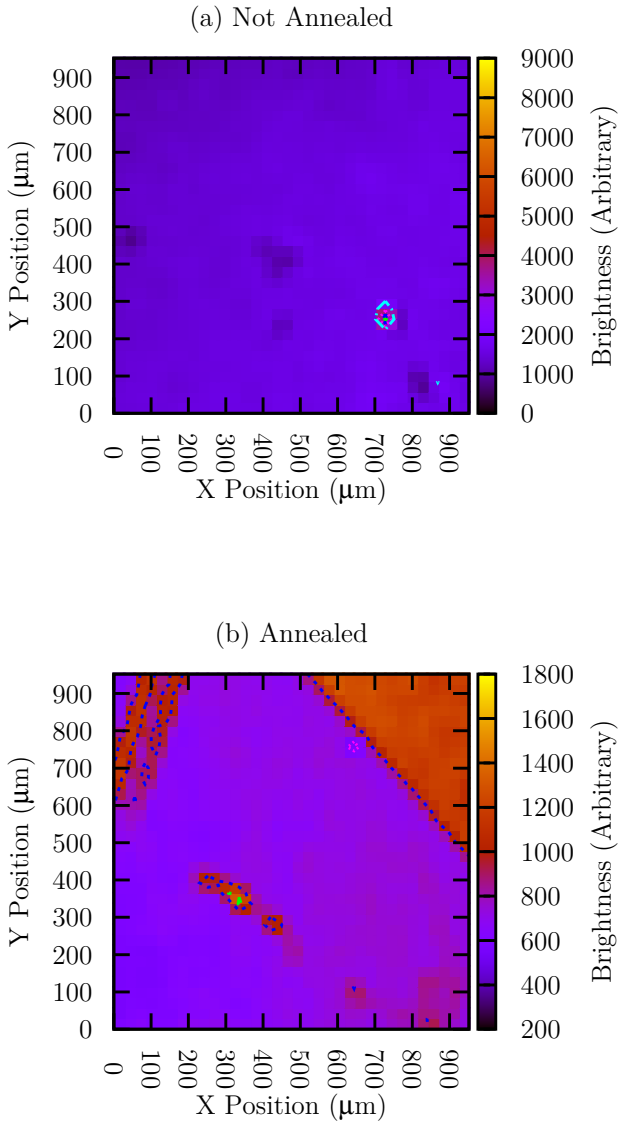

Figure 5.14. Spatially resolved brightness of oxygen vacancy luminescence. Compare (b) with Figure 5.13 (b) to see the negative correlation in Figure 5.15 (b). (a) Sample without annealing. (b) Sample with annealing.

localized in bright spots. Annealing cuprous oxide crystals contributes to the annihilation

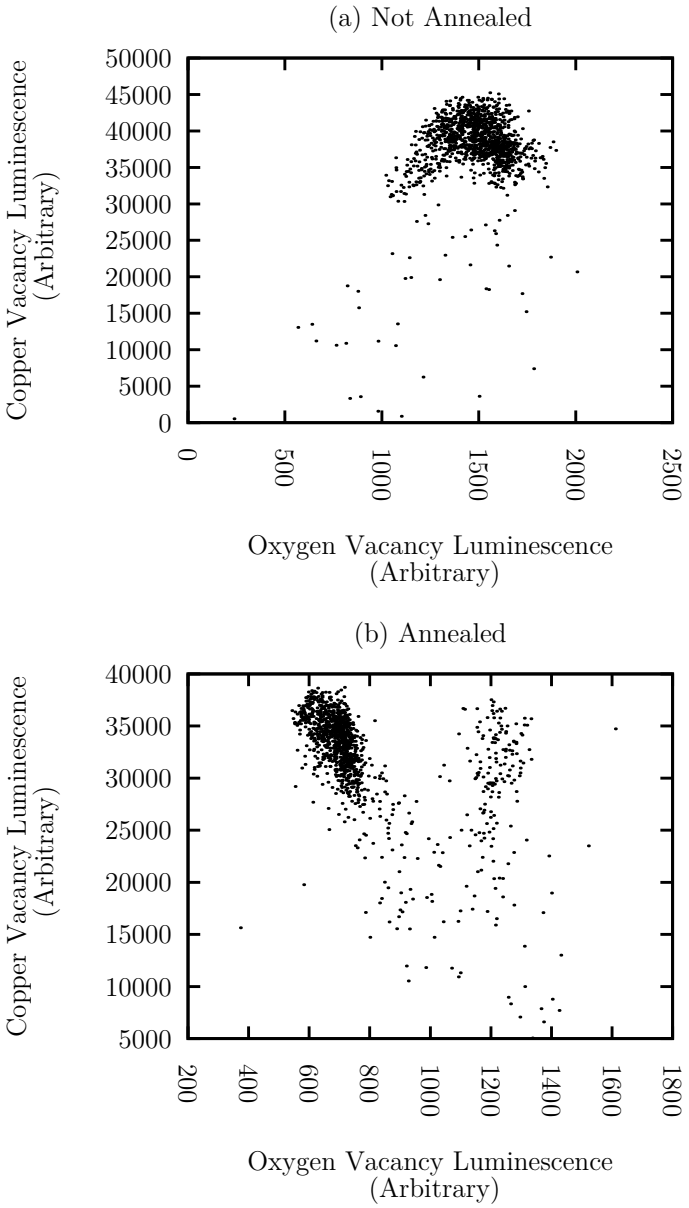

Figure 5.15. Comparing the brightness of luminescence from copper and oxygen vacancies. After annealing, a negative correlation develops as the two types of vacancies annihilate. (a) Sample without annealing. (b) Sample with annealing. Two outliers in (a) are not shown.

of copper and oxygen vacancies, leading to a negative correlation between the two kinds of vacancy associated luminescence.

CHAPTER 6

Third Harmonic Generation

Third harmonic generation produces electron/hole pairs during two photon absorption experiments. The physics, however, differs from the way photoionization produces electron/hole pairs during two photon absorption (Chapter 7).

6.1. Introduction

In a perturbative regime, harmonic generation efficiency follows a power law with an exponent equal to the order of the harmonic.

$$I_{n\omega} \propto I_{\omega}^{n} \tag{6.1}$$

Many measurements find lower exponents [133]. In simpler cases such as gasses, scaling is well described [134] by a nonperturbative model [135].

The relevance of three photon processes to excitons in cuprous oxide was first inferred via the power dependence of stressed cuprous oxide paraexciton luminescence [28]. Power law behavior was observed with an exponent 2.8±0.2. In a Lyman transition study, results were consistent with cubic behavior[12]. Using the Z-scan method and direct detection, an exponent of 1.8 was observed [29], which presents a considerable discrepancy. The first two experiments may be observing photoionization, which is explained in Chapter 7, rather than third harmonic generation.

Nonperturbative behavior is typically realized in measurements of the higher harmonics because the two phenomena are caused by intense pumping. Such investigations in crystals began with ZnO [136]. While harmonic generation in cuprous oxide begins with the third harmonic, we will show that the magnitude is better described by a nonperturbative scaling.

Four earlier reports used 1,240 nm excitation [28], involved a possibly third-photon photoionizing 1,220 nm pump and 10,700 nm probe [12], and operated with a 1,300 to 1,800 nm fundamental [6, 29]. Our experiment is able to access the transparent region for third harmonic generation in cuprous oxide at low temperature, which includes fundamental wavelengths longer than 1,820 nanometers.

Previous results on the nonlinear optical constants include the second order index of refraction measured at 1,064 nm [6] and two-photon absorption coefficient at 1,220 nm [29]. In the past, $\chi^{(3)}$ effects in cuprous oxide were tacitly assumed to be isotropic. Third harmonic generation is not.

6.2. Methods

Six different cuprous oxide single crystals were used to study third harmonic generation behavior. Three synthetic samples were grown via the floating zone method [76] using at least 99.9%, 99.99%, and 99.999% pure copper metal as starting material. Another high purity crystal (Figure 6.1) was received from A. Revcolevschi [86]. It was grown in a floating zone furnace using 99.999% pure starting material. Two geological samples were also used. Geological samples were included for comparison because they are commonly studied in many laboratories.

Figure 6.1. The sample received from A. Revcolevschi, after polishing.

The third harmonic generation of pump wavelengths from 1,200 to 2,000 nm was investigated in multiple samples to verify reproducibility. A 35 femtosecond OPA light source (similar to Chapter 4) was focused on polished faces of samples in a vacuum at room temperature and the absolute magnitude of the transmitted third harmonic generation was measured with a silicon power meter. The high intensity of the pump laser allowed complete evaluation of the efficiency of third harmonic generation. The samples were mounted on aluminum sheets with holes punched through them instead of using a window as a mount. This ensured that only the sample was in the laser beam's focal region. In these measurements, the fundamental is not substantially attenuated by harmonic generation. Similar results were obtained for all samples measured for all pump

Figure 6.2. A geological sample of unknown provenance used for Figure 6.5

wavelengths that were examined. The results from a [100] face of the crystal received from A. Revcolevschi were selected for presentation in Figure 6.3 because, of the samples available at the time of this experiment, its 8 mm thickness could best occupy the intense region of the beam. The beam had a 64 μm minimum radius. The best power stability coefficient of variation observed was 1.5% after harmonic generation.

The dependence of third harmonic generation on the polarization of the laser was also examined on multiple samples for reproducibility. All samples gave similar results. Measurements from a geological sample (Figure 6.2) illuminated along the [100] axis are reported in Figure 6.5. This sample gave the clearest results owing to a longer integration time.

6.3. Results

6.3.1. Exponent

The absolute power dependence of third harmonic generation is presented in Figure 6.3, which shows that large quantities of third harmonic were generated. The overall relationship between the fundamental intensity and the third harmonic intensity can be described by a power law with an exponent lying between those reported in previous measurements [28, 29, 12]. Only a mild wavelength dependence of the third harmonic signal was observed at room temperature. The observation of third harmonic generation at photon energies above the gap in Figure 6.4 is remarkable. The stability of the OPA power across wavelengths is also excellent.

6.3.2. Selection Rules

Figure 6.5 shows that the third harmonic signal is in fact dependent on the polarization of the laser. In this figure, light centered near 1,800 nm from the OPA was used to illuminate a geological cuprous oxide sample along the [100] axis. The sample was cooled in vacuum to approximately 2.7 Kelvin. The third harmonic signal spectrum was collected for various orientations of a half-wave plate located between the OPA and the sample.

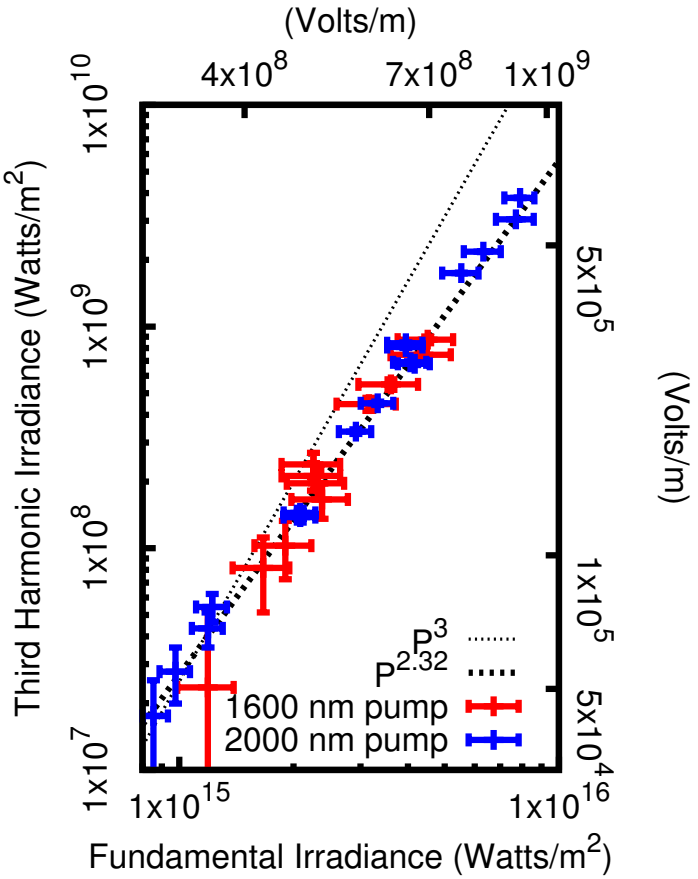

Figure 6.3. Dependence of third harmonic generation on fundamental laser peak irradiance. The cubic curve shows that if a perturbative Gaussian beam model with coherence length 10 μm is used, a $\chi^{(3)}$ factor about 10^4 less than the correct value [6] would be inferred owing to non-cubic behavior at the high irradiances used here. The data points are eleven standard errors from perturbative behavior.

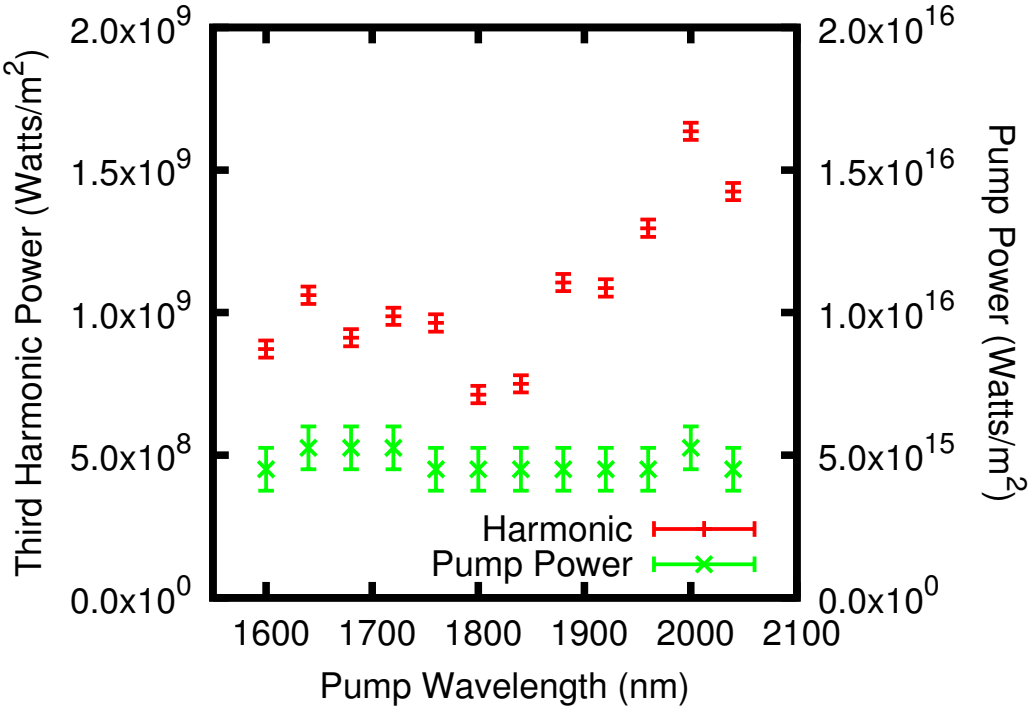

Figure 6.4. Wavelength dependence of pump power and third harmonic generation at room temperature.

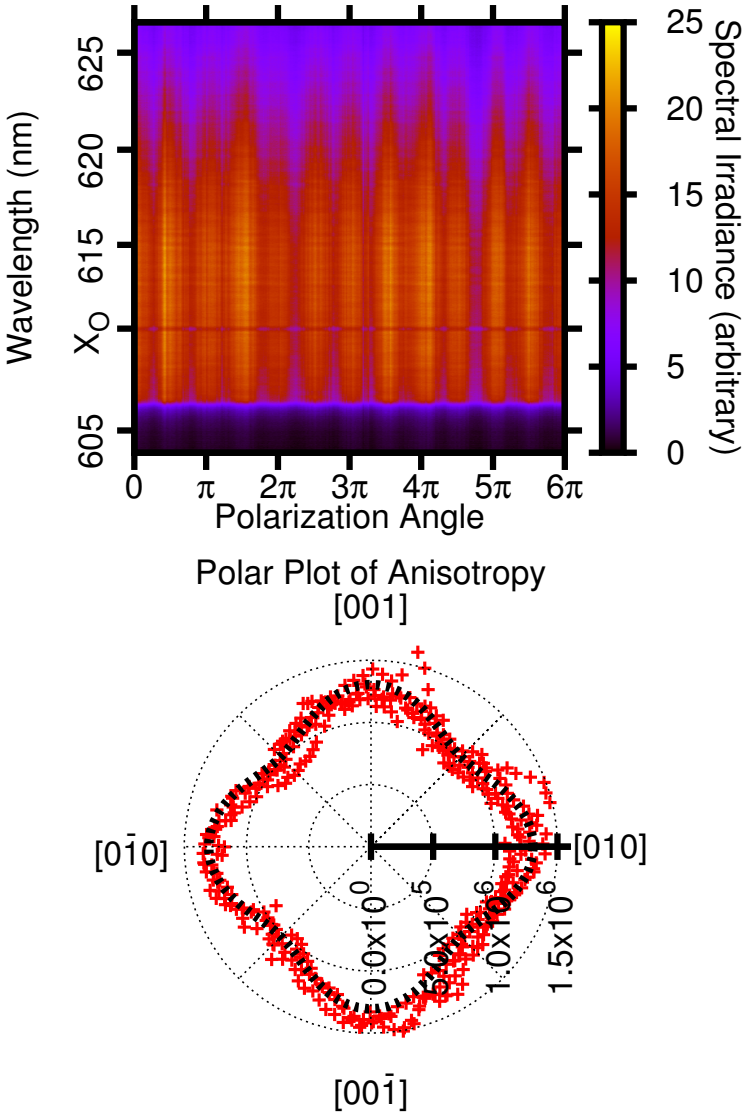

Figure 6.5. Dependence of third harmonic generation on fundamental laser polarization, with the electric field measured from [010]. The anisotropy is 22 times the standard error. The wavelength-integrated polar plot of the data also graphs the theory shown in Expression 6.2. In the polar plot, isotropic results would form a circle.

At short wavelengths starting near 605 nm, the third harmonic is greatly reduced by phonon-assisted absorption, which extends well below the bandgap energy [25]. A narrow *1s* quadrupole orthoexciton-polariton absorption line (X_O) is also observed. This demonstrates exciton production via the third harmonic without an intermediate electron-hole state. Absorption studies in cuprous oxide do not show this line (except in [91] and [33]), but it is clearly visible in our relatively thick samples. Polarization independence of this line is restricted to the [100] axis [28]. Since two-photon luminescence from this line is narrow even when pumping with spectrally broad lasers [137, 29], it is notable that absorption of the third harmonic photons follows the pattern of white light. At long wavelengths, third harmonic generation displays the approximately Gaussian spectral profile of the laser. Supercontinuum generation and plasma formation were not observed.

For normal incidence on a [100] cubic crystal face and with ϕ as the angle between the electric field and the [010] axis, the total third harmonic generation is proportional to [138, Equation 39]

$$2\left(3\chi^{(3)}_{1212}\right)^2 + \left(A_0\frac{g_{3b}}{N}\frac{\chi^{(3)}_{1111}-3\chi^{(3)}_{1212}}{4}\right)^2\cos^2(2\phi) \tag{6.2}$$

This is compared with the data in Figure 6.5. In our experiment, no detection polarizer was used so that all the third harmonic generation was collected; therefore a factor of $\sin^2(2\phi)$ found in [138] is omitted in the second term. A_0, g_{3b} and N are as defined in [138].

The measured part of the third harmonic which is polarization-independent is

$$\frac{2\left(3\chi^{(3)}_{1212}\right)^2}{2\left(3\chi^{(3)}_{1212}\right)^2+\left(A_0\frac{g_{3b}}{N}\frac{\chi^{(3)}_{1111}-3\chi^{(3)}_{1212}}{4}\right)^2}=0.78\pm0.01 \tag{6.3}$$

Since in a cubic crystal the polarization is never more than $\frac{\pi}{4}$ from the axis with maximal harmonic generation, we have a quantity $\geq \cos\left(\frac{\pi}{4}\right)$ in Equation 6.3. The highest possible value, which would occur in an isotropic material, is one.

6.4. Combined Behavior

The combined third harmonic signal (excluding linear absorption) for a fundamental measured in Watts/m^2 was found to be

$$\begin{aligned} I_{3\omega} &= (4.41\pm0.08)\cdot10^{-28}I_\omega^{2.32\pm0.06} \\ &\quad\times\left(\cos^2(2\phi)+3.6\pm0.2\right)\ \text{Watts/m}^2 \end{aligned} \tag{6.4}$$

where the overall coefficient was obtained by assuming the exponent is exact, but not vice versa. The experimental results should be computable from the quantum mechanical polarization [134, 135] and a model of the crystal. Suitable numerical methods would be a useful area of future research. The exponent is significantly nonperturbative and the anisotropy is significant.

6.5. Coherence Length Not Observed

The coherence length and beam-sample geometry impact the efficiency of harmonic generation. A coherence length of 10 μm is expected for cuprous oxide [139]. A wedge

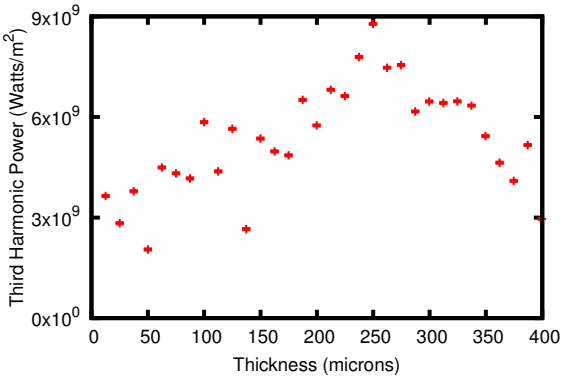

Figure 6.6. Thickness dependence of third harmonic generation at room temperature. The pump power is about 5×10^{15} W/m^2.

shaped sample was fabricated from a synthetic crystal that was grown from 99.99% Cu [76]. The shape of the sample was determined with a profilometer. The wedge was designed to examine coherence lengths [140, 141] between 6 and 300 μm. However, a lack of beating (from destructive interference within the third harmonic) showed that the coherence length is not in the range I examined (Figure 6.6). In retrospect, this portion of the experiment would have benefited from an investigation of the spectral phase of the pump.

6.6. Luminescence

The wedge-shaped sample was cooled to 2.7 Kelvin and the luminescence spectrum caused by third harmonic absorption was measured in the transmission geometry using a 1,400 nm pump (Figure 6.7 (a)) where the sample was 0.3 mm thick. In this pumping and detection configuration, the primary luminescence is caused by decay of an orthoexciton into a photon and a Γ_{12}^- phonon. The luminescence does not form a beam. The spectrum yields the time-averaged thermal distribution of excitons. The time averaged effective exciton temperature, which is distinct from the lattice temperature, was determined by

comparing the Maxwell-Boltzmann distribution (Equation 5.1) to the spectrum. The dependence of the intensity of the luminescence, as determined from the model, on the fundamental laser peak irradiance follows a power law with exponent 1.8 ± 0.2 (Figure 6.7 (b)), consistent with the z-scan results [6]. Exciton decay into luminescence is not necessarily linear in exciton density [29, 42]. The effective exciton temperature (Figure 6.7 (c)) should be higher under more intense excitation.

6.7. Conclusions

A scheme has been developed for reducing three photon processes when only two-photon absorption is desired which involves π phase shifting half the pump photons [12]. No specific claims are made about the size of the reduction. Assuming third harmonic generation dominates over photoionization (Chapter 7), Result 6.4 shows that

$$2\left(\frac{1}{2}\right)^{2.32} = 40\% \tag{6.5}$$

of the third harmonic generation remains.

Cuprous oxide is a promising material for applications that require optical third harmonic generation while simultaneously having a low second harmonic background. To my knowledge, no conventional second harmonic generation has been observed in cuprous oxide crystals, despite extensive studies of two-photon absorption.

Third harmonic generation can also be used as a diagnostic tool for cuprous oxide. The study of stress traps for excitons in cuprous oxide has been a popular field of research [113, 142, 39]. The potentials of these traps can be mapped out by utilizing the localized nature of tomographic third harmonic generation absorption microscopy. Inclusions

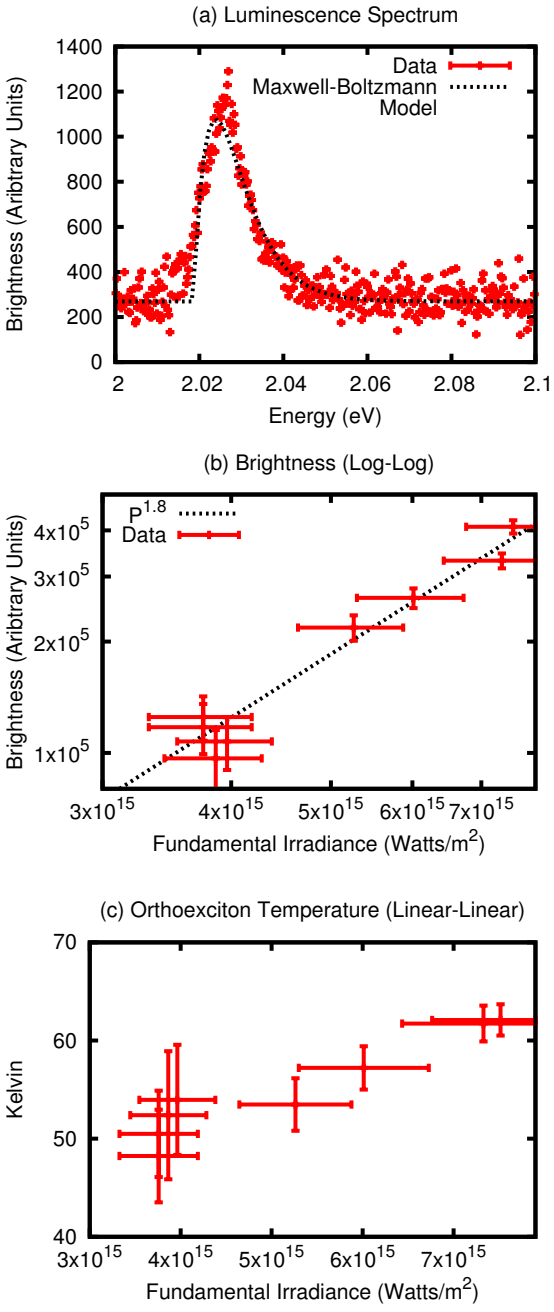

Figure 6.7. (a) Luminescence spectrum from three photon absorption of 1400 nm light, using the highest laser power. (b) Log-Log representation of the dependence of the luminescence intensity as determined from a Maxwell-Boltzmann model on various laser peak irradiances. (c) Linear representation of the dependence of the temperature of the exciton gas on various laser peak irradiances.

[86] commonly induce stress in the crystal (Chapter 5), which can also be measured by determining the resulting localized shift in exciton energy levels.

In conclusion I wish to point out that most third harmonic studies involve cascaded $\chi^{(2)}$ processes [143]. Cuprous oxide is an interesting example of a purely $\chi^{(3)}$ system. Previously, at low temperature the transparent region of cuprous oxide was inaccessible to third harmonic studies. Strong signals have now been observed in that region. Here third harmonic generation in cuprous oxide has been explored, including absolute intensity measurements. The anisotropy of the harmonic generation in this cuprite structured crystal has been shown to follow the cubic crystal pattern. The results will be useful for exciton studies and, possibly, applications based on third harmonic generation or, more generally, $\chi^{(3)}$.

CHAPTER 7

Exciton Photoionization

7.1. Introduction

In the experiments reported in this chapter photon pairs from a 1,220 nm pump pulse were combined through a narrow resonance in a cuprous oxide single crystal to produce propagating 2.0335 eV (609.71 nm) orthoexciton-polaritons. Preparing the excitons via two photon absorption ensures they are in a well defined, non-thermal state. Previous studies of two photon absorption in cuprous oxide hinted at the existence of a photoionization process. The process was masked, however, by:

(1) third harmonic generation [12, 144] (Chapter 6)

(2) Auger exciton-exciton annihilation [42]

(3) identical pump and probe photons.

To distinguish between these processes I apply, in addition to the 1.016 eV pump pulse, a temporally and energetically distinct 1,064 nm probe pulse (Figure 7.1) along the same crystal axis. The purpose of the probe pulse is to ionize excitons generated by the pump pulse. This contrasts with Terahertz spectroscopy of Lyman transitions [145–148, 12], where the electron and hole typically remain bound. The probe pulse is not directly absorbed in the absence of the pump.

I measure the time averaged, transmitted quadrupole exciton-polariton population, which only samples those excitons permitted to decay by the selection rules [8, 149].

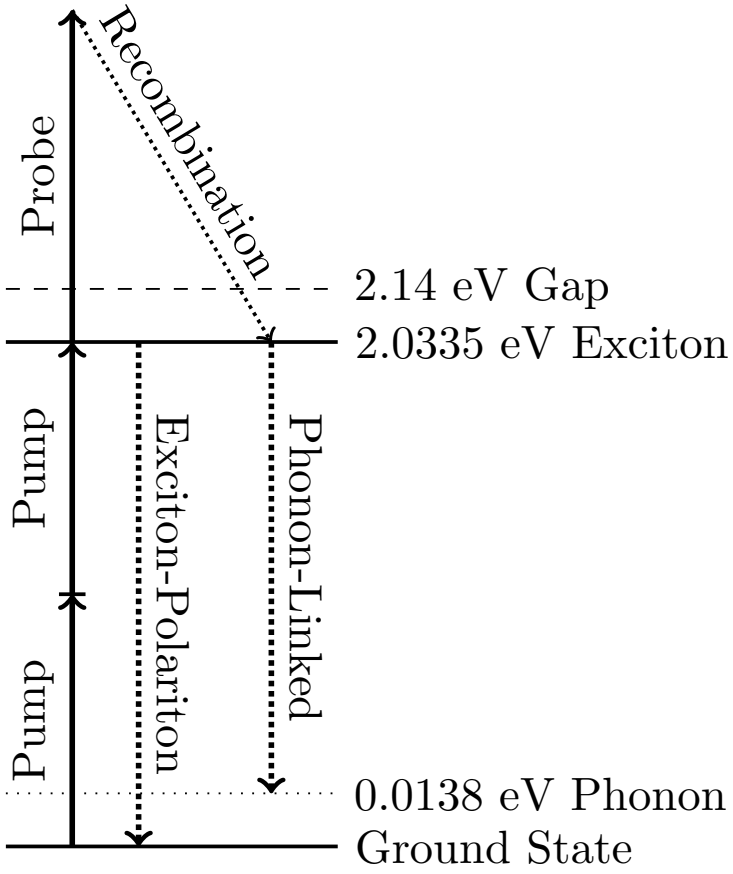

Figure 7.1. Energy level diagram illustrating two photon absorption of the pump, scattering of the exciton, nonradiative electron/hole recombination, phonon-linked luminescence, and exciton-polariton luminescence.

The probe beam strongly attenuates the quadrupole orthoexciton-polaritons. The action of the probe is illustrated in Figure 7.2. Furthermore, this attenuation depends on the temporal positioning of the probe pulse. Auger recombination is excluded through the use of a probe photon which does not produce excitons. $\chi^{(3)}$ processes are also ruled out when the pump and probe are temporally separated.

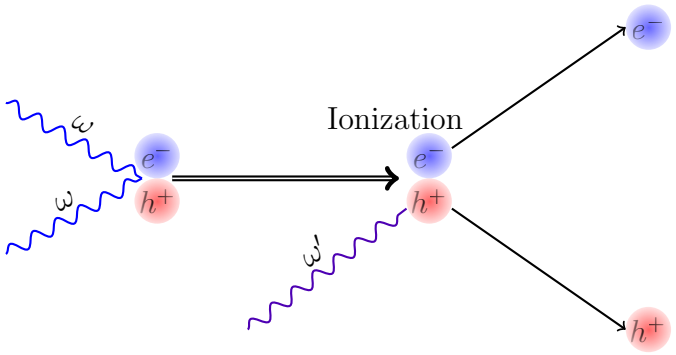

Figure 7.2. An illustration of exciton photoionization.

As a simple model, I will regard the exciton as a hydrogenic atom for which the ionization cross section of the *1s* state is given by [150]

$$\sigma = \frac{h a_0}{\mu c}\frac{2^9\pi}{3}\frac{e^{-4\frac{v_0}{v}\arctan\left(\frac{v}{v_0}\right)}}{\left(1+\frac{v^2}{v_0^2}\right)^4\left(1-e^{-2\pi\frac{v}{v_0}}\right)} \tag{7.1}$$

where

$$\frac{v^2}{v_0^2} = \frac{h\nu}{\mathrm{Ry}} - 1 \tag{7.2}$$

Here h is Planck's constant, $a_0 = 0.79$ to 1.11 nm is the exciton Bohr radius [148], $\mu = 4 \times 10^{-31}$ kg is the reduced effective mass [151], c is the speed of light, $h\nu$ is the photon energy, and Ry= 97 meV is the exciton Rydberg energy [151]. At the probe photon energy the measured cross section is $(3.9 \pm 0.2) \times 10^{-22}$ m^2, which is larger than the range for the hydrogenic atom model of 1.3 to 2.7×10^{-23} m^2 (depending on the value of the Bohr radius) and, in addition, about 7.5 times larger than the reported values for *p*-terphenyl [152] and anthracene [153]. The cross section is only $(5 \pm 2) \times 10^{-26}$ m^2 in tetracene [154]. The hydrogenic model depends on the energy of the photon. This is illustrated in Figure 7.3. The cross section determined here only applies to excitons in

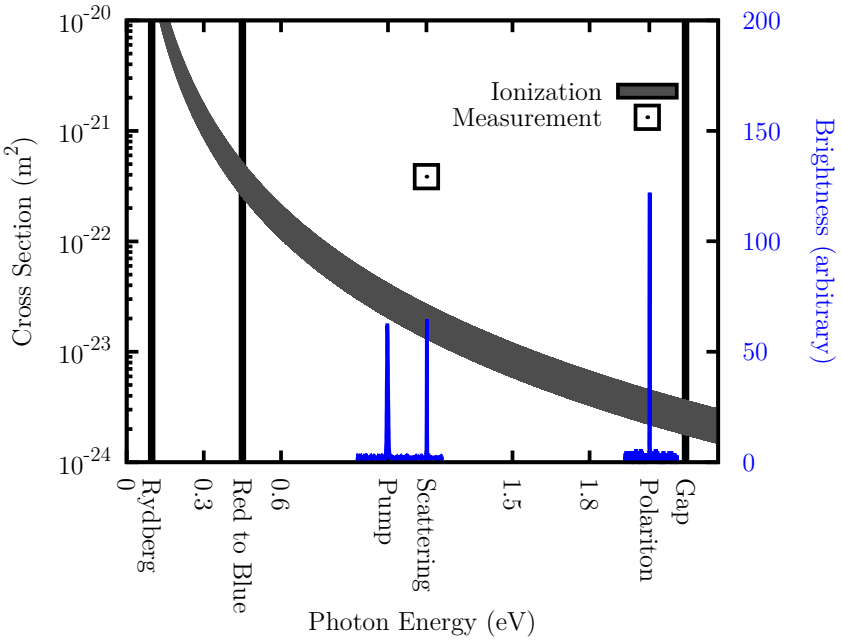

Figure 7.3. The theoretical ionization scattering cross section for a Rydberg exciton. The diagonal band shows the calculated scattering cross section decreases as the scattering photon energy gets bigger. The width represents the range of possible Bohr radius values. If the photon energy is less than the Rydberg energy, no scattering is possible. If it is above the bandgap, the photon will be absorbed rapidly, probably preventing detection of any scattering process. The square in the center shows the actual measured cross section, which is considerably larger than the calculated value. Blue data show the spectrum of the polariton luminescence, and of the two laser beams used. The laser spectra are determined through second harmonic generation produced by β-barium borate. Energy reference points are drawn as vertical bars on the figure. The Rydberg is the binding energy in a hydrogenic model. "Red to Blue" is the energy of the previously reported transition from the yellow exciton to the blue exciton state [15]. The final bar marks the bandgap.

the population sampled through polariton luminescence, which is highly collimated in the forward direction; it includes all processes caused by the probe beam which diminish the size of that population.

7.2. Photon Scattering Methods

The experiment is illustrated in Figure 7.4. There is a photograph in Figure 7.5. The frequency-tripled output of a mode-locked EKSPLA PL2143SS Nd:YAG laser is used to pump an optical parametric amplifier (OPA). The frequency tripling is achieved using two β-barium borate crystals. The first crystal creates the second harmonic. The second crystal creates the sum frequency of the fundamental and the second harmonic, which is the third harmonic. The beam then proceeds to the OPA. The full width half maximum (FWHM) pulse duration is $(5.4 \pm 0.5) \times 10^{-11}$ s, which is determined by sum-frequency cross-correlation of the pump and probe in β-barium borate. It is assumed to be the same for both pulses. The repetition rate is 10 Hz.

At the two-photon resonance energy of 1.016 eV (1220 nm), the spectral bandwidth of the linearly polarized idler output of the OPA has a FWHM of 9.28 meV, far broader than the line width of the orthoexciton-polariton. The idler passed through a Newport 10RP52-3 achromatic 1/2 waveplate and a 200 mm N-BK7 lens.

The 1.165 eV (1,064 nm) probe beam is obtained directly from the Nd:YAG laser. The beam is filtered using a Semrock 532 nm long pass filter which removes leaking second harmonic generation in the laser beam. Next, it passes through a 1,064 nm 1/2 waveplate. The beam travels through several mirrors and down a 60 cm Newport New Focus delay rail with a right angle prism, coated with gold on the two perpendicular surfaces, used as a retroreflector.

The delay line was aligned using a nearly closed iris and a photodiode located several meters beyond the delay line. By moving the delay line back and forth, and repeatedly adjusting the mirrors before the delay line so that the photodiode voltage was maximized,

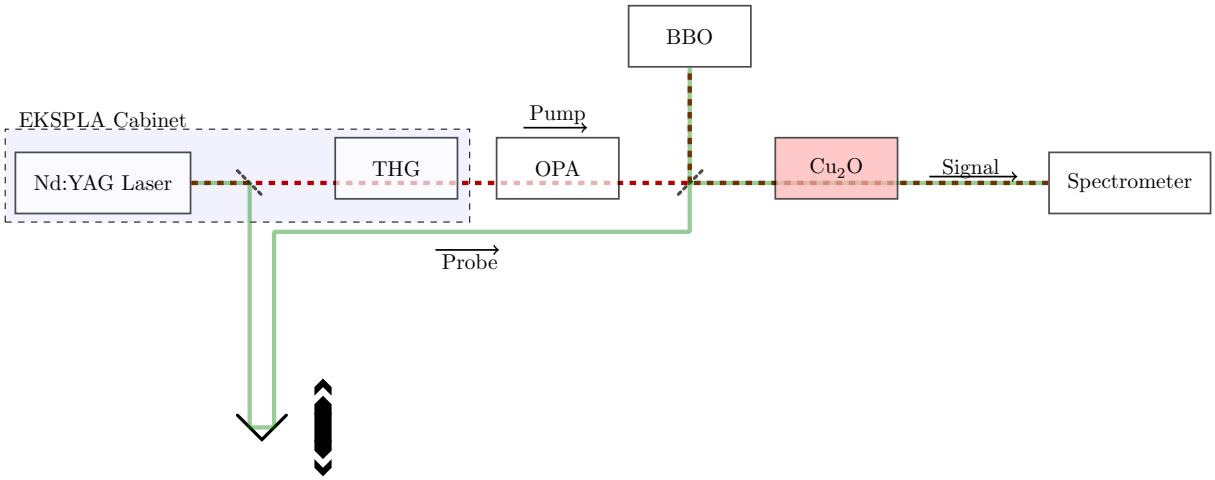

Figure 7.4. Photoionization experiment diagram. The laser beam is split internally. The branch shown at the top is converted to third harmonic by cascade sum frequency generation (THG) and then sent to an optical parametric amplifier (OPA). The OPA idler beam is tuned to half the *1s* orthoexciton energy. The other branch is delayed. The beam branches recombine, with half passing through the cuprous oxide sample and the other half applied to a β-Barium Borate (BBO) or a power meter in the reference arm.

the pointing stability of the delay line could be optimized. Typical accuracies were a few milliradians.

For power dependence measurements, a polarizer (Thorlabs PBS253 polarizing beam-splitter) is placed after the delay line and the waveplate is used to vary the laser power. The beam passes through a 300 mm lens. The probe beam is joined with the pump beam in a 50:50 nonpolarizing Thorlabs BS015 beam combiner, with half the combined beam proceeding to the sample through two alignment mirrors with normal incidence.

A near-field 0.52 mm radius aperture was used to select the center of the beam so that the sample was illuminated approximately uniformly, which also assists in the alignment. The sample was submerged in superfluid helium at 1.4 ± 0.5 K (Figure 7.6). The orthoexciton-polariton beam was measured in transmission and averaged across laser

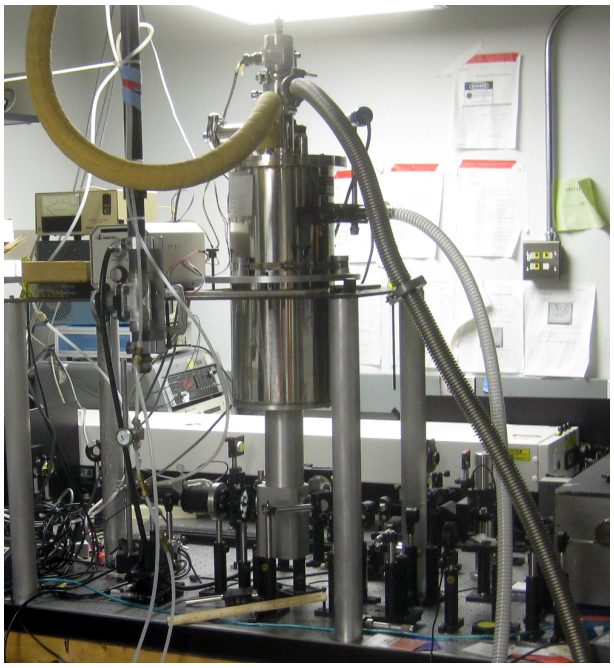

Figure 7.5. A photograph of the apparatus shortly after completion of the experiments.

shots with an Andor 303 mm focal length Czerny-Turner spectrograph and DU420A-BEX2-DD thermoelectric cooled CCD camera. The second half of the combined beam was monitored, after a matched aperture, using a Coherent 1110743 power meter or a β-barium borate sum frequency generator, slightly phase mismatched for each of the three sum frequencies. A custom made Stellarnet spectrometer was used to measure the sum frequencies.

7.3. Results

The presence of the probe beam resulted in a substantial reduction in the observed exciton-polariton luminescence (Figure 7.7). The shape of the exciton-polariton spectrum, which is instrument resolution limited, showed no change during probing (Figure 7.12). The magnitude of the exciton luminescence depends on the spectrum of the photons in

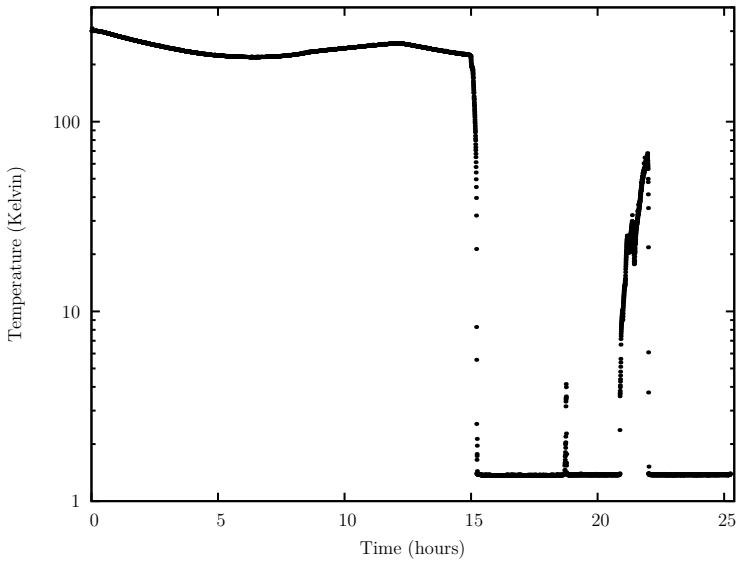

Figure 7.6. Temperature of the sample silicon diode thermometer during liquid nitrogen precooling, submersion in liquid helium during the experiment, and during two periods when the cryostat was refilled with helium. The sample temperature is very stable during the experiment.

the pump beam, but the cross section was independent of the mean pump photon energy (Section 7.7, Figure 7.13). This is expected because the pumped and detected states remain the same, though their occupation changes.

The number and spin of the excitons produced by the pump beam depend on the propagation direction and polarization of the pump relative to the crystal axes [8]. The cross section is observed to be nearly independent of the polarization of the pump or probe beams, in contrast with third harmonic generation (Section 6.3.2). The scattering measurements from two propagation directions were consistent with spherically symmetric target particles (Section 7.8).

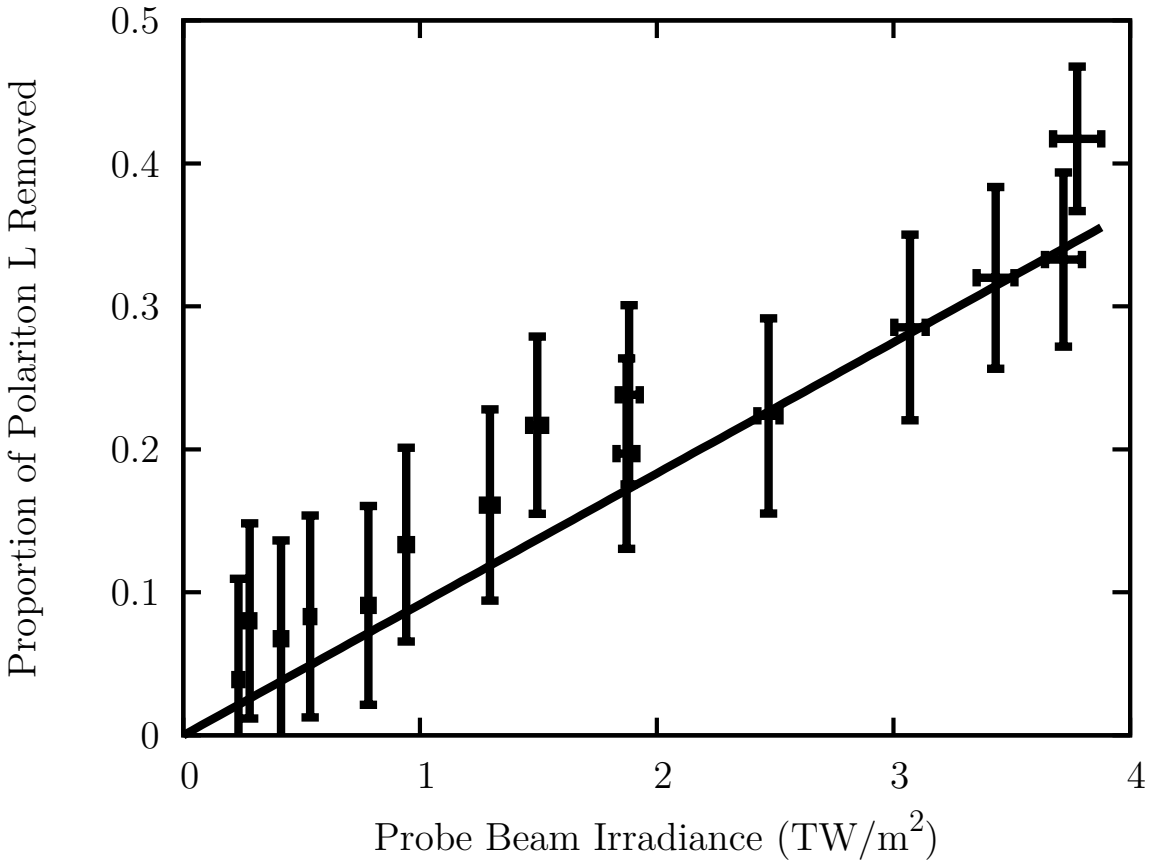

Figure 7.7. Exciton photoscattering. The proportion of the transmitted luminescence that was removed increased linearly with the number of incident photons.

An average heating of the sample by the laser was ruled out as a cause of the reduction in exciton luminescence by varying the laser pulse rate. No change in the scattering cross section was observed (Section 7.9).

The probe pulse decreases the brightness of the exciton-polariton luminescence. As the number of probe photons in each pulse increased, the proportion of the luminescence that was removed increased linearly (Figure 7.7); here N_i is the number of incident photons in the probe laser pulse and L is the wavelength-integrated exciton-polariton luminescence

intensity with the probe beam on (L_{on}) or off (L_{off}). For a working area $\mathcal{A}$, the cross section (Figure 7.8) is

$$\sigma = \frac{\mathcal{A}}{N_i}\left(1 - \frac{L_{\text{on}}}{L_{\text{off}}}\right) = (3.9 \pm 0.2) \times 10^{-22}\ \text{m}^2. \tag{7.3}$$

The pump for the data shown in Figures 7.7 and 7.8 is 23.8 μJ per pulse. The probe pulse is delayed 119 ± 1 ps to ensure pump absorption is complete and decay is minimal (Section 7.4). Since the probe pulse arrives after the pump pulse, there is no significant error due to temporal overlap of the pulses. Systematic error owing to emission detected before the probe pulse was kept small. Short term stabilities for the pump and probe beams were 95% and 98% respectively.

The carriers produced via photoionization recombine to produce phonon-linked luminescence, which increased quadratically with the probe beam intensity, as shown in Figure 7.9, because the binding rate is proportional to the product of the carrier densities. This process is evidence for photoionization assisted two exciton decay. In Figure 7.9, the phonon-linked luminescence is reported as a ratio of the measurement with both the pump and the probe to a measurement with the pump alone.

Third harmonic generation [144] from the probe beam can also produce phonon-linked luminescence (Section 6.6). However, no three photon sum frequency generation in the sample was observed by direct detection.

Phonon-linked luminescence is not directed in a beam because recombined excitons have random momentum. Therefore the phonon-linked luminescence was much weaker than the (directed) exciton-polariton luminescence. Excitons which cannot contribute

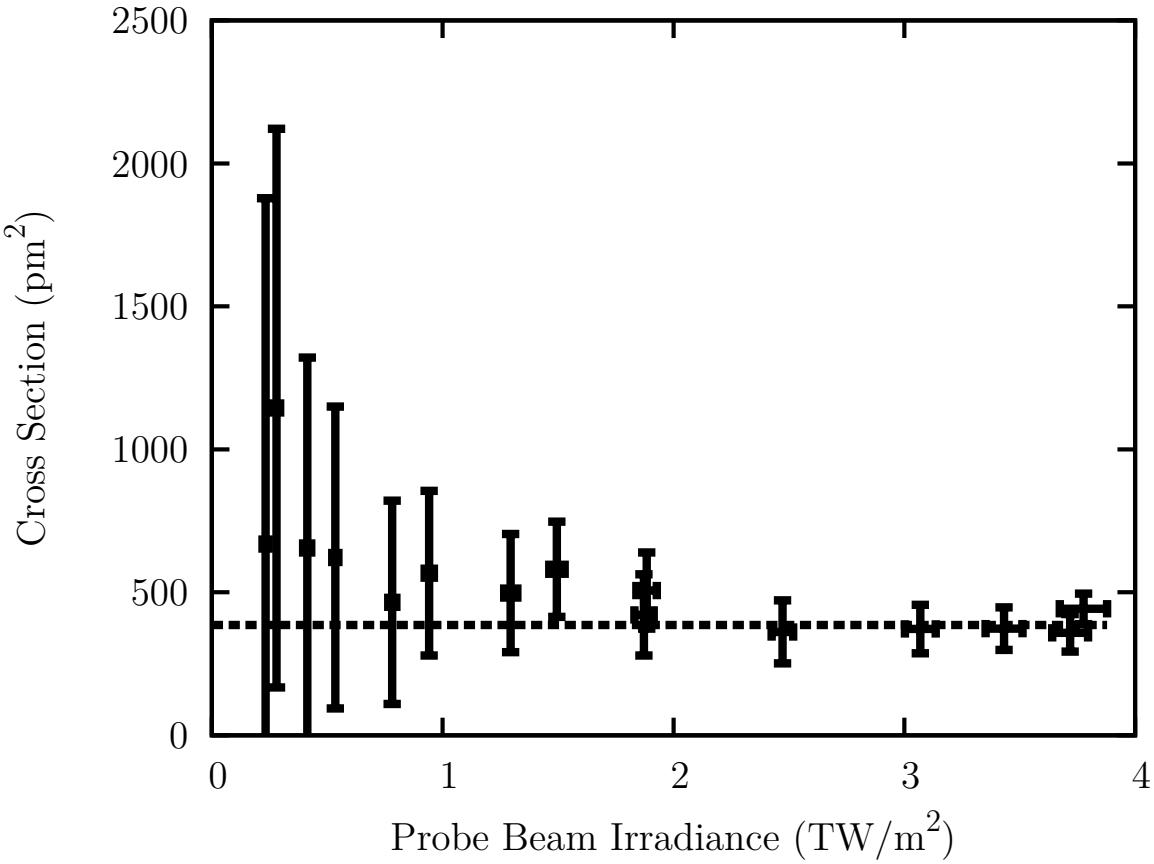

Figure 7.8. Photoionization cross section values associated with Figure 7.7. The average value is marked with a dashed line.

to the polariton signal, such as the paraexciton state, may contribute to the quadratic increase in phonon-linked luminescence if they are ionized.

7.4. Dynamics Through Photoionization

If the ionization pulse arrived before the pump pulse, no ionization occurred (Figure 7.10). If the ionization pulse arrived after the pump pulse, the apparent photoionization cross section decreased rapidly owing to dispersion [111] (and the resulting spread in

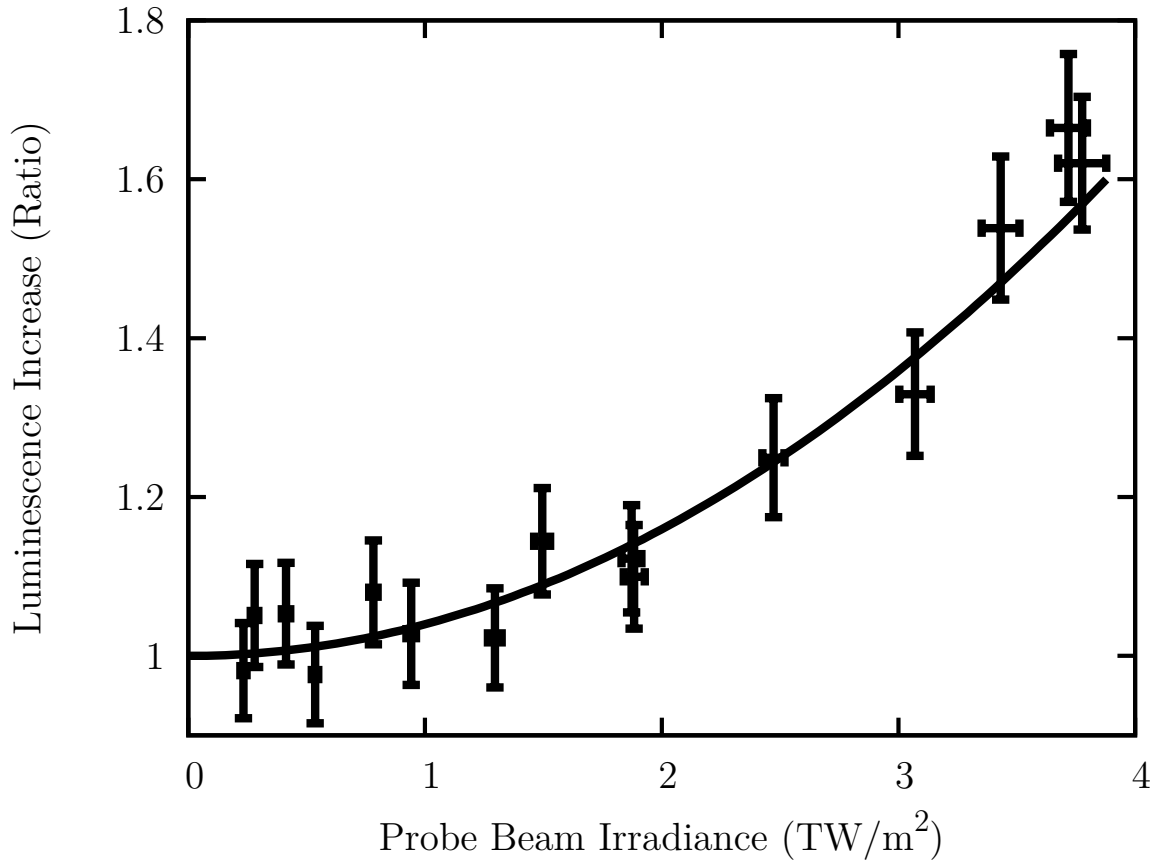

Figure 7.9. Phonon-linked luminescence. The quantity of luminescence increases quadratically with the number of incident phonons since it is a result of the post-ionization decay chain of two excitons.

exciton group velocities) and Auger decay [42, 155, 40] of the exciton-polaritons. A density dependence indicating Auger decay was demonstrated previously under similar conditions [29]. The rise time is explained by the temporal structure of the laser pulses, not by a change in degenerate spin state which can be detected using luminescence [8]. The pump pulse was 25 μJ with a long term standard deviation of 1 μJ. The probe pulse, which is subject to divergence owing to the additional path length used to generate the delay, was 116 μJ with a long term standard deviation of 35 μJ.

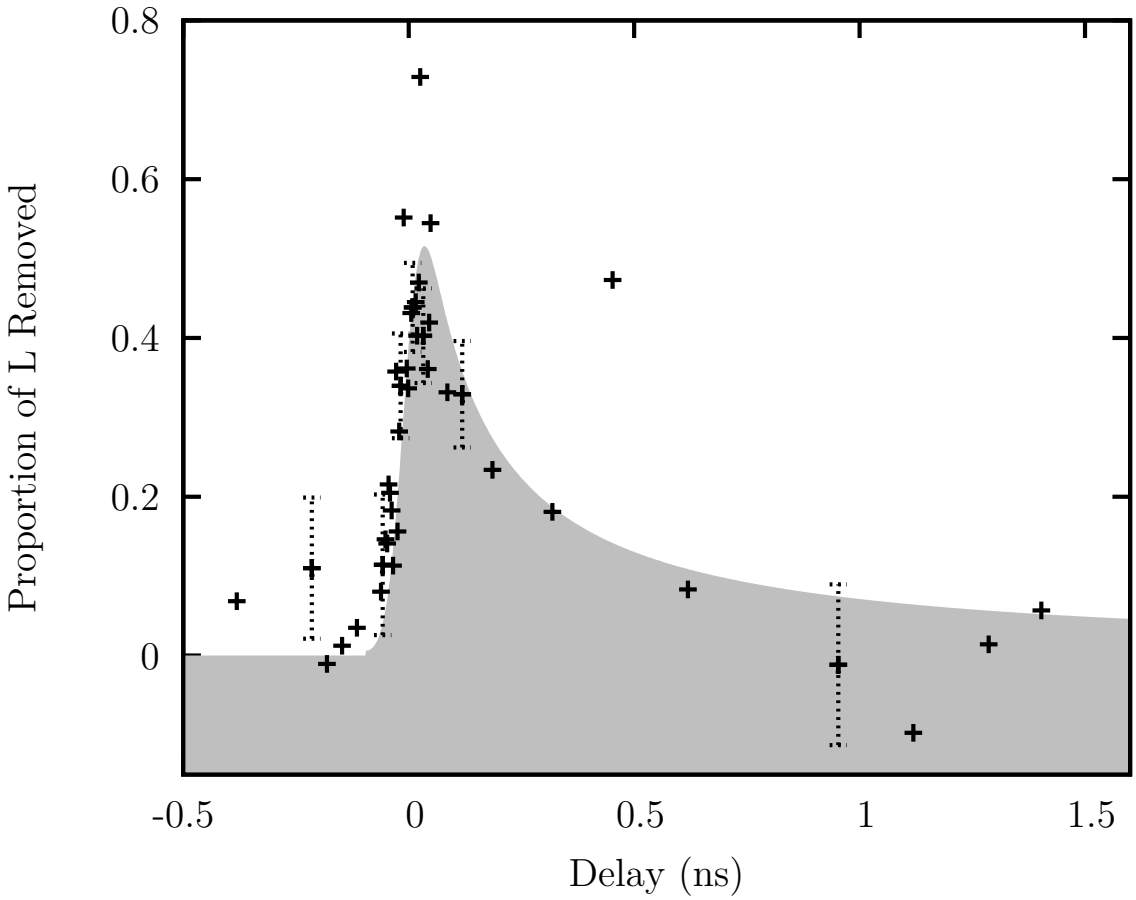

Figure 7.10. Scattering delay. A sample of error bars is shown for clarity. The curve represents pumping with a Gaussian temporal profile followed by Auger decay. An exponential decay could also fit this data.

7.5. Samples

The sample described thus far in this chapter was grown from 0.99999 purity Cu in air, at 4.5 mm/hour with 7 RPM counterrotation. It was cut with [111] faces and annealed at 1045 °C for 5 days with a 5 °C/minute ramp rate. The final sample thickness was 3.988 mm. An additional sample with [100] faces was grown at 3.5 mm/hour and annealed for only 3 days. The thickness was 0.24 mm. This sample was previously reported in [76].

Note that selection rules apply to [100] propagation and that the greater thickness of the [111] sample leads to stronger two photon absorption. Neither sample is perfectly phase pure (Figure 7.11).

7.6. Spectra

Based on a Gaussian model, the polariton peak peak in the luminescence spectrum was at 2.0335 ± 0.0002 eV for a lattice temperature of 1.4 ± 0.5 K (measured with a Lakeshore DT-500CU silicon diode and DRC-82C with logging over GPIB), independent of probe beam scattering (Figure 7.12). Temperature dependence has been investigated [100]. Line widths were resolution limited. Measurements were typically collected in a lower resolution mode, which improved statistics. Luminescence was detected more efficiently by opening the spectrometer entrance slit, thereby increasing the sensitivity of the instrument. The resulting decrease in the instrument resolution did not allow for the exciton temperature to be measured by fitting the phonon-linked luminescence spectrum. In this case the polariton brightness L was determined by integrating from 2.029 eV to 2.038 eV. The phonon-linked luminescence was integrated from 2.016 to 2.026 eV. Photon exciton scattering has no effect on the spectrum shape. It is interesting to compare the spectra in Figures 4.1, 5.3, 6.7(a), and 7.12 to see the difference made by the momentum-conserving nature of two photon absorption.

7.7. Pumping

The photon scattering cross section is independent of the pump beam spectrum. The state pumped by two photon absorption is presumed to be independent of the pump photon energy and spectral phase, provided there is absorption [31].

Figure 7.11. Top: Sample with [111] faces with side view illustration. The green arrow in the illustration indicates the viewpoint of the microscope image and the direction of laser propagation. The blue arrow in the illustration indicates the direction of crystal growth ([100]). The black lines in the illustration represent the opaque, cupric oxide coated surface of the crystal, which forms after annealing as the crystal cools. Bottom: Sample with [100] faces.

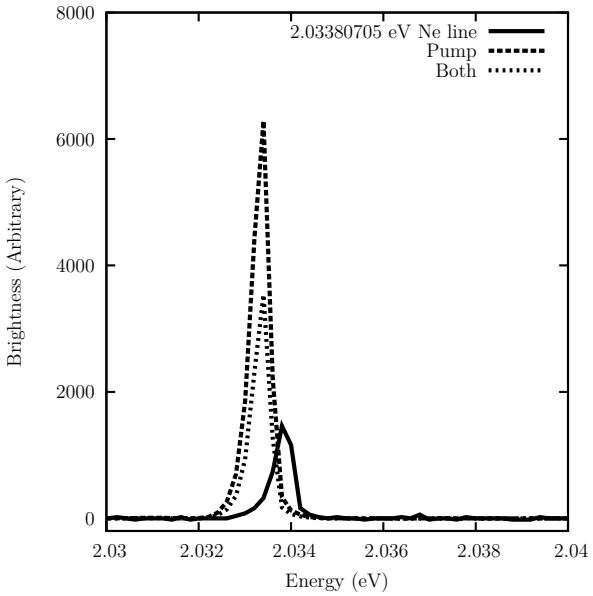

Figure 7.12. Exciton-polariton luminescence spectrum, with pump beam only and with both pump and scattering beam. A neon spectral line is used to confirm calibration [7]. The neon brightness is not comparable, and the line widths are resolution limited.

The pump spectrum center was adjusted using the OPA (Figure 7.13). No change in the cross section was found in the small region where there is absorption. Only the luminescence brightness is influenced by the pump laser spectral overlap with the absorption resonance. The bars indicate laser standard deviation line width, not uncertainty. The pump spectra were determined by second harmonic generation using a β-barium borate crystal. The upper curve is a Gaussian fit. For the lower curve, which includes the scattering beam, only the amplitude is fitted; the other parameters remain the same. The peak pump photon energy lies below half the luminescence energy, but the discrepancy can be explained by systematic uncertainties. A resolution-limited luminescence spectrum is shown. In all other measurements reported in this chapter, the optimal pump photon energy is used.

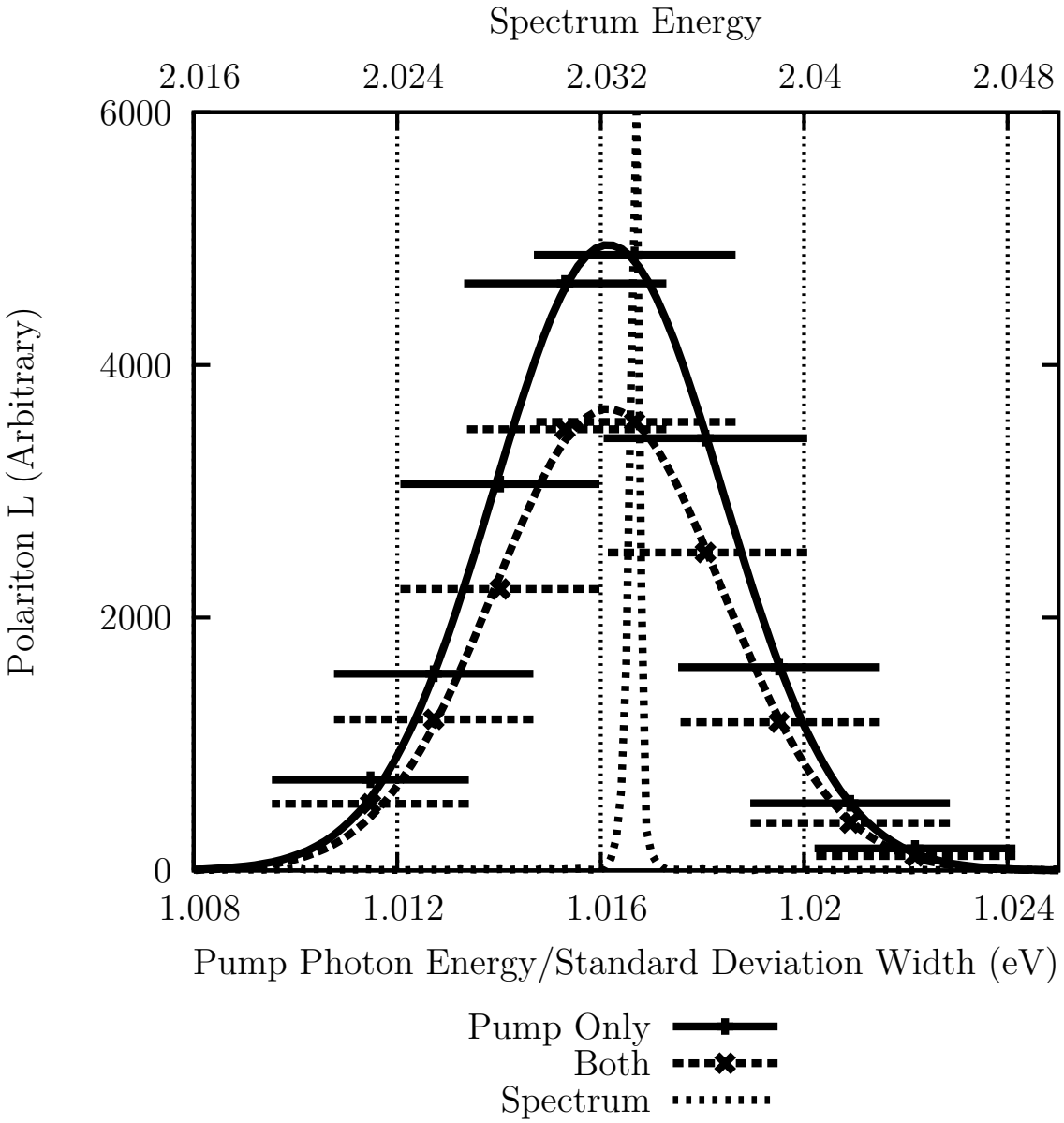

Figure 7.13. Exciton-polariton luminescence brightness as a function of two photon pumping energy with and without the scattering beam. Bars are the standard deviation pump beam spectral width, not the uncertainty in the mean energy.

7.8. Selection Rules

The selection rules for two photon absorption have been previously investigated [8, 149]. Since the *1s* orthoexciton is spherically symmetric, the scattering is independent of polarization. Figures 7.14 and 7.15 show no significant change in the cross section as a function of pump laser polarization for [100] and [111] beam propagation respectively. Figure 7.16 shows no significant change in cross section with the polarization of the scattering beam for [111] propagation.

There has been extensive interest in cooling excitons to form a Bose-Einstein condensate. Phase and polarization methods (Section 6.3.2) of reducing heating of the exciton gas owing to third harmonic generation have been developed [12, 144]. Results show the photon scattering process cannot be manipulated through polarization. Optical heating of the exciton gas is best minimized by keeping the pump irradiance low or spatially separating it from the excitons being studied. On the other hand, photoionization absorption will be a simpler, if destructive, alternative to Lyman spectroscopy for imaging exciton gases [146, 148].

7.9. Laser Pulse Rate

The scattering cross section is independent of laser pulse rate (Figure 7.17). The pulse rate was varied using the laser's software frequency divider, which produces pulse rates of the type $10/n$ Hz. If the laser pulses resulted in an average heating of the sample, the intensity of the luminescence would droop below the expected linear dependence at high pulse rate.

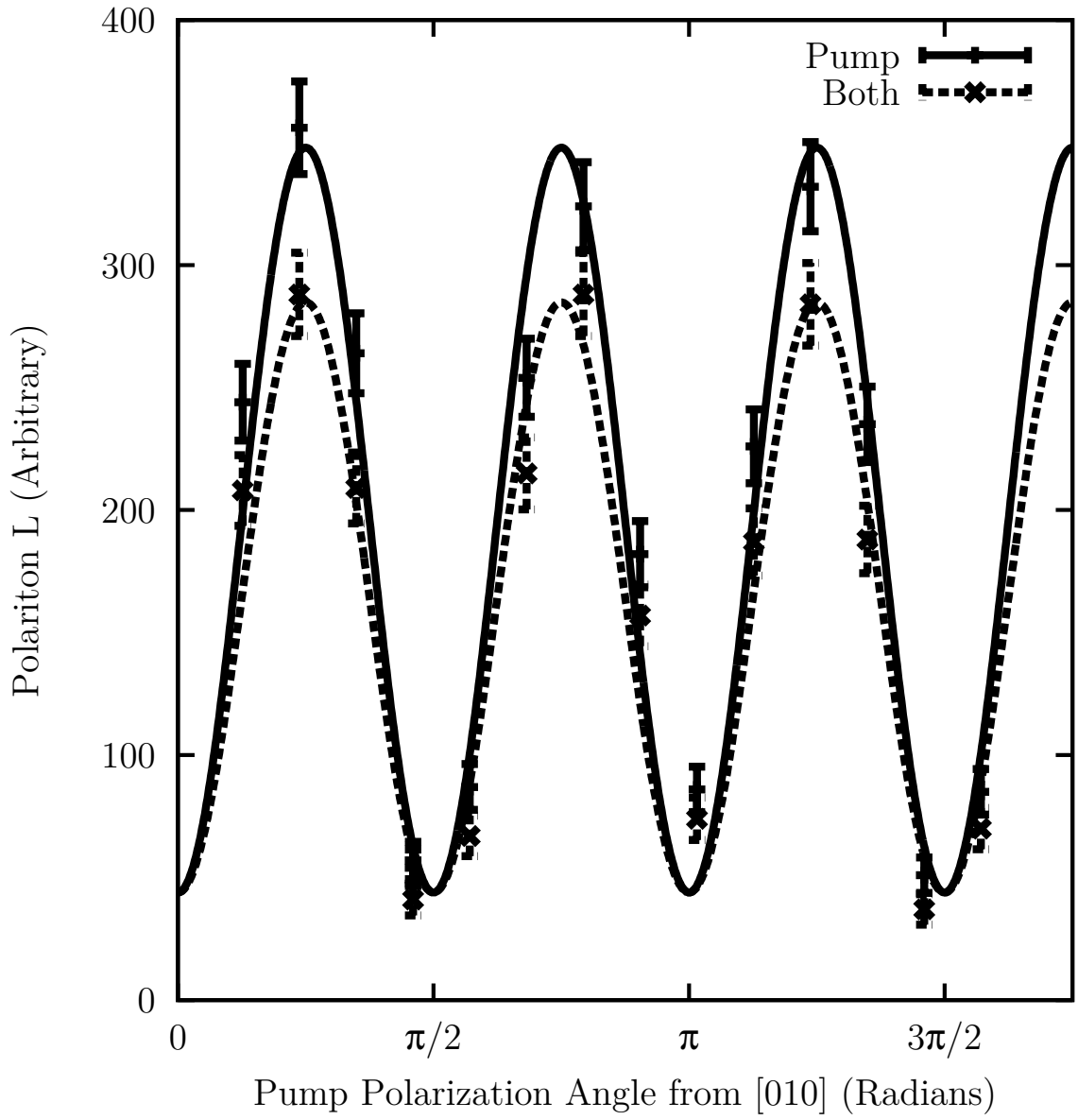

Figure 7.14. For [100] incidence, scattering is independent of the polarization of the pump photon. The curves show the selection rule [8] with two different brightnesses. The difference between the data produced using only the pump beam and the data produced with both a pump and a probe beam arises from a fixed proportion of the exciton-polaritons that are scattered by the probe beam.

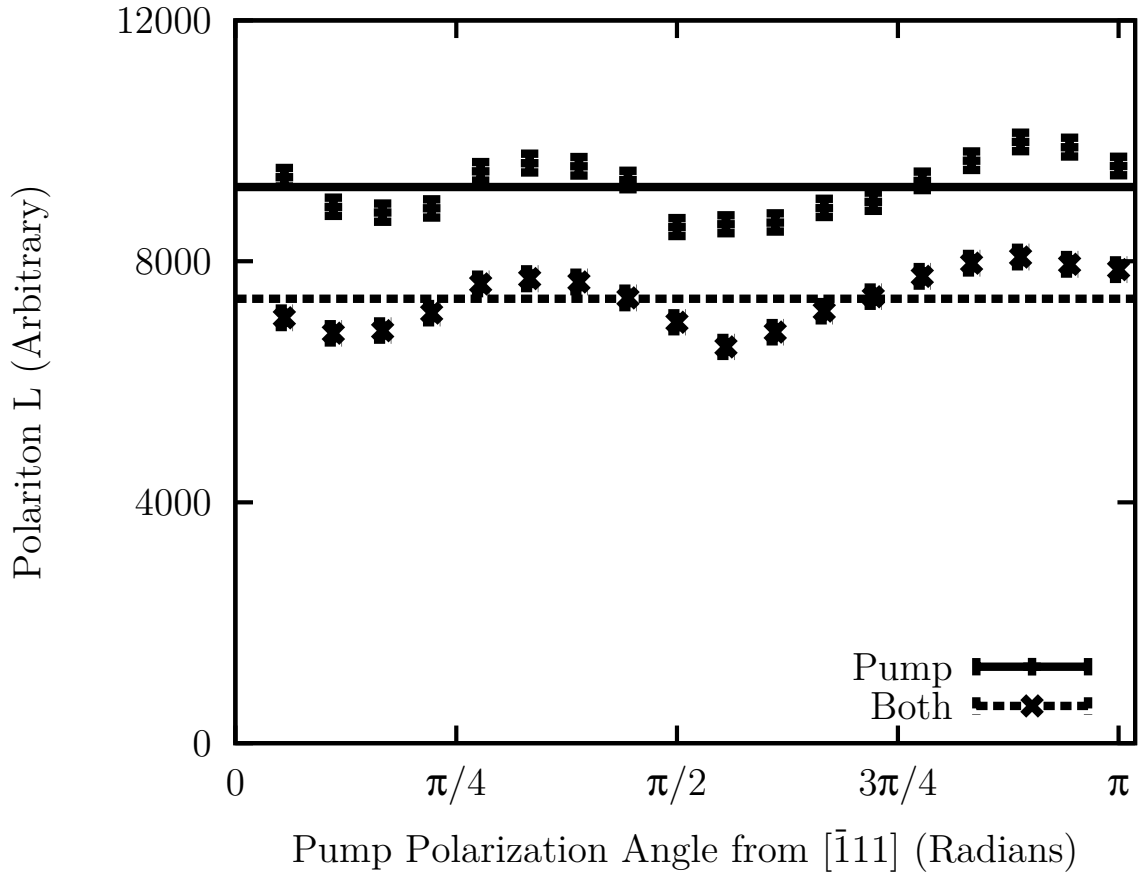

Figure 7.15. For [111] incidence, both two photon absorption and photoscattering are essentially independent of the polarization of the pump photon.

7.10. Time Resolved Luminescence

Time resolved luminescence measurements were collected in order to provide a qualitatively dramatic demonstration of the photoionization phenomenon. The starting point for the experiment was a regeneratively amplified 2 kHz 35 fs Ti:Sapphire pulsed laser as in Chapters 4 and 6. The laser beam was split. Each half of the beam passed through an OPA. The first OPA was set to a signal wavelength of 1,220 nm to produce a two photon

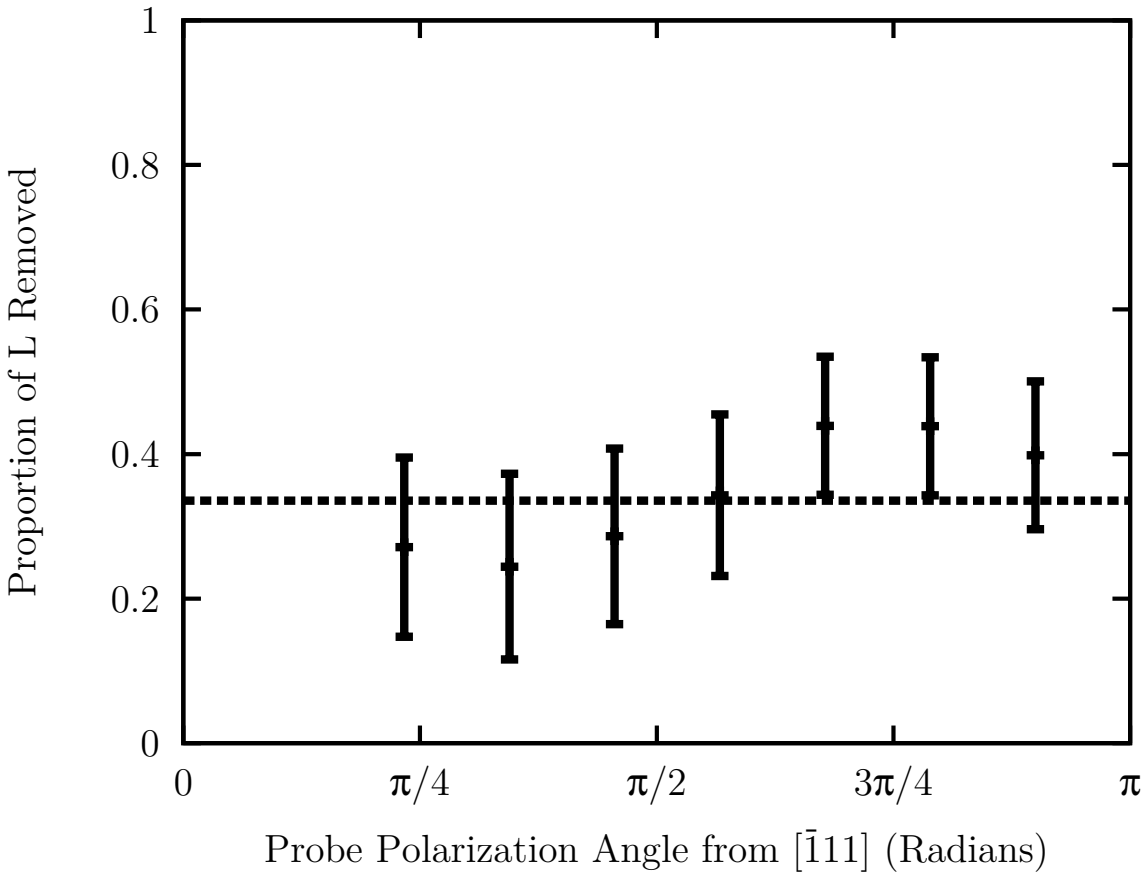

Figure 7.16. Measurements showing that the scattering cross section is independent of the polarization of the probe photon. This example is for [111] incidence.

absorption pump beam. The idler was spatially separated and dumped. The pump was 26 mW. The second OPA was set to an idler wavelength of 2,080 nm, so that the third harmonic would not be absorbed. This probe beam was passed through a 1,550 nm long pass dielectric filter. The probe beam was 17 mW.

Both beams were focused through a Thorlabs AC254-150-C-ML 150 mm achromatic lens. The pump spot size was 170±10 μm in diameter. The probe beam was 510±40 μm in diameter. Unlike the experiment to measure the photoionization cross section, the beams

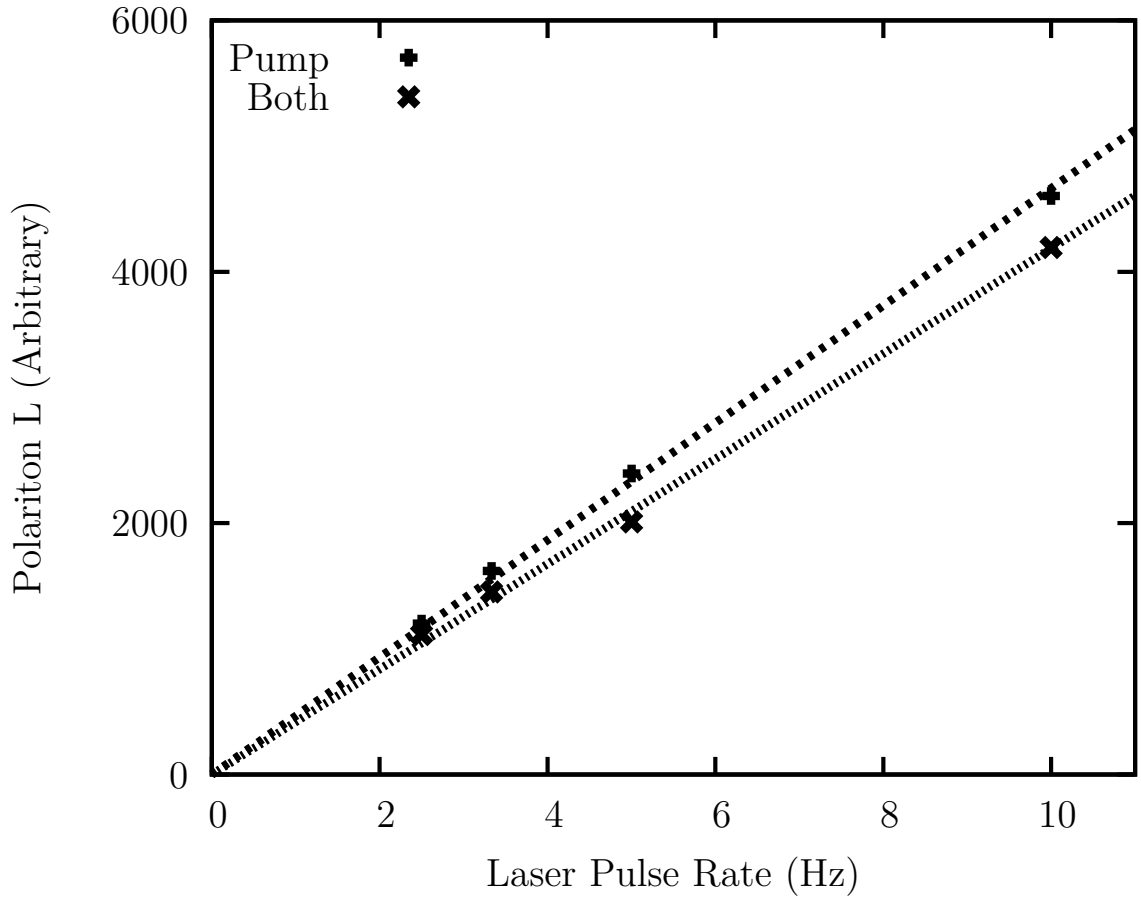

Figure 7.17. The polariton intensity vs. laser pulse rate showing that the luminescence intensity increases linearly.

were not made precisely collinear nor was an aperture used. As a time-saving measure, the pump/probe overlap is therefore not precisely defined in this section. Since the pump beam passes through a periscope and the probe does not, the beam polarizations are the same despite one being a signal and the other an idler.

The sample used is the [111] oriented sample described in Section 7.5. It was mounted with a [111] axis parallel to the polarization of both beams. The sample was in vacuum at 2.9 Kelvin. Luminescence was collected in transmission with a 150 mm spectrograph

containing a 150 groves/mm grating and a streak camera with a 125 ps time window. In this configuration the streak camera time resolution is about 5 ps. The spectral accuracy of the spectrograph is about 10 nm at best. The polariton and phonon-linked luminescence cannot be resolved.

Figure 7.18 shows the time resolved exciton luminescence. The long wavelength, brief band at about 70 ps is the third harmonic generation (Chapter 6) from the probe laser. The spectrally narrow, long duration signal near 620 nm is the exciton luminescence. The spectrally broad pulse at 20 ps is of unknown origin, but is coincident with the arrival of the pump pulse.

Figure 7.19 shows wavelength-integrated data. The exciton signal was integrated across the nominal wavelengths of 610 to 625 nm. The harmonic generation was integrated from 647 to 684 nm. Data collected from the pump only and from the probe only are shown for comparison. As expected from my previous results, there is a dramatic reduction in exciton luminescence when the probe arrives. The probe alone produces no luminescence. The probe is much less intense than the pump, so the pump is actually producing a lot of undetected photoionization.

7.11. Local Dynamical Modeling

The traditional model of time resolved exciton luminescence is

$$\frac{dn}{dt} = -\frac{n}{\tau} - An^2 \tag{7.4}$$

This equation and its variants very accurately describe the results of numerous experiments, but is not intended to capture all aspects of exciton physics. For example, it

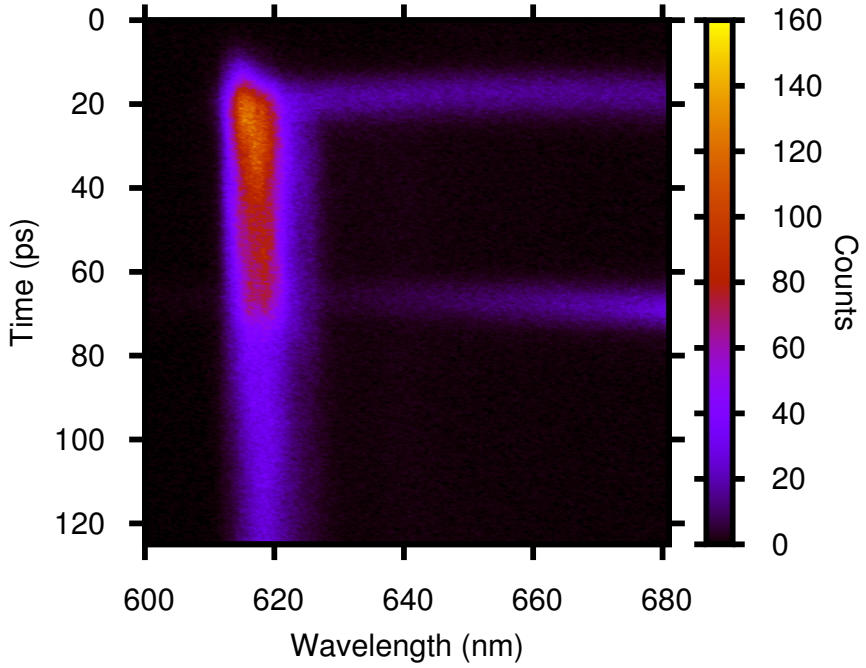

Figure 7.18. Time resolved exciton luminescence with a photoionizing probe. The probe pulse occurs near 70 ps and produces a horizontal band of third harmonic generation. The exciton luminescence is reduced at the same time.

does not describe the spatial distribution or the momentum of excitons, their diffusion, or polariton dispersion. It is purely a description of local exciton losses. Here I illustrate the impact of the exciton/photon scattering cross section on a hypothetical time resolved exciton luminescence experiment.

The equation requires a pumping term and a new term to describe photon scattering. Everything must be defined very carefully.

$$\frac{dn_X}{dt} = -\frac{n_X}{\tau} + \frac{\beta}{2}\iint L(\epsilon_1)L(\epsilon_2)\delta^2(E_{X_O} - \epsilon_1 - \epsilon_2)d\epsilon_1 d\epsilon_2 - An_X^2 - n_X \int \sigma \frac{L}{\epsilon'} d\epsilon' \tag{7.5}$$

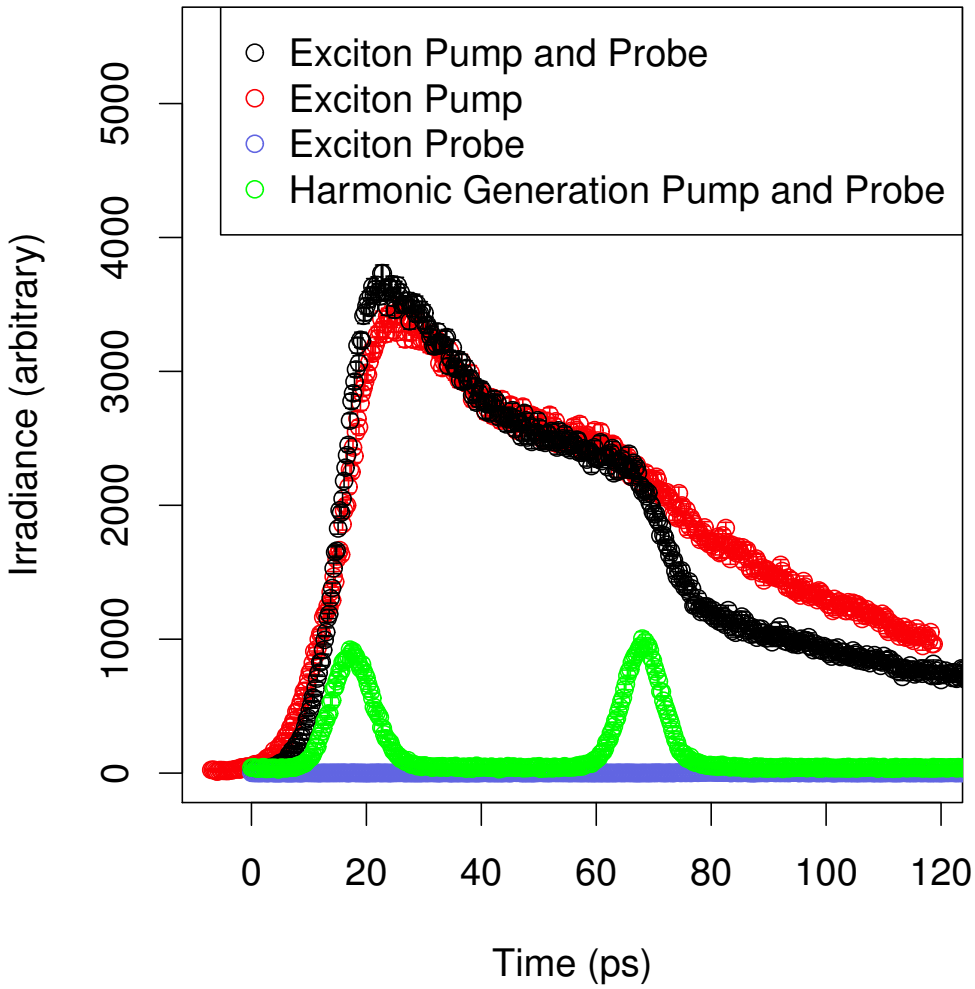

Figure 7.19. Wavelength-integrated, time resolved exciton luminescence. The presence of the probe pulse near 70 ps produces a dramatic reduction in the exciton luminescence (black) compared to luminescence obtained from the pump alone (red). The probe alone produces no exciton luminescence (blue). Long wavelength light indicates the arrival times of the pump and probe (green).

where

- n_X is a number volumetric density of excitons detectable through polariton luminescence

- τ is the intrinsic exciton lifetime including conversion to the lower lying dark paraexciton, radiative decay through the polariton mechanism, and phonon processes
- β is the two photon absorption coefficient [29]. Owing to momentum conservation, two photon absorption only pumps a narrow range of orthoexciton states [8]
- ϵ is the incident photon energy
  - ϵ_1 describes the first photon contributing to two photon absorption
  - ϵ_2 describes the second photon
  - ϵ' describes a photon which may contribute to scattering, such as a pump or probe photon
  - It is necessary to know the total incident spectrum to determine if a photon with a particular energy can contribute to two photon absorption.
- $L(x)$ is the spectral irradiance (energy flux per photon energy)
- δ^2 is an incompletely understood function which maintains conservation laws [30] and has dimensions inverse energy. It does not have zero width like a Dirac delta, but the width is very small by the standards of current experiments.
- E_{X_O} is the orthoexciton energy
- A is the Auger constant [42, 29, 155]
- σ is the ϵ-dependent photon scattering cross section

Interesting pump phase effects have been described [31, 12], but I exclude them from the model as not relevant to photoionization.

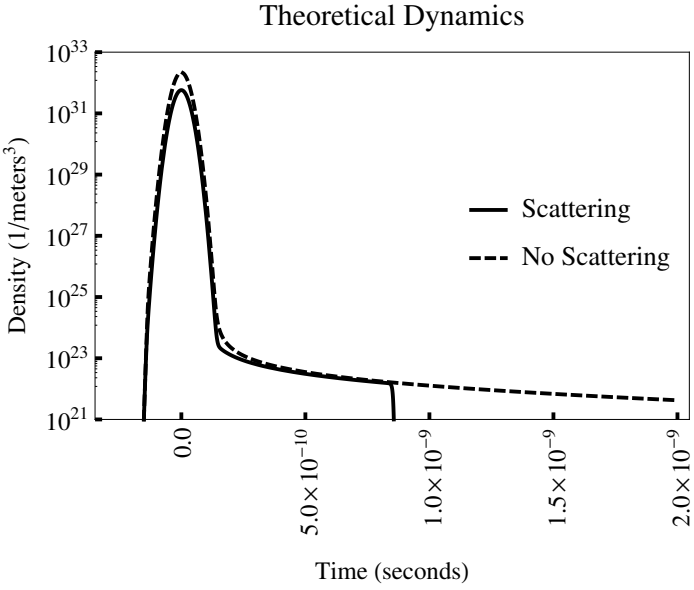

Figure 7.20. Solution to the exciton density differential equation 7.5.

A numerical solution to the differential equation under the delayed scatting pulse conditions used in the experiment shows the effect of photon scattering on the exciton density as a function of time (Figure 7.20). In the calculation, two photon pumping of the orthoexciton is suppressed by both Auger recombination and photon scattering from the pump beam. As the laser beam turns off, the exciton density decreases tracking the laser temporal profile because Auger scattering reduces the exciton population. In other words, the effective exciton lifetime is near zero owing to the high exciton density. After a few tenths of a nanosecond, the population density is small enough that density independent decay processes are more prevalent.

Later, the probe pulse removes much of the exciton population. A calculation with $\sigma = 0$ shows that exciton photon scattering can make a substantial difference. For simplicity, the pump, probe, and polariton are modeled as approximately monochromatic.

The following parameters were used in the numerical calculation.

- $n_X(t = 10^{-6}$ seconds$) = 0$ was used as a boundary condition.
- $\sigma = 3.9 \cdot 10^{-22}$ m^2 for both pump and probe beams
- Laser pulses with Gaussian temporal profiles having standard deviation $2.3 \cdot 10^{-11}$ seconds
- 116 μJ scattering pulses
- 25 μJ pump pulses
- $\beta = 2.17 \cdot 10^{-12}$ m/W
- $\tau = 1.17 \cdot 10^{-9}$ s
- $A = 7 \cdot 10^{-14}$ m^3/s
- The probe pulse is delayed 1 ns

CHAPTER 8

Conclusions and Outlook

This dissertation demonstrates the synthesis of high quality cuprous oxide crystals. There is a large volume of ongoing research on cuprous oxide synthesis, primarily focused on nano- and micromaterials for photocatalysis, photovoltaic, and sensing applications. I hope the defect reduction and sample characterization methods described here will inform future synthesis studies. One pressing question in the field of cuprous oxide synthesis is: How does the electronic structure of cuprous oxide change as material dimensions become small? The methods of Chapter 5 will be useful for answering this question.

While synthetic cuprous oxide lacks some defects found in geological samples and provides greater reproducibility, it does not yet hold the record for longest exciton lifetime. Some additional improvement may be obtained in the future by slower synthesis processes which further drive sample oxidation towards stoichiometry and reduce strain. This will be a tedious line of investigation. There is also some promise in investigating halogen doping at oxygen sites as an oxidation mechanism [78, 79, 81]. Finally, in imitation of natural cuprous oxide formation, hydrothermal growth [156] should be further pursued.

The efficiency of third harmonic generation in cuprous oxide crystals was determined in absolute terms. This is quite unusual for a third harmonic investigation which does not rely on cascading second harmonic generation processes. The anisotropy caused by the tensor nature of the third order susceptibility was measured; the existence of the

anisotropy was predicted but there are no theoretical tools known to me for quantitative predictions. The results emphasize the need for better theoretical methods for time dependent electronic structure calculations in crystals.

Photoionization of excitons is an exciting process to investigate. It has roots in the development of quantum mechanics; the quantization of light was inferred from the energy threshold for the photoelectric effect. It also presents cutting edge challenges in understanding how material band structure modifies the exciton/photon inelastic scattering cross section.

Direct experimental extensions of this work might include measuring the dependence of the cross section on the photon energy to compare it with existing theory (Equation 7.1), alternate pumping schemes, measurements in other materials, and measurements of exciton Rayleigh scattering with terahertz radiation.

More broadly, a good future direction for exciton physics in cuprous oxide is to investigate exciton/phonon scattering processes [23]. Such experiments can be very difficult to control owing to the low energy of phonons, however terahertz technology [157] for phonon applications [142], such as coherent excitation of phonons, is rapidly advancing.

References

[1] Christian Sandfort, Jan Brandt, Christoph Finke, Dietmar Fröhlich, Manfred Bayer, Heinrich Stolz, and Nobuko Naka. Paraexcitons of Cu_2O confined by a strain trap and high magnetic fields. *Physical Review B*, 84(16):165215, 2011.

[2] GM Kavoulakis and G. Baym. Auger decay of degenerate and Bose-condensed excitons in Cu_2O. *Physical Review B*, 54(23):16625, 1996.

[3] GM Kavoulakis and A. Mysyrowicz. Auger decay, spin exchange, and their connection to Bose-Einstein condensation of excitons in Cu_2O. *Physical Review B*, 61(24): 16619, 2000.

[4] JI Jang and JP Wolfe. Biexcitons in the semiconductor Cu_2O: An explanation of the rapid decay of excitons. *Physical Review B*, 72(24):241201, 2005.

[5] JI Jang and JP Wolfe. Exciton decay in Cu_2O at high density and low temperature: Auger recombination, spin-flip scattering, and molecule formation. *Solid State Communications*, 137(1-2):91–96, 2006.

[6] S.E. Mani, J.I. Jang, and J. B. Ketterson. Large third-order susceptibility and third-harmonic generation in centrosymmetric Cu_2O crystal. *Optics Letters*, 34 (18):2817–2819, 2009.

[7] A. Kramida, Yu. Ralchenko, J. Reader, and NIST ASD Team. NIST Atomic Spectra Database (ver. 5.1), [Online]. Available: `http://physics.nist.gov/asd` [2013, December 22]. National Institute of Standards and Technology, Gaithersburg, MD.,

2013.

[8] K. Yoshioka and M. Kuwata-Gonokami. Dark excitons in Cu_2O crystals for two-photon coherence storage in semiconductors. *Physical Review B*, 73(8):081202, 2006.

[9] JH Apfel and LN Hadley. Exciton absorption in cuprous oxide. *Physical Review*, 100:1689–1691, 1955.

[10] LH Tjeng, MBJ Meinders, J Van Elp, J Ghijsen, GA Sawatzky, and RL Johnson. Electronic structure of Ag_2O. *Physical Review B*, 41(5):3190, 1990.

[11] A. Mysyrowicz, D. Hulin, and A. Antonetti. Long exciton lifetime in Cu_2O. *Physical Review Letters*, 43(15):1123–1126, 1979.

[12] Takuro Ideguchi, Kosuke Yoshioka, Andre Mysyrowicz, and Makoto Kuwata-Gonokami. Coherent quantum control of excitons at ultracold and high density in Cu_2O with phase manipulated pulses. *Physical Review Letters*, 100(23):233001, 2008.

[13] YWPH Petroff, PY Yu, and YR Shen. Study of photoluminescence in Cu_2O. *Physical Review B*, 12(6):2488, 1975.

[14] Y Yu Peter and YR Shen. Resonance Raman studies in Cu_2O . I. The phonon-assisted 1 s yellow excitonic absorption edge. *Physical Review B*, 12(4):1377, 1975.

[15] Johannes Schmutzler, Dietmar Fröhlich, and Manfred Bayer. Signatures of coherent propagation of blue polaritons in Cu_2O. *Physical Review B*, 87(24):245202, 2013.

[16] Oleksiy Roslyak, Upali Aparajita, Joseph L Birman, and Shaul Mukamel. Coherent manipulation of quadrupole biexcitons in cuprous oxide by 2d femtosecond spectroscopy. *physica status solidi (b)*, 249(3):435–447, 2012.

[17] AI Bobrysheva and SA Moskalenko. Biexcitons in crystals with large orthopara-exciton splitting. *physica status solidi (b)*, 119(1):141–146, 1983.

[18] WF Brinkman, TM Rice, and Brian Bell. The excitonic molecule. *Physical Review B*, 8(4):1570, 1973.

[19] Wei-Teh Huang. Binding energy of excitonic molecules in isotropic semiconductors. *physica status solidi (b)*, 60(1):309–317, 1973.

[20] Shahin Engakkattil Mani. *Nonlinear optical studies on cuprous oxide using two-photon excitation*. PhD thesis, Northwestern University, 2010.

[21] Pavel A Korzhavyi and Börje Johansson. *Literature review on the properties of cuprous oxide Cu_2O and the process of copper oxidation*. Swedish Nuclear Fuel and Waste Management Company, 2011.

[22] Keith E OHara and JP Wolfe. Relaxation kinetics of excitons in cuprous oxide. *Physical Review B*, 62(19):12909, 2000.

[23] Kosuke Yoshioka, Yusuke Morita, Kenta Fukuoka, and Makoto Kuwata-Gonokami. Generation of ultracold paraexcitons in cuprous oxide: A path toward a stable Bose-Einstein condensate. *Physical Review B*, 88(4):41201, 2013.

[24] Keith O'Hara. *Relaxation Kinetics of Excitons in Cuprous Oxide*. PhD thesis, University of Illinois at Urbana-Champaign, 1999.

[25] Philip W Baumeister. Optical absorption of cuprous oxide. *Physical Review*, 121 (2):359, 1961.

[26] D. Fröhlich, A. Kulik, B. Uebbing, A. Mysyrowicz, V. Langer, H. Stolz, and W. von der Osten. Coherent propagation and quantum beats of quadrupole polaritons in Cu_2O. *Physical Review Letters*, 67(17):2343–2346, 1991.

[27] Jan Brandt, Dietmar Fröhlich, Christian Sandfort, Manfred Bayer, and Heinrich Stolz. Paraexciton polariton propagation beats in cuprous oxide. *physica status solidi (c)*, 6(2):556–559, 2009.

[28] Y. Liu. *Excitons at high density in Cuprous Oxide and coupled quantum wells*. PhD thesis, University of Pittsburgh, 2004.

[29] S. Mani, JI Jang, and JB Ketterson. Nonlinear optical processes at quadrupole polariton resonance in Cu_2O as probed by a Z-scan technique. *Physical Review B*, 82(11):113203, 2010.

[30] Joon I Jang. *Optoelectronics - Materials and Techniques*, chapter Cuprous Oxide (Cu_2O): A Unique System Hosting Various Excitonic Matter and Exhibiting Large Third-Order Nonlinear Optical Responses. InTech, 2011.

[31] Kosuke Yoshioka, Ken Miyashita, and Makoto Kuwata-Gonokami. Selective generation of ultracold high-density *1s* orthoexcitons in Cu_2O with phase-modulated pulse using acousto-optic programmable filter. *Optics Express*, 22(3):3261–3270, 2014.

[32] H-R Trebin, HZ Cummins, and JL Birman. Excitons in cuprous oxide under uniaxial stress. *Physical Review B*, 23(2):597, 1981.

[33] G Dasbach, D Fröhlich, R Klieber, D Suter, M Bayer, and H Stolz. Wave-vector-dependent exchange interaction and its relevance for the effective exciton mass in Cu_2O. *Physical Review B*, 70(4):045206, 2004.

[34] A. Jolk, M. Jörger, and C. Klingshirn. Exciton lifetime, Auger recombination, and exciton transport by calibrated differential absorption spectroscopy in Cu_2O. *Physical Review B*, 65(24):245209, 2002.

[35] O'Hara, KE and Gullingsrud, JR and Wolfe, JP. Auger decay of excitons in Cu_2O. *Physical Review B*, 60(15):10872, 1999.

[36] Warren, JT and O'Hara, KE and Wolfe, JP. Two-body decay of thermalized excitons in Cu_2O. *Physical Review B*, 61(12):8215, 2000.

[37] S. Denev and D. W. Snoke. Stress dependence of exciton relaxation processes in Cu_2O . *Phys. Rev. B*, 65(8):085211, Feb 2002.

[38] JI Jang and JP Wolfe. Auger recombination and biexcitons in Cu_2O: A case for dark excitonic matter. *Physical Review B*, 74(4):045211, 2006.

[39] R. Schwartz, N. Naka, F. Kieseling, and H. Stolz. Dynamics of excitons in a potential trap at ultra-low temperatures: paraexcitons in Cu_2O. *New Journal of Physics*, 14 (2):023054, 2012.

[40] K. Yoshioka, T. Ideguchi, A. Mysyrowicz, and M. Kuwata-Gonokami. Quantum inelastic collisions between paraexcitons in Cu_2O. *Physical Review B*, 82(4):041201, 2010.

[41] JI Jang and JB Ketterson. Suppression of molecule formation for orthoexciton-polaritons in Cu_2O. *Solid State Communications*, 146(3-4):128–132, 2008.

[42] Laszlo Frazer, Richard D Schaller, and JB Ketterson. Unexpectedly slow two particle decay of ultra-dense excitons in cuprous oxide. *Solid State Communications*, 2013.

[43] Zhen Zhang, Wenbin Hu, Yida Deng, Cheng Zhong, Haoren Wang, Yating Wu, and Lei Liu. The effect of complexing agents on the oriented growth of electrodeposited microcrystalline cuprous oxide film. *Materials Research Bulletin*, 47(9):2561–2565, 2012.

[44] Ming Yang, Xiaoqi Jin, and Qiao Huang. Electrochemical glucose oxidation on dendritic cuprous oxide film fabricated by pss-assisted electrochemical deposition. *Solid State Sciences*, 13(2):427–433, 2011.

[45] Wilman Septina, Shigeru Ikeda, M Alam Khan, Takeshi Hirai, Takashi Harada, Michio Matsumura, and Laurence M Peter. Potentiostatic electrodeposition of cuprous oxide thin films for photovoltaic applications. *Electrochimica Acta*, 56(13):4882–4888, 2011.

[46] Flora M Li, Rob Waddingham, William I Milne, Andrew J Flewitt, Stuart Speakman, James Dutson, Steve Wakeham, and Mike Thwaites. Low temperature ($<$ 100° C) deposited p-type cuprous oxide thin films: Importance of controlled oxygen and deposition energy. *Thin Solid Films*, 520(4):1278–1284, 2011.

[47] Dewi Suriyani, Che Halin, Abu Talib Ibrahim, Abd Razak Daud, and Muhammad Azmi. Cuprous oxide thin films for a photoelectrochemical cell of ITO/Cu_2O/PVC$-LiClO_4$/graphite. *Advanced Materials*, 2012.

[48] Jung Joon Yoo, Jin Yu, Jae Yong Song, and Yeonjin Yi. Single-walled carbon nanotubes as a dopant in p-type cuprous oxide films. *Carbon*, 49(8):2659–2664, 2011.

[49] Zhigang Zang, Atsushi Nakamura, and Jiro Temmyo. Nitrogen doping in cuprous oxide films synthesized by radical oxidation at low temperature. *Materials Letters*, 2012.

[50] Yun Seog Lee, Mark T Winkler, Sin Cheng Siah, Riley Brandt, and Tonio Buonassisi. Hall mobility of cuprous oxide thin films deposited by reactive direct-current magnetron sputtering. *Applied Physics Letters*, 98(19):192115–192115, 2011.

[51] Anna Osherov, Changqiong Zhu, and Matthew J Panzer. Role of solution chemistry in determining the morphology and photoconductivity of electrodeposited cuprous oxide films. *Chemistry of Materials*, 25(5):692–698, 2013.

[52] Chinchun Ooi and Gregory KL Goh. Formation of cuprous oxide films via oxygen plasma. *Thin Solid Films*, 518(24):e98–e100, 2010.

[53] Jun-Woo Park, Hyungkeun Jang, Sung Kim, Suk-Ho Choi, Hosun Lee, Joongoo Kang, and Su-Huai Wei. Microstructure, optical property, and electronic band structure of cuprous oxide thin films. *Journal of Applied Physics*, 110(10):103503–103503, 2011.

[54] KMDC Jayathilaka, Vassilios Kapaklis, W Siripala, and JKDS Jayanetti. Sulfidation of electrodeposited microcrystalline/nanocrystalline cuprous oxide thin films for solar energy applications. *Semiconductor Science and Technology*, 27(12):125019, 2012.

[55] Jung-Dae Kwon, Se-Hun Kwon, Tae-Hoon Jung, Kee-Seok Nam, Kwun-Bum Chung, Dong-Ho Kim, and Jin-Seong Park. Controlled growth and properties of p-type cuprous oxide films by plasma-enhanced atomic layer deposition at low temperature. *Applied Surface Science*, 2013.

[56] Shaodong Sun and Zhimao Yang. Recent advances in tuning crystal facets of polyhedral cuprous oxide architectures. *RSC Advances*, 4(8):3804–3822, 2014.

[57] Linfeng Gou and Catherine J Murphy. Solution-phase synthesis of Cu_2O nanocubes. *Nano Letters*, 3(2):231–234, 2003.

[58] Sangeeta Sahoo, Sudhir Husale, Bryant Colwill, Toh-Ming Lu, Saroj Nayak, and Pulickel M Ajayan. Electric field directed self-assembly of cuprous oxide nanostructures for photon sensing. *ACS Nano*, 3(12):3935–3944, 2009.

[59] Xudong Liang, Lian Gao, Songwang Yang, and Jing Sun. Facile synthesis and shape evolution of single-crystal cuprous oxide. *Advanced Materials*, 21(20):2068–2071, 2009.

[60] Conghua Lu, Limin Qi, Jinhu Yang, Xiaoyu Wang, Dayong Zhang, Jinglin Xie, and Jiming Ma. One-pot synthesis of octahedral Cu_2O nanocages via a catalytic solution route. *Advanced Materials*, 17(21):2562–2567, 2005.

[61] Haolan Xu, Wenzhong Wang, and Wei Zhu. Shape evolution and size-controllable synthesis of Cu_2O octahedra and their morphology-dependent photocatalytic properties. *The Journal of Physical Chemistry B*, 110(28):13829–13834, 2006.

[62] Yu Chang, Joong Jiat Teo, and Hua Chun Zeng. Formation of colloidal CuO nanocrystallites and their spherical aggregation and reductive transformation to hollow Cu_2O nanospheres. *Langmuir*, 21(3):1074–1079, 2005.

[63] Debao Wang, Maosong Mo, Dabin Yu, Liqiang Xu, Fanqing Li, and Yitai Qian. Large-scale growth and shape evolution of Cu_2O cubes. *Crystal Growth & Design*, 3(5):717–720, 2003.

[64] Jiatao Zhang, Junfeng Liu, Qing Peng, Xun Wang, and Yadong Li. Nearly monodisperse Cu_2O and CuO nanospheres: preparation and applications for sensitive gas sensors. *Chemistry of Materials*, 18(4):867–871, 2006.

[65] LI Zhang and Hui Wang. Cuprous oxide nanoshells with geometrically tunable optical properties. *ACS Nano*, 5(4):3257–3267, 2011.

[66] Huizhi Bao, Wenhua Zhang, Daili Shang, Qing Hua, Yunsheng Ma, Zhiquan Jiang, Jinlong Yang, and Weixin Huang. Shape-dependent reducibility of cuprous oxide nanocrystals. *The Journal of Physical Chemistry C*, 114(14):6676–6680, 2010.

[67] Praveen Martis, Antonio Fonseca, Zineb Mekhalif, and Joseph Delhalle. Optimization of cuprous oxide nanocrystals deposition on multiwalled carbon nanotubes. *Journal of Nanoparticle Research*, 12(2):439–448, 2010.

[68] Ji Chan Park, Jeonghan Kim, Hyuksang Kwon, and Hyunjoon Song. Gram-scale synthesis of Cu_2O nanocubes and subsequent oxidation to CuO hollow nanostructures for lithium-ion battery anode materials. *Advanced Materials*, 21(7):803–807, 2009.

[69] Xiao-Yan Yan, Xi-Li Tong, Yue-Fei Zhang, Xiao-Dong Han, Ying-Yong Wang, Guo-Qiang Jin, Yong Qin, and Xiang-Yun Guo. Cuprous oxide nanoparticles dispersed on reduced graphene oxide as an efficient electrocatalyst for oxygen reduction reaction. *Chemical Communications*, 48(13):1892–1894, 2012.

[70] W Zh Wang, GH Wang, X Sh Wang, YJ Zhan, YK Liu, and Ch L Zheng. Synthesis and characterization of Cu_2O nanowires by a novel reduction route. *Advanced Materials*, 14(1):67–69, 2002.

[71] Zorica Crnjak Orel, Alojz Anzlovar, Goran Drazic, and Majda Zigon. Cuprous oxide nanowires prepared by an additive-free polyol process. *Crystal Growth & Design*, 7 (2):453–458, 2007.

[72] Xiaofeng Chang, Guangbin Ji, Kai Shen, Lijia Pan, Yi Shi, and Youdou Zheng. Fabrication of nanowire-like cuprous oxide in aqueous solutions of a triblock copolymer. *Journal of Alloys and Compounds*, 482(1):240–245, 2009.

[73] Yueh-Hsun Lee, Ing-Chi Leu, Min-Tao Wu, Jung-Hsien Yen, and Kuan-Zong Fung. Fabrication of Cu/Cu_2O composite nanowire arrays on Si via AAO template-mediated electrodeposition. *Journal of Alloys and Compounds*, 427(1):213–218, 2007.

[74] Jia Li, Yu Shi, Qiang Cai, Qianyao Sun, Hengde Li, Xihua Chen, Xiaoping Wang, Yunjie Yan, and EG Vrieling. Patterning of nanostructured cuprous oxide by surfactant-assisted electrochemical deposition. *Crystal Growth and Design*, 8(8): 2652–2659, 2008.

[75] Yong-e Gu, Xu Su, Yongling Du, and Chunming Wang. Preparation of flower-like Cu_2O nanoparticles by pulse electrodeposition and their electrocatalytic application. *Applied Surface Science*, 256(20):5862–5866, 2010.

[76] Kelvin B Chang, Laszlo Frazer, Johanna J Schwartz, John B Ketterson, and Kenneth R Poeppelmeier. Removal of copper vacancies in cuprous oxide single crystals grown by the floating zone method. *Crystal Growth & Design*, 13(11):4914–4922, 2013.

[77] Sandhaya Koirala, Nobuko Naka, and Koichiro Tanaka. Correlated lifetimes of free paraexcitons and excitons trapped at oxygen vacancies in cuprous oxide. *Journal of Luminescence*, 134:524–527, 2013.

[78] Qiong Bai, Weichao Wang, Qiming Zhang, and Meng Tao. n-type doping in Cu_2O with F, Cl, and Br: A first-principles study. *Journal of Applied Physics*, 111(2): 023709, 2012.

[79] Zhao Zong-Yan, Yi Juan, and Zhou Da-Cheng. Electronic structures of halogen-doped Cu_2O based on dft calculations. *Chinese Physics B*, 23(1):017401, 2014.

[80] Francesco Biccari, Claudia Malerba, and Alberto Mittiga. Chlorine doping of Cu_2O. *Solar Energy Materials and Solar Cells*, 94(11):1947–1952, 2010.

[81] Xiaofei Han, Kunhee Han, and Meng Tao. n-type Cu_2O by electrochemical doping with Cl. *Electrochemical and Solid-State Letters*, 12(4):H89–H91, 2009.

[82] Leah Y Isseroff and Emily A Carter. Electronic structure of pure and doped cuprous oxide with copper vacancies: Suppression of trap states. *Chemistry of Materials*, 25 (3):253–265, 2013.

[83] Y Tsur and I Riess. Impurity solubility limits in ionic crystals, with application to Cu_2O. *Zeitschrift für physikalische Chemie*, 207(1):181–213, 1998.

[84] Dan Trivich and Gordon P Pollack. Preparation of single crystals of cuprous oxide in an arc-image furnace. *Journal of The Electrochemical Society*, 117(3):344–345, 1970.

[85] Gerard Vagnard and J Washburn. Plastic deformation of cuprous oxide. *Journal of the American Ceramic Society*, 51(2):88–88, 1968.

[86] RD Schmidt-Whitley, M Martinez-Clemente, and A Revcolevschi. Growth and microstructural control of single crystal cuprous oxide Cu_2O. *Journal of Crystal Growth*, 23(2):113–120, 1974.

[87] Richard S Zucker. Growth of single crystal cuprous oxide from the melt and luminescence of cuprous oxide. *Journal of The Electrochemical Society*, 112(4):417–420, 1965.

[88] WS Brower and HS Parker. Growth of single crystal cuprous oxide 1. *Journal of Crystal Growth*, 8(3):227–229, 1971.

[89] JL Loison, M Robino, and C Schwab. Progress in melt growth of Cu_2O. *Journal of Crystal Growth*, 50(4):816–822, 1980.

[90] A Haydar and A Coret. Excitonic photoconductivity and structural defects in Cu_2O crystals. *Le Journal de Physique Colloques*, 41(C6):C6–504, 1980.

[91] T. Ito, H. Yamaguchi, K. Okabe, and T. Masumi. Single-crystal growth and characterization of Cu_2O and CuO. *Journal of Materials Science*, 33(14):3555–3566, 1998.

[92] Nicolas J Alvarez, Lynn M Walker, and Shelley L Anna. A non-gradient based algorithm for the determination of surface tension from a pendant drop: Application to low bond number drop shapes. *Journal of Colloid and Interface Science*, 333(2): 557–562, 2009.

[93] PH Keck, M Green, and ML Polk. Shapes of floating liquid zones between solid rods. *Journal of Applied Physics*, 24(12):1479–1481, 1953.

[94] Walter Tiano, Monica Dapiaggi, and Gilberto Artioli. Thermal expansion in cuprite-type structures from 10 K to decomposition temperature: Cu_2O and Ag_2O. *Journal of Applied Crystallography*, 36(6):1461–1463, 2003.

[95] GK White. Thermal expansion of cuprous oxide at low temperatures. *Journal of Physics C: Solid State Physics*, 11(11):2171, 1978.

[96] Klaus-Peter Bohnen, Rolf Heid, Lothar Pintschovius, Aloysius Soon, and Catherine Stampfl. Ab initio lattice dynamics and thermal expansion of Cu_2O. *Physical Review B*, 80(13):134304, 2009.

[97] Karena W Chapman and Peter J Chupas. Anomalous thermal expansion of cuprites: A combined high resolution pair distribution function and geometric analysis. *Chemistry of Materials*, 21(2):425–431, 2009.

[98] BJ Keene. Review of data for the surface tension of pure metals. *International Materials Reviews*, 38(4):157–192, 1993.

[99] Michael O'Keeffe. Infrared optical properties of cuprous oxide. *The Journal of Chemical Physics*, 39:1789, 1963.

[100] Takayuki Ito and Taizo Masumi. Detailed examination of relaxation processes of excitons in photoluminescence spectra of Cu_2O. *Journal of the Physical Society of Japan*, 66(7):2185–2193, 1997.

[101] Y Zhu, K Mimura, and M Isshiki. Oxidation mechanism of Cu_2O to CuO at 600–1050 C. *Oxidation of Metals*, 62(3-4):207–222, 2004.

[102] SM Koohpayeh, D Fort, A Bradshaw, and JS Abell. Thermal characterization of an optical floating zone furnace: A direct link with controllable growth parameters. *Journal of Crystal Growth*, 311(8):2513–2518, 2009.

[103] CW Lan. Three-dimensional simulation of floating-zone crystal growth of oxide crystals. *Journal of crystal growth*, 247(3):597–612, 2003.

[104] Sandhaya Koirala, Mitsuyoshi Takahata, Yuji Hazama, Nobuko Naka, and Koichiro Tanaka. Relaxation of localized excitons by phonon emission at oxygen vacancies in Cu_2O. *Journal of Luminescence*, 155:65–69, 2014.

[105] Caroline A Schneider, Wayne S Rasband, and Kevin W Eliceiri. NIH Image to ImageJ: 25 years of image analysis. *Nature Methods*, 9(7):671–675, 2012.

[106] JI Jang, Y Sun, B Watkins, and JB Ketterson. Bound excitons in Cu_2O: Efficient internal free exciton detector. *Physical Review B*, 74(23):235204, 2006.

[107] P. Dawson, MM Hargreave, and GR Wilkinson. The dielectric and lattice vibrational spectrum of cuprous oxide. *Journal of Physics and Chemistry of Solids*, 34(12): 2201–2208, 1973.

[108] JCW Taylor and FL Weichman. Raman effect in cuprous oxide compared with infrared absorption. *Canadian Journal of Physics*, 49(5):601–605, 1971.

[109] K. Reimann and K. Syassen. Raman scattering and photoluminescence in Cu_2O under hydrostatic pressure. *Physical Review B*, 39(15):11113, 1989.

[110] H. Solache-Carranco, G. Juárez-Díaz, A. Esparza-García, M. Briseño-García, M. Galván-Arellano, J. Martínez-Juárez, G. Romero-Paredes, and R. Peña-Sierra. Photoluminescence and x-ray diffraction studies on Cu_2O. *Journal of Luminescence*, 129(12):1483–1487, 2009.

[111] D Fröhlich, A Kulik, B Uebbing, A Mysyrowicz, V Langer, H Stolz, and W von der Osten. Coherent propagation and quantum beats of quadrupole polaritons in Cu_2O. *Physical Review Letters*, 67(17):2343, 1991.

[112] J.L. Lin and JP Wolfe. Bose-Einstein condensation of paraexcitons in stressed Cu_2O. *Physical Review Letters*, 71(8):1222–1225, 1993.

[113] DP Trauernicht, JP Wolfe, and A. Mysyrowicz. Thermodynamics of strain-confined paraexcitons in Cu_2O. *Physical Review B*, 34(4):2561, 1986.

[114] Kosuke Yoshioka, Eunmi Chae, and Makoto Kuwata-Gonokami. Transition to a Bose-Einstein condensate and relaxation explosion of excitons at sub-Kelvin temperatures. *Nature Communications*, 2:328, 2011.

[115] Y Sun, Kirill Rivkin, J Chen, JB Ketterson, P Markworth, and RP Chang. Strain splitting of *1*s yellow orthoexciton of epitaxial orthorhombic Cu_2O films on MgO [110]. *Physical Review B*, 66(24):245315, 2002.

[116] S Denev and DW Snoke. Stress dependence of exciton relaxation processes in Cu_2O. *Physical Review B*, 65(8):85211, 2002.

[117] James P Wolfe and Joon I Jang. New perspectives on kinetics of excitons in Cu_2O. *Solid State Communications*, 134(1):143–149, 2005.

[118] Hannes Raebiger, Stephan Lany, and Alex Zunger. Origins of the p-type nature and cation deficiency in Cu_2O and related materials. *Physical Review B*, 76(4):045209, 2007.

[119] M Zouaghi, B Prevot, C Carabatos, and M Sieskind. Near infrared optical and photoelectric properties of Cu_2O. III. Interpretation of experimental results. *physica status solidi (a)*, 11(2):449–460, 1972.

[120] Michael O'Keeffe and Walter J Moore. Electrical conductivity of monocrystalline cuprous oxide. *The Journal of Chemical Physics*, 35:1324, 1961.

[121] Robert S Toth, Rein Kilkson, and Dan Trivich. Electrical conductivity of single-crystal cuprous oxide at high temperatures. *Physical Review*, 122(2):482, 1961.

[122] P Ochin, C Petot, and G Petot-Ervas. Thermodynamic study of point defects in $Cu_{2-\delta}O$. electrical conductivity measurements at low oxygen partial pressures. *Solid State Ionics*, 12:135–143, 1984.

[123] O Porat and I Riess. Defect chemistry of $Cu_{2-y}O$ at elevated temperatures. Part II: Electrical conductivity, thermoelectric power and charged point defects. *Solid State Ionics*, 81(1):29–41, 1995.

[124] Junqiang Li, Zenxia Mei, Daqian Ye, Huili Liang, Lishu Liu, Yaoping Liu, Augustinas Galeckas, Andrej Yu Kuznetsov, and Xiaolong Du. Engineering of optically defect free Cu_2O enabling exciton luminescence at room temperature. *Optical Materials Express*, 3(12):2072–2077, 2013.

[125] MY Shen, T. Yokouchi, S. Koyama, and T. Goto. Dynamics associated with Bose-Einstein statistics of orthoexcitons generated by resonant excitations in cuprous oxide. *Physical Review B*, 56(20):13066, 1997.

[126] DW Snoke and JP Wolfe. Picosecond dynamics of degenerate orthoexcitons in Cu_2O. *Physical Review B*, 42(13):7876, 1990.

[127] E Gross, S Permogorov, and B Razbirin. Free exciton motion in crystals and exciton-phonon interaction. *Journal of Physics and Chemistry of Solids*, 27(10):1647–1651, 1966.

[128] WP Dumke. Two-phonon indirect transitions and lattice scattering in Si. *Physical Review*, 118(4):938, 1960.

[129] DM Basko, S Piscanec, and AC Ferrari. Electron-electron interactions and doping dependence of the two-phonon raman intensity in graphene. *Physical Review B*, 80 (16):165413, 2009.

[130] Takahiro Ohkubo, Mitsuhiro Ushio, Koki Urita, Isamu Moriguchi, Bashir Ahmmad, Atsushi Itadani, and Yasushige Kuroda. Nanospace-enhanced photoreduction for the synthesis of copper (I) oxide nanoparticles under visible-light irradiation. *Journal of Colloid and Interface Science*, 421:165–169, 2014.

[131] Shufang Wu, Tianmo Liu, Wen Zeng, Shixiu Cao, Kangguan Pan, Shiyang Li, Yongsong Yan, Jiejun He, Bin Miao, and Xianghe Peng. Octahedral cuprous oxide synthesized by hydrothermal method in ethanolamine/distilled water mixed solution. *Journal of Materials Science: Materials in Electronics*, 25(2):974–980, 2014.

[132] A Labidi, H Ouali, A Bejaoui, T Wood, C Lambert-Mauriat, M Maaref, and K Aguir. Synthesis of pure Cu_2O thin layers controlled by in-situ conductivity measurements. *Ceramics International*, 2014.

[133] A.D. DiChiara, S. Ghimire, C.I. Blaga, E. Sistrunk, E.P. Power, A.M. March, T.A. Miller, D.A. Reis, P. Agostini, and L.F. DiMauro. Scaling of high-order harmonic generation in the long wavelength limit of a strong laser field. *Selected Topics in Quantum Electronics, IEEE Journal of*, 18(1):419–433, 2012.

[134] JJ Macklin, JD Kmetec, and CL Gordon III. High-order harmonic generation using intense femtosecond pulses. *Physical Review Letters*, 70(6):766–769, 1993.

[135] A. LHuillier, P. Balcou, S. Candel, K.J. Schafer, and K.C. Kulander. Calculations of high-order harmonic-generation processes in xenon at 1064 nm. *Physical Review A*, 46(5):2778, 1992.

[136] S. Ghimire, A.D. DiChiara, E. Sistrunk, P. Agostini, L.F. DiMauro, and D.A. Reis. Observation of high-order harmonic generation in a bulk crystal. *Nature Physics*, 7 (2):138–141, 2010.

[137] MY Shen, S. Koyama, M. Saito, T. Goto, and N. Kuroda. Second-harmonic generation resonant to the *1s* orthoexciton level of cuprous oxide. *Physical Review B*, 53 (20):13477, 1996.

[138] JE Sipe, DJ Moss, and HM Van Driel. Phenomenological theory of optical second- and third-harmonic generation from cubic centrosymmetric crystals. *Physical Review B*, 35(3):1129, 1987.

[139] Refractive index database. http://refractiveindex.info, 2013.

[140] G. Boyd, H. Kasper, and J. McFee. Linear and nonlinear optical properties of $AgGaS_2$, $CuGaS_2$, and $CuInS_2$, and theory of the wedge technique for the measurement of nonlinear coefficients. *Quantum Electronics, IEEE Journal of*, 7(12): 563–573, 1971.

[141] G.R. Meredith. Cascading in optical third-harmonic generation by crystalline quartz. *Physical Review B*, 24(10):5522, 1981.

[142] K. Yoshioka and M. Kuwata-Gonokami. Relaxation explosion of a quantum degenerate exciton gas in Cu_2O. *New Journal of Physics*, 14(5):055024, 2012.

[143] D Eimerl, JM Auerbach, CE Barker, D Milam, and PW Milonni. Multicrystal designs for efficient third-harmonic generation. *Optics Letters*, 22(16):1208–1210, 1997.

[144] Laszlo Frazer, Richard D Schaller, Kelvin B Chang, John B Ketterson, and Kenneth R Poeppelmeier. Third-harmonic generation in cuprous oxide: efficiency determination. *Optics Letters*, 39(3):618–621, 2014.

[145] M Jörger, E Tsitsishvili, T Fleck, and C Klingshirn. Infrared absorption by excitons in Cu_2O. *physica status solidi (b)*, 238(3):470–473, 2003.

[146] M. Kubouchi, K. Yoshioka, R. Shimano, A. Mysyrowicz, and M. Kuwata-Gonokami. Study of orthoexciton-to-paraexciton conversion in Cu_2O by excitonic lyman spectroscopy. *Physical Review Letters*, 94(1):16403, 2005.

[147] Makoto Kuwata-Gonokami, Motoyoshi Kubouchi, Ryo Shimano, and Andre Mysyrowicz. Time-resolved excitonic lyman spectroscopy of Cu_2O. *Journal of the Physical Society of Japan*, 73(4):1065–1069, 2004.

[148] Takeshi Tayagaki, Andre Mysyrowicz, and Makoto Gonokami. The yellow excitonic series of Cu_2O revisited by lyman spectroscopy (condensed matter: Electronic structure, electrical, magnetic and optical properties). *Journal of the Physical Society of Japan*, 74(5):1423–1426, 2005.

[149] RJ Elliott. Symmetry of excitons in Cu_2O. *Physical Review*, 124(2):340, 1961.

[150] Harvey Hall. The theory of photoelectric absorption for x-rays and γ-rays. *Reviews of Modern Physics*, 8(4):358, 1936.

[151] Svâtoslav Anatol'evič Moskalenko and David W Snoke. *Bose-Einstein Condensation of Excitons and Biexcitons and Coherent Nonlinear Optics with Excitons*. Cambridge University Press, 2000.

[152] Eizi Morikawa, Yasuo Isono, and Masahiro Kotani. Generation and recombination of charge carriers in p-terphenyl crystal. Photoionization of singlet exciton. *The Journal of Chemical Physics*, 78:2691, 1983.

[153] RG Kepler. Photoionization of excitons in anthracene. *Physical Review Letters*, 18: 951–953, 1967.

[154] P Schlotter, J Kalinowski, and H Bässler. Photoionization of triplet excitons in tetracene crystals. *physica status solidi (b)*, 81(2):521–526, 1977.

[155] KE O'Hara, JR Gullingsrud, and JP Wolfe. Auger decay of excitons in Cu_2O. *Physical Review B*, 60(15):10872, 1999.

[156] He Ying Zhao, Ye Feng Wang, and Jing Hui Zeng. Hydrothermal synthesis of uniform cuprous oxide microcrystals with controlled morphology. *Crystal Growth and Design*, 8(10):3731–3734, 2008.

[157] H Hirori, A Doi, F Blanchard, and K Tanaka. Single-cycle terahertz pulses with amplitudes exceeding 1 MV/cm generated by optical rectification in $LiNbO_3$. *Applied Physics Letters*, 98(9):091106, 2011.

[158] David A Czaplewski, Martin V Holt, and Leonidas E Ocola. The range and intensity of backscattered electrons for use in the creation of high fidelity electron beam lithography patterns. *Nanotechnology*, 24(30):305302, 2013.

[159] LC Olsen, RC Bohara, and MW Urie. Explanation for low-efficiency Cu_2O schottky-barrier solar cells. *Applied Physics Letters*, 34(1):47–49, 1979.

[160] E. Tselepis, E. Fortin, and A. Mysyrowicz. Exciton-mediated photovoltaic effect in Cu_2O/Cu. *Physical Review Letters*, 59(18):2107–2110, 1987.

[161] E. Fortin, S. Fafard, and A. Mysyrowicz. Exciton transport in Cu_2O: Evidence for excitonic superfluidity? *Physical Review Letters*, 70(25):3951–3954, 1993.

[162] E. Benson, E. Fortin, and A. Mysyrowicz. Study of anomalous excitonic transport in Cu_2O. *physica status solidi (b)*, 191(2):345–367, 1995.

[163] Andre Mysyrowicz, Emery Fortin, and Eric Benson. Study of excitonic superfluidity in Cu_2O. In *Excitonic Processes in Condensed Matter: International Conference*, pages 140–150. International Society for Optics and Photonics, 1995.

[164] A. Mysyrowicz, E. Benson, and E. Fortin. Directed beam of excitons produced by stimulated scattering. *Physical Review Letters*, 77(5):896–899, 1996.

[165] N. Naka, M. Hasuo, and N. Nagasawa. Two-photon photo-voltaic spectroscopy on wannier excitons in Cu_2O. *Physics of the Solid State*, 40(5):847–849, 1998.

[166] AE Bulatov and SG Tikhodeev. Phonon-driven carrier transport caused by short excitation pulses in semiconductors. *Physical Review B*, 46(23):15058, 1992.

[167] E. Benson, E. Fortin, and A. Mysyrowicz. Anomalous exciton transport in Cu_2O: Excitonic superfluidity or phonon-wind effect? *Solid State Communications*, 101 (5):313–317, 1997.

[168] SG Tikhodeev. Comment on directed beam of excitons produced by stimulated scattering. *Physical Review Letters*, 78(16):3225, 1997.

[169] G.A. Tikhodeev, S.G. Kopelevich and N.A. Gippius. Exciton transport in Cu_2O: Phonon wind versus superfluidity. *physica status solidi (b)*, 206:45–53, 1998.

[170] SG Tikhodeev, NA Gippius, and GA Kopelevich. Exciton transport in Cu_2O. *physica status solidi (a)*, 178(1):63–68, 2000.

[171] AD Jackson and GM Kavoulakis. Propagation of exciton pulses in semiconductors. *EPL (Europhysics Letters)*, 59(6):807, 2002.

[172] Eric Benson. Study of excitonic superfluidity in Cu_2O. Master's thesis, University of Ottawa, 1995.

[173] S Meskinis, K Slapikas, and S Smetona. Low resistance Al–nGaAs ohmic contacts. *Semiconductor Science and Technology*, 17(9):907, 2002.

APPENDIX A

Preparation of Electronic Detectors

I developed detectors for photovoltaic measurements and a search for exciton solitons which has not been successful thus far. This appendix describes the my electron beam lithography process, which as far as I know is the first one performed on cuprous oxide substrates.

A.1. Sample Requirements

- Bumps must be small compared to the thickness of the resist (< 100 nm).
- Large scale curvature must be such that focus of the electron beam can be maintained or corrected.
- The sample must be hydrophilic so that resist will adhere to it. Cuprous oxide is highly hydrophilic.
- Samples must be strong enough not to fracture during handling, including spin coating ($> 100\mu$m thick).
- Samples are more easily mounted if their thickness is less than 1 mm.
- The sample must be adequately grounded so that it can be imaged for alignment with the electron beam. Though cuprous oxide is not a conductor, this has not been a challenge.

A.2. Device Construction

Exciton detectors require cuprous oxide with copper and gold connections. There also need to be contacts to send the signal to external readout electronics. There are four layers to the design:

(1) Alignment marks

(2) Gold/cuprous oxide interface

(3) Copper/cuprous oxide interface

(4) Contacts

Each layer was made with electron beam lithography and deposition. One electron beam lithography cycle is required for each layer on each cuprous oxide chip. Each chip can contain multiple devices, within the constraint that the devices not interfere with each other. The lithography process is about the same in each case, but the deposition varies.

The alignment mark step crates a reference frame for subsequent deposition steps. I used plus-sign shaped alignment marks. For each device I used two large and two small marks. Only three noncollinear marks are required to perform alignment of the electron beam, but I found that using extra marks was very helpful. Sometimes not all the marks are written correctly. Since the alignment marks are subject to electron beam exposure during the alignment of the remaining three layers, they can be destroyed if the resist on top of the alignment mark is exposed enough that it is removed during development. Small alignment marks can be difficult to find in the electron microscope. Large alignment marks are helpful for finding the small alignment marks. Identifying arrays of squares help identify the different alignment marks.

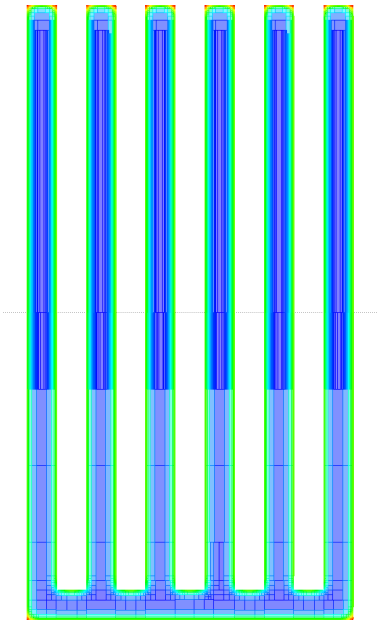

Figure A.1. An example of computed proximity effect correction to electron dose for an Au electrode design. The lowest correction factor is 0.686 (blue) and the highest is 1.359 (red).

The copper and gold layers must be separated so that charge cannot flow from one to the other, but close enough together that when an electron is collected from an exciton by the inherently positive copper electrode, the gold electrode will collect the hole from the exciton. The smaller the gap, presumably the more sensitive the detector. The longer the boundary between copper and gold within the region where excitons are present, the greater the sensitivity of the device. On the other hand, high capacitance might negatively impact the time resolution of the detector.

Proximity effect correction was used in the electron beam lithography [158]. I used $\beta = 3.33$ μm, $\eta = 0.75$, and a beam size of 10 nm.

A.3. Recommended Lithography Recipe

(1) Resist Preparation

(a) Sonicate the sample for three minutes in acetone.

(b) Rinse in isopropanol.

(c) Set a hot plate to 150 C.

(d) Place the sample on to a spinner with a small chuck.

(e) Activate the spinner vacuum.

(f) Test the spinner cycle.

(g) Use a pipette to pick up undiluted Zeon Chemicals L.P. ZEP 520A resist. ZEP is

- Positive resist
- Molecular Weight 57000
- 11% methyl styrene and chloromethyl acrylate copolymer
- 89% anisole
- Sensitive
- Etch resistant
- High resolution

(h) Discard one drop of ZEP.

(i) Place two drops on the sample.

(j) Spin at 4000 RPM for 30 seconds to produce an expected 300 nm thickness.

(k) Bake on the hot plate at 150 C for 3 minutes.

(l) Cool the sample quickly.

(2) Electron Beam Writing

Figure A.2. Raith 150 Electron Beam Lithography System

- Raith 150 electron beam lithography system.
- 30 kV beam acceleration.
- 30 μm aperture.
- 10 mm working distance.
- Secondary electron detector.
- Three point alignment with focus correction.
- 100 μm write field.
- Dose of about 99 nC/cm^2 written in three parts of 33 nC/cm^2

- Each of the three writings offsets the write field by 10 μm in both axes to reduce stitching error.
- Step size of 0.1 μm in both axes.
- Current is typically 370 pA.
- Beam dwell is computed based on other parameters. It is typically 9 ms.
- The instrument's maximum beam speed is about 11 mm/s. These parameters operate near the limit on the Raith 150 blanking speed.

(3) Development

- Develop in Xylenes for 30 seconds.
- Rinse in isopropanol.
- Blow dry.

(4) Descum

- The March plasma etcher has power and pressure feedback.
- It is precleaned with oxygen plasma.
- Oxygen pressure 165 mTorr.
- Power 20 Watts.
- Duration 15 seconds.
- Oxygen plasma does not oxidize the sample.

(5) Deposition varies

(6) Liftoff

(a) Place sample in anisole at 70 C for 40 minutes.

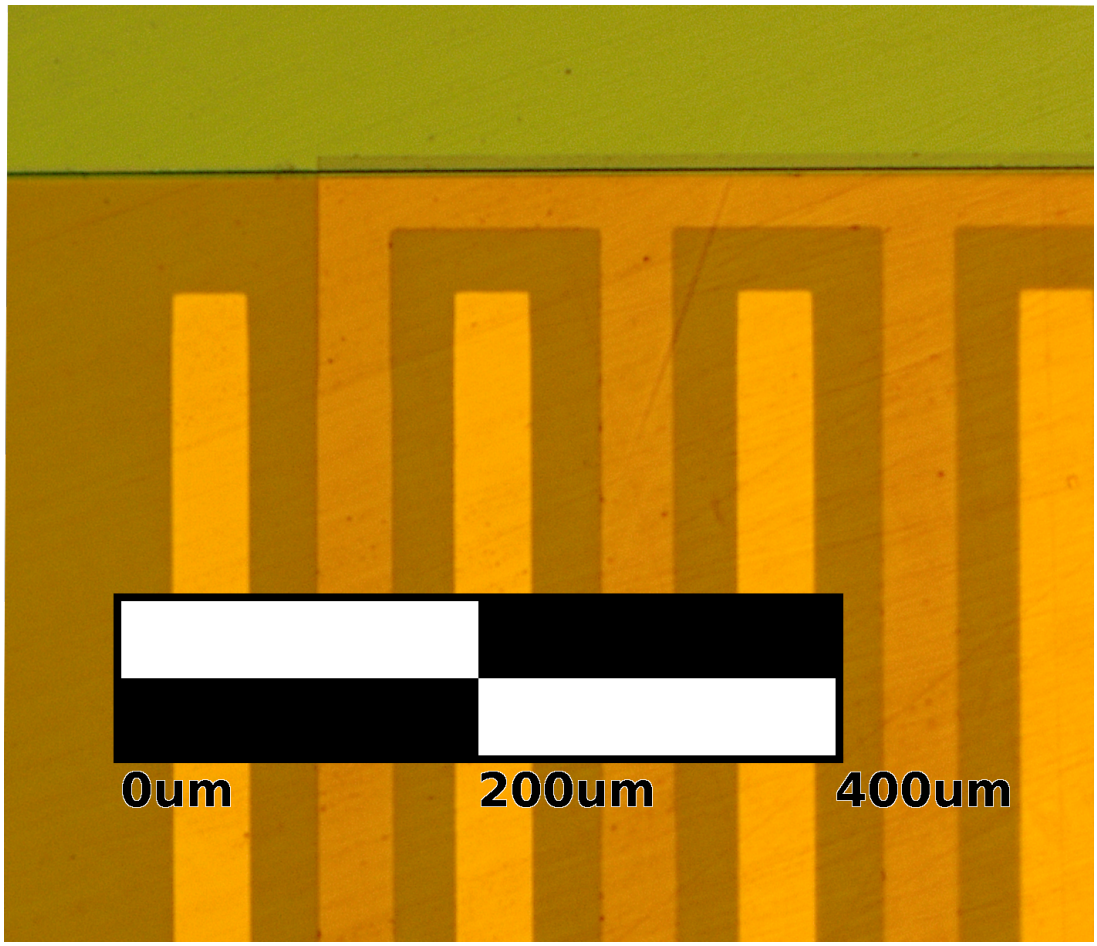

Figure A.3. This microscope image shows a device after the development step of the contact pad layer. The gold electrodes are yellow. The copper electrode is red. The background is resist. The green region at the top is the developed, but not deposited, contact pad.

(b) Rinse in a powerful stream of acetone. The style of squirt bottle with the tube coming out the top provides an adequate stream. The type of bottle with the tube coming out of the side does not work.

(c) Return the sample to the anisole and sonicate it for a few seconds.

(d) Rinse the sample with IPA.

Figure A.4. March Plasma Etcher used for oxygen plasma cleaning, which may improve deposition adhesion by removing residual resist from the developed area.

(e) Repeat liftoff steps until all resist and the deposited material on top of the resist is gone. Try not to allow the sample to dry during liftoff.

(f) Blow dry the sample.

A.4. Deposition

Deposition was typically performed using an AJA system with four distinct sputtering targets. This system is very fast because it has a load lock and it is not often necessary to change targets. Based on convenience, sometimes an Emitech sputtering system was used. It has three identical targets and has some constraints such as limited sputtering duration. No big difference was found between the two pieces of sputtering equipment.

Sputtering is omnidirectional. In some cases, a sputtered layer can adhere to the side of the resist near the developed area, preventing proper liftoff. With this lithography recipe, sputtering was successful. If it had not been successful, then evaporation could have been used throughout.

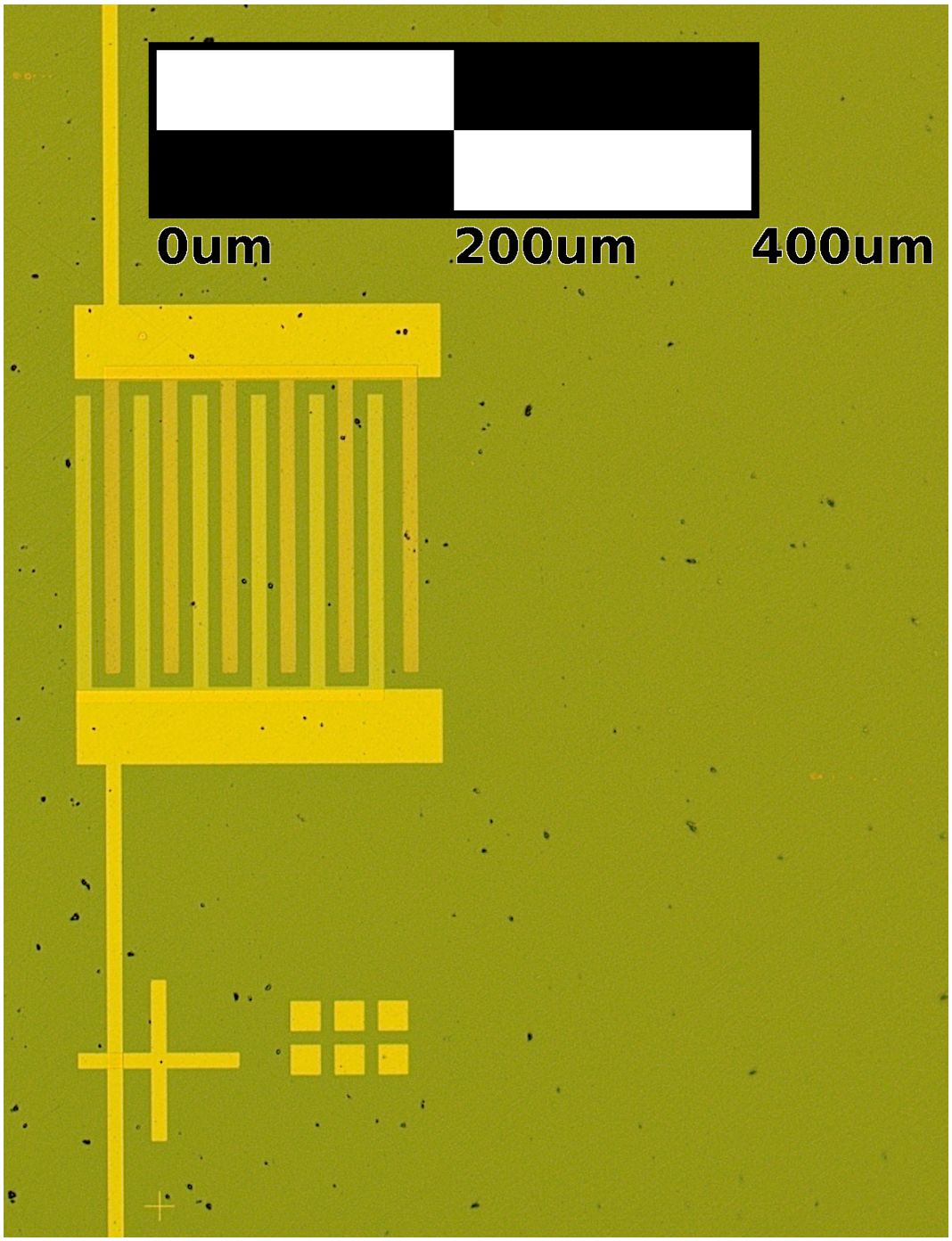

Figure A.5. Microscope image of a completed device. The gold electrode is the bottom one. Both small and large alignment marks are visible.

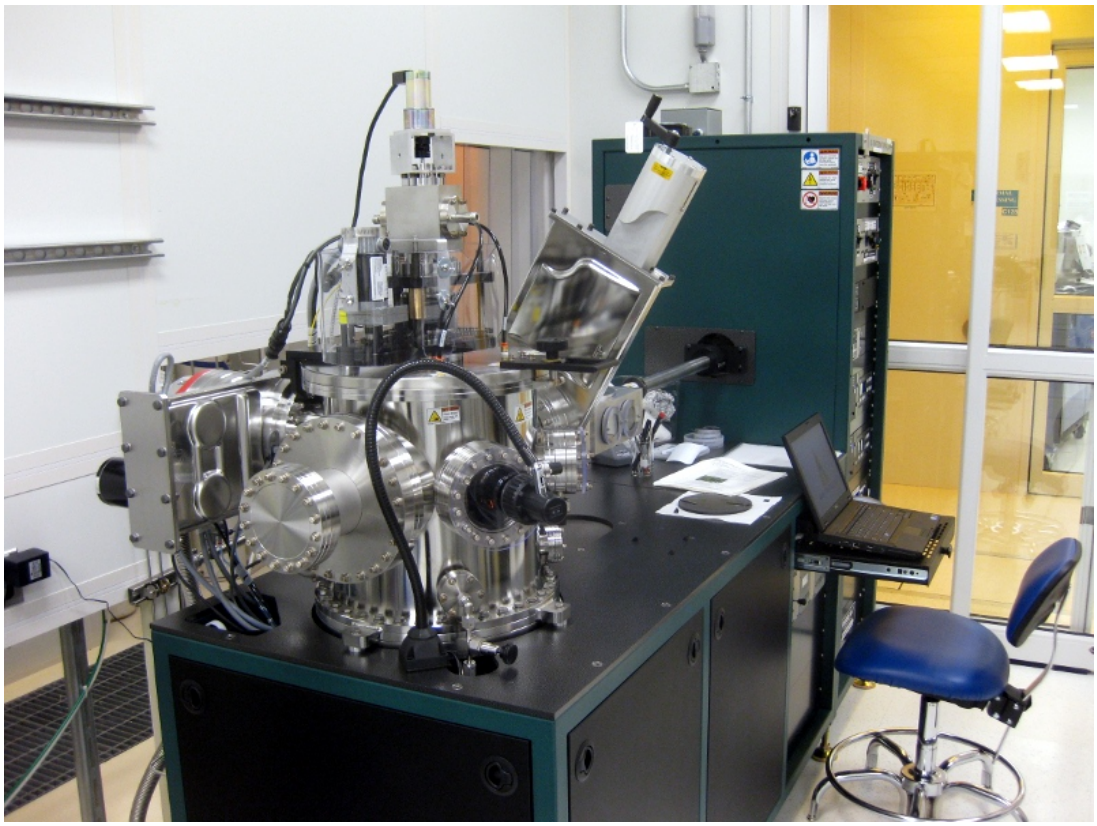

Figure A.6. AJA sputtering system.

A.4.1. Alignment Marks

Alignment mark deposition is the least particular deposition layer. The important thing is that the alignment marks be easily imaged by a scanning electron microscope. I typically used 10 nm chromium as an adhesion layer followed by 100 nm gold. Gold sputters fast and provides good contrast because it is dense.

A.4.2. Copper and Gold

Typically I sputtered 100 nm of copper or gold for the copper and gold electrode components. Thinner layers do make a partially transparent device, which could be useful since

it would allow for pump laser beams to shine through the device, but I used thicker layers to ensure adequate conductivity.

A.4.3. Contact Pads

Contact pad deposition is the final and most troublesome step. While in all cases, deposition adhesion seemed to be adequate for proper liftoff, contact pad adhesion was not adequate for reliable wire bonding, though bonds were occasionally made. A variety of contact pad deposition formulas were tested. Anecdotally, the best adhesion was obtained using a Lesker CMS Lab-18 electron beam evaporator to deposit 5 nm Ti and 100 nm Au. This deposition was performed by Dan Rosenmann. Ultimately, the conductive epoxy Circuitworks CW2400 was substituted for wire bonding. The epoxy was cured at 75 C for one hour. When epoxy is used, the contact pad composition does not appear to be important.

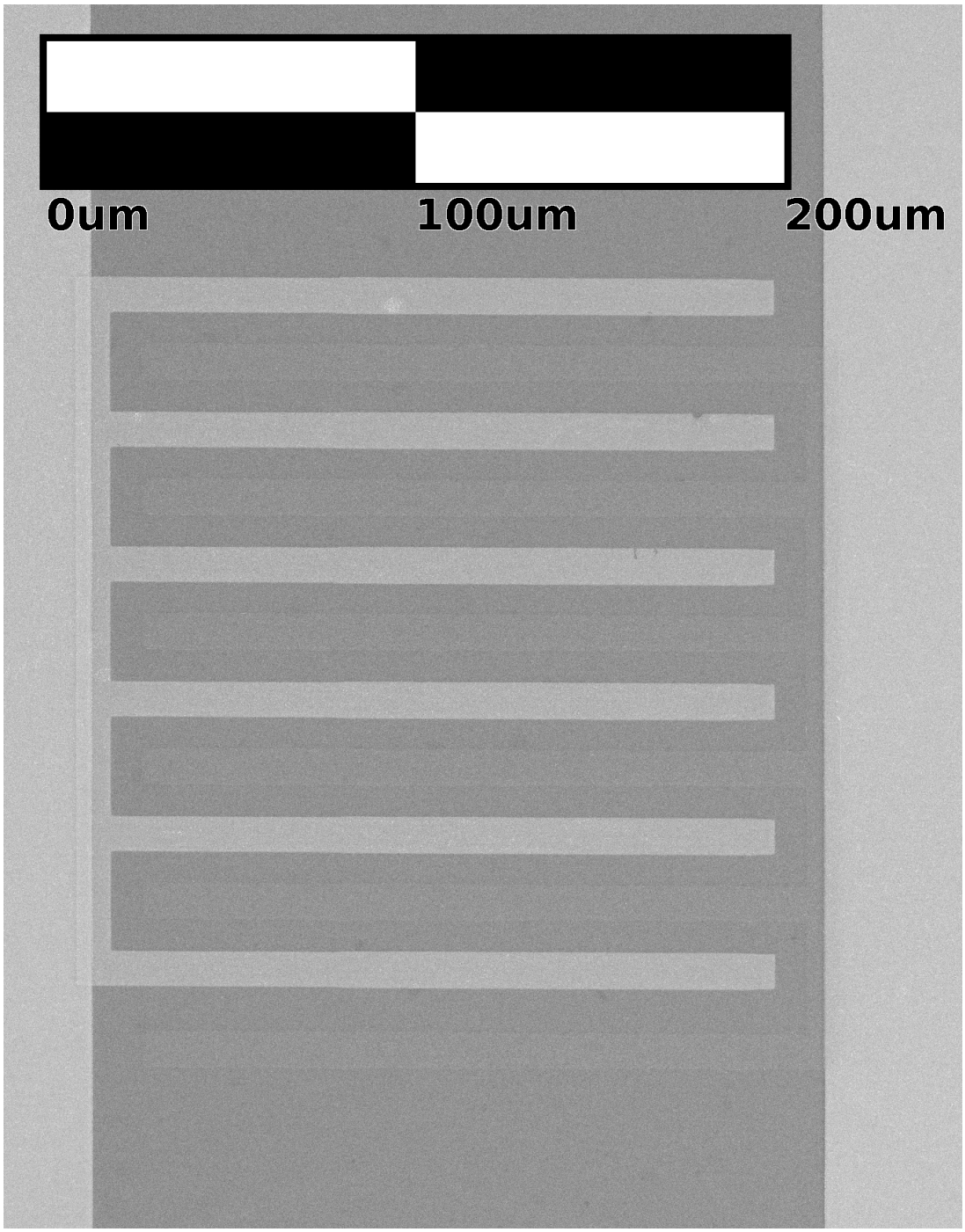

Figure A.7. An SEM image of an example device. The copper component has low contrast in the SEM because it is on a Cu_2O background.

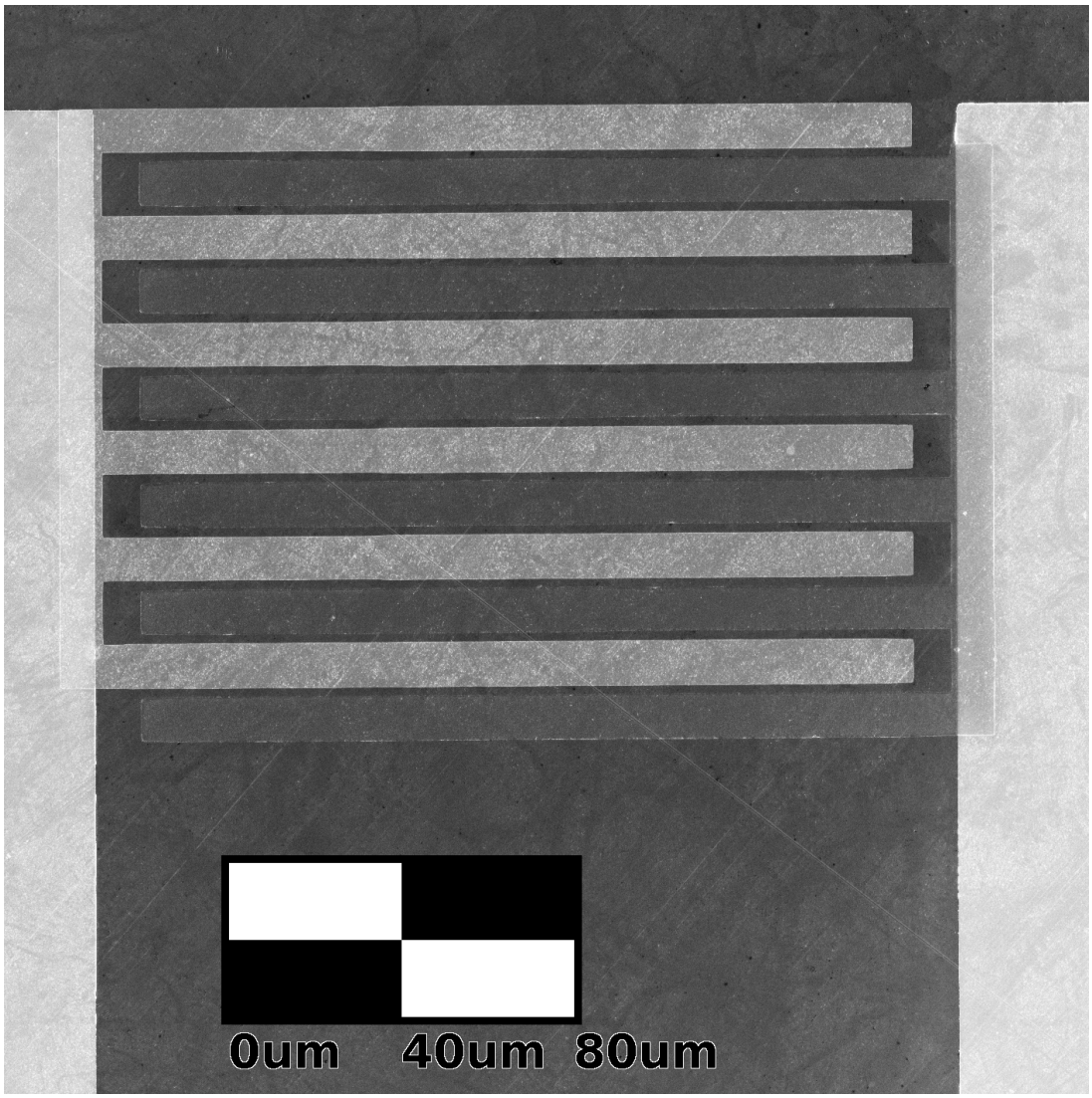

Figure A.8. A second SEM image of an example device. In this case the electrodes are closer together.

APPENDIX B

Photovoltaic Measurements

B.1. Background

B.1.1. Voltaics

At a copper-cuprous oxide boundary, electrons in the cuprous oxide are attracted to the copper and holes are repelled by a 0.75 eV Schottky barrier [159] owing to the ionic component of copper/oxygen bonds. Photocurrent spectra revealed that absorption through the *1s* orthoexciton polariton quadrupole resonance produced a voltage. Long distance diffusion was observed [160].

Laser pulses were used to excite cuprous oxide above the gap. Time resolved voltage showed two types of signal: broad diffusion or a narrow pulse of excitons. The narrow pulse occurred at higher pump intensities and lower temperatures. This was interpreted as evidence of superfluidity [161]. The phase boundaries were mapped out. Pump probe experiments were performed with 532 nm excitation showing a soliton gathering excitons from a diffusive probe [162] leaving the probe with a sech^2 shape [163]. Solitons were produced with phonon assisted absorption and $n = 2$ exciton state absorption [163].

Gain to the soliton was found when a background of continuous wave excitons was present. Soliton heights are up to 18 mV with a 50 Ω load [164].

Two photon photo-voltaic spectroscopy verified that an exciton mediated photovoltaic effect occurs even if excitons are pumped directly into the yellow *1s* orthoexciton state, but

that phonon-assisted two photon absorption is forbidden. The high-lying green exciton also has two photon absorption to the *1s* through *4d* states. The voltage was not time resolved [165].

B.1.2. Phonon Wind

The momentum flux of acoustic phonons is

$$\mathbf{W}(\mathbf{r},t) = \frac{1}{4\pi}\frac{\varepsilon_{PW}}{S}\int_V \frac{\mathbf{r}-\mathbf{r}'}{|\mathbf{r}-\mathbf{r}'|^3} g\left(\mathbf{r}', t - \frac{|\mathbf{r}-\mathbf{r}'|}{S}\right) d^3\mathbf{r}' \tag{B.1}$$

ε_{PW} is the energy associated with the poorly understood operator $Y^\dagger$, the energy released by Expression electron-hole binding, here presumed to form phonons. S is the speed of sound. g is the carrier generation rate. The corresponding motion of excitons with concentration n is

$$\frac{\partial n}{\partial t} + \nabla\cdot\mathbf{V}n = D\nabla^2 n - \frac{n}{\tau_c} \tag{B.2}$$

$$\sigma_{ph}\left(1-\frac{V}{S}\right)\mathbf{W} = \frac{m}{\tau_r}\mathbf{V} \tag{B.3}$$

Where $\mathbf{V}$ is the exciton drift velocity, D is the exciton self-diffusion constant, τ_c is the exciton lifetime, τ_r is the electron-hole recombination time, and σ_{ph} is the exciton-phonon scattering cross-section. For absorption coefficient λ, there is a solution

$$n(z,t) = \frac{g_s}{\tau_i}e^{D\lambda^2 t}\left[e^{-\lambda z_0}\operatorname{erfc}\left(\frac{2D\lambda t - z_0}{\sqrt{4Dt}}\right) + e^{\lambda z_0}\operatorname{erfc}\left(\frac{2D\lambda t + z_0}{\sqrt{4Dt}}\right)\right] \tag{B.4}$$

where g_s is λ times the number of photons per pump pulse and τ_i is the pulse duration [166]. This model seems to reasonably fit the observed solitons, but may or may not

explain gain from a continuous wave background [167–170]. It has been pointed out that an unspecified dispersion and nonlinearity can produce solitons in the absence of phonons or superfluidity [171].

B.2. Sample Connection

Several mounting techniques were used in measurements of the photovoltaic devices described in Chapter A. I machined a new mount for each sample because I did not wish to disturb the devices once they were successfully mounted. The mounts used had opaque shields with one or two openings because of concerns expressed in Reference [172] p. 44 about stray light disabling the detector "for an unknown reason." I was not able to determine if these shields were really necessary. In most cases, black ABS plastic was used because it is insulating, opaque, and easily machined. For temperature dependent measurements, a copper mount was used to ensure good thermal coupling between the sample and the silicon diode thermometer. With the copper mount, extra care was taken to insulate the signal lead from the grounded mount using electrical tape.

The sample was adhered to the mount or, for concave mounts that were difficult to reach into, a fragment of a glass coverslip for easy handling. The adhesive was VGE-7031 varnish, which was cured overnight at 50 °C in an oven. Wedge shaped copper strips were adhered to the device contact electrodes with ITW Chemtronics CW2400 two part conductive epoxy. When mixing the epoxy, I found I got better results if I prepared substantially more epoxy than I needed because it made the epoxy easier to mix. The epoxy was again cured overnight at 50 °C. Conductive epoxy has the disadvantage that

incorrect connections cannot be removed, however I found it was much more reliable than wire bonding.

I soldered leads onto the copper strips and applied additional varnish as necessary to ensure all parts would stay mounted. The mount was bolted to the central probe rod of the cryostat, which also served as a ground. An insulated wire, typically connected to the copper electrode on the device, was twisted up the rod. I soldered that signal wire to the core of a BNC pass through. A BNC cable connected the system to a BNC T junction, which was attached to the oscilloscope and a 50 Ω shielded resistor (in parallel with the device). The entire cryostat, cryostat mount, optical table, and BNC cable shield formed a common ground, which was connected to the wall circuit ground. The cryostat mount has four conductive posts which form potential, unavoidable ground loops. Correctly assembled devices had room temperature resistances of order 10 kΩ, depending on the details of the contact geometry and crystal synthesis.

All measurements were performed in the cryostat. Room temperature experiments were performed in vacuum to prevent oxidation. It was not determined if this was necessary. Low temperature experiments were performed in liquid or gaseous helium.

The oscilloscope used was a Tektronix TDS340. Its specifications are similar to those of the oscilloscope used in reports of paraexciton solitons. It has a 100 MHz bandwidth and a 1 MΩ input impedance. The primary instrument limitation is that it can only average 256 laser shots at a time. Typically this was sufficient, but the program described in Chapter C allows for further averaging.

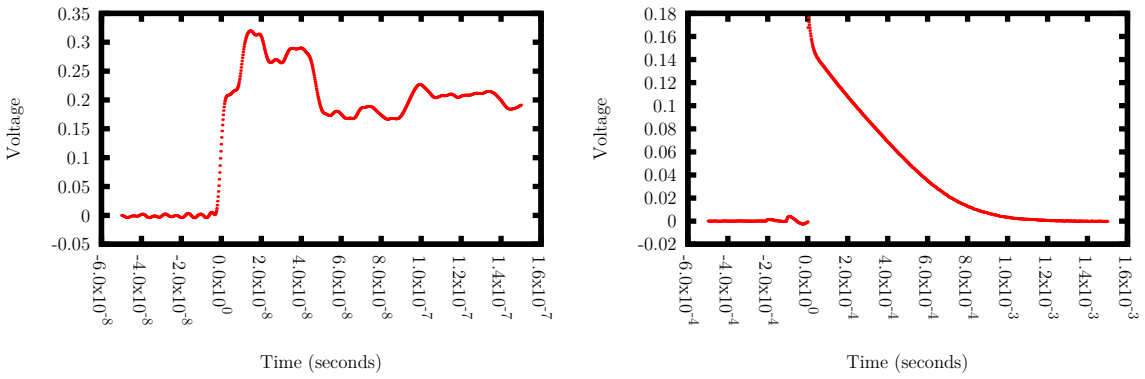

Figure B.1. Waveform of the trigger diode on two different time scales.

B.3. Triggering

The laser was used to optically trigger the oscilloscope. Similar to Chapter 7, the laser third harmonic pumped the OPA which illuminates the sample. A small portion of the 355 nm third harmonic light leaked through a mirror between the laser and the OPA. I placed a Thorlabs DET100A silicon diode so that it would absorb the leaked light. It was connected to the oscilloscope as a trigger. No power supply was used with the diode. The diode has a 43 ns rise time according to the manufacturer, but the actual rise time appears to be shorter (Figure B.1). It is probably less than the oscilloscope resolution. The oscilloscope can take only 1000 samples from each waveform. To use them most efficiently, I typically configured the oscilloscope to record the minimum number of pre-trigger samples, which is 250.

B.4. Noise

The sample was adjacent to a picosecond pulsed Nd:YAG laser, which contains components that use high voltage pulses, such as Pockels cells. The laser electronics have some inductive coupling to the sample circuit. This coupling is apparently much less

severe than the problems described in Reference [172] p. 47. Four simple steps greatly reduced both the noise and the background from inductive coupling.

First, cables were disconnected from the TRAIN, SYNC1, SYNC2, and TRIG connectors on the side of the laser head. These unnecessary components served as antennas which transmitted unwanted background signals. The triggering system described in Reference [172] relies on similar connections, which may explain why it suffered from more noise. Second, the optical table was correctly grounded. Third, the signal was averaged across laser shots. Single shot measurement was possible, but typically averaging of order 256 shots was desirable (Figure B.2). Fourth, all measurements were repeated with the laser beam blocked by a robotic shutter in front of the cryostat. The signal recorded with the shutter in place was taken to be a background (Figure B.3) and subtracted from the signal. The necessary computer program is in Chapter C. The resulting measurements are therefore solely owing to interaction of the laser light with the sample, and not inductive coupling.

B.5. Comparison with Photomultiplier

Previously, both optical and electronic means of investigating paraexcitons have been employed. Only electronic evidence of paraexciton solitons has been reported. Optical methods typically rely on weak phonon linked luminescence mechanisms or strain. I made some simple measurements with a photomultiplier tube for comparison with the electronic detector. While the electronic detector temporal resolution is limited by the oscilloscope used, the photomultiplier time resolution is about 500 ns, even when a low load resistance of 17 Ω was used (Figure B.4). Better photomultiplier measurements can be performed

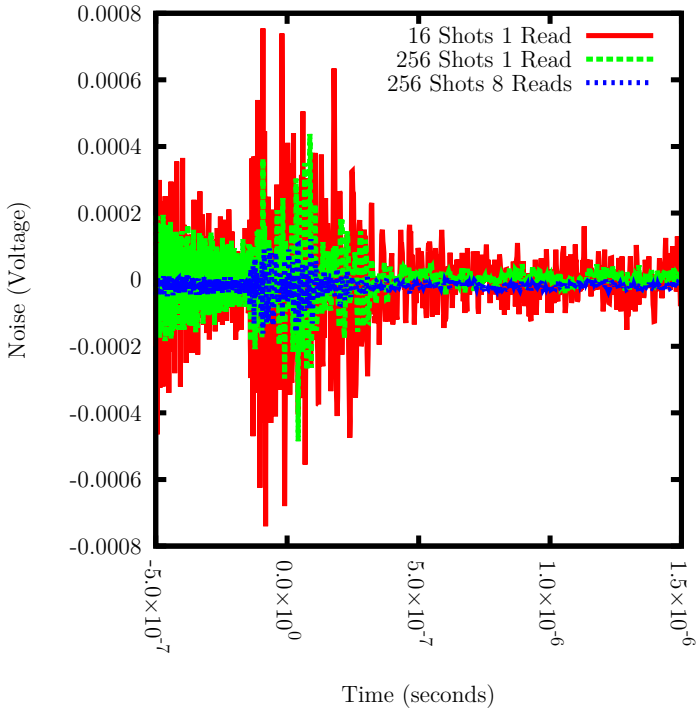

Figure B.2. Measurements from a sample not exposed to light demonstrate the benefits of averaging the signal. When the number of laser shots increase by a factor of 8, the amount of noise remaining after averaging decreases by about a factor of $\sqrt{8}$, as expected.

by replicating, for example, the methods of Reference [11], which did not observe solitons. Time resolved luminescence measurements on a much shorter time scale are reported in Chapter 4.

B.6. Spectra

A device at 1.4±0.5 K was illuminated by passing the OPA beam through the sample. The prompt photocurrent across 50 Ω resistance was recorded (Example in Figure B.5) as a function of the OPA beam center energy (Figure B.6). The results are consistent with Reference [165], accounting for differences in geometry. When light is transmitted

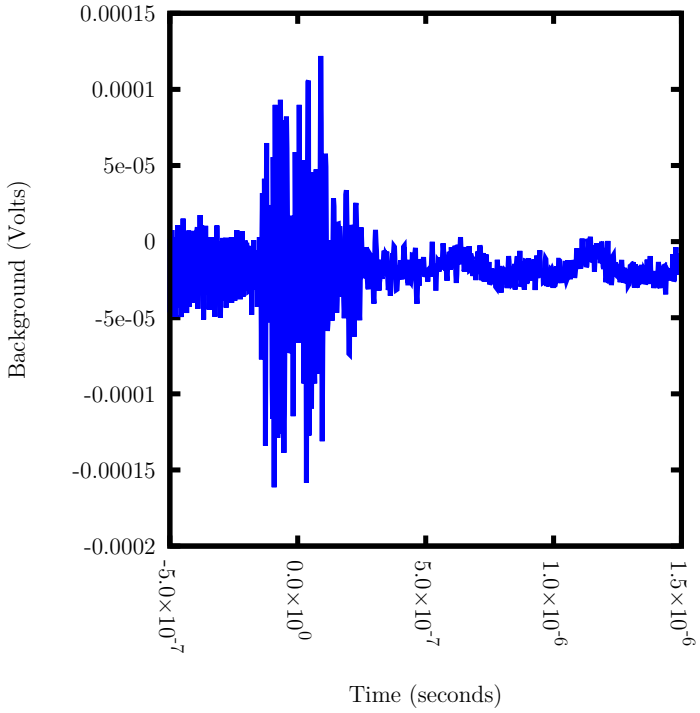

Figure B.3. An example of background caused by inductive coupling. This background is readily removed by subtraction, as in Figure B.2.

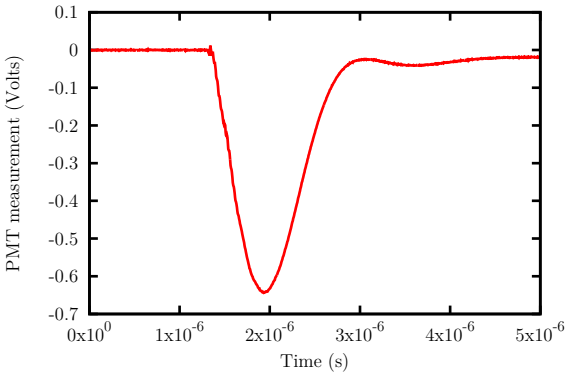

Figure B.4. Time resolved luminescence at 220 K collected through a 610 nm band pass filter.

through the cuprous oxide sample to the detector, a strong signal is detected. At higher photon energies, the light is absorbed and no signal reaches the detector. The energy of

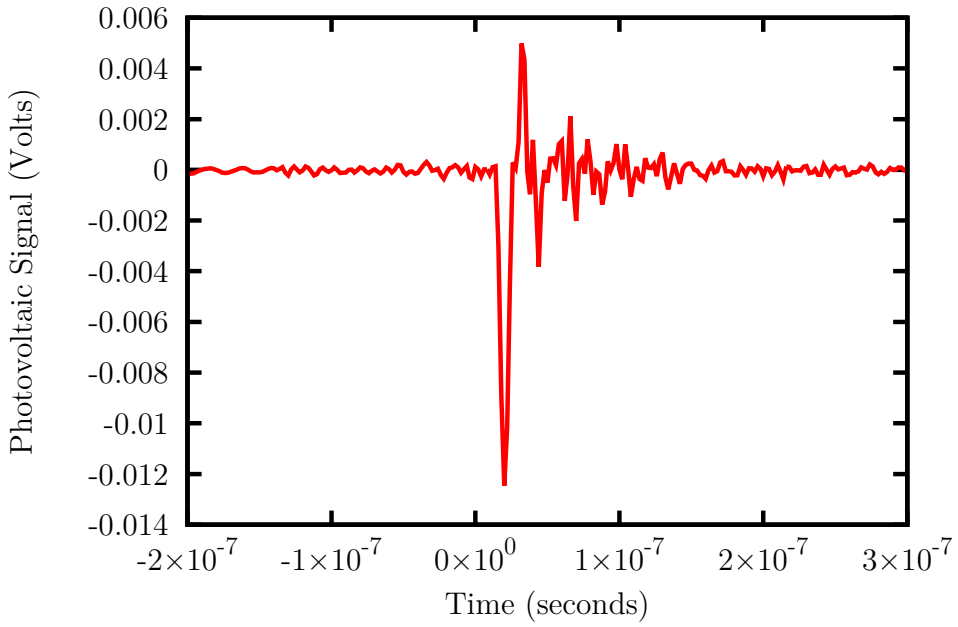

Figure B.5. Time resolved photocurrent for a wavelength of 622 nm (1.99 eV).

the OPA output as a function of the energy of the photons in the OPA beam is displayed in Figure B.7. Variations in the OPA linewidth are shown in Figure B.8. The linewidth sets the resolution of Figure B.6.

The primary absorption feature starts at 2.051±0.001 eV. This is consistent with production of a *1s* orthoexciton and a 18.7 meV ${}^3\Gamma_{15}^-$ phonon. The absorption coefficient increases like the square root of the phonon energy [25]. Applying the Beer-Lambert law, the photovoltaic signal as a function of energy E is

$$V(E) \propto -H(E-2.051)e^{-\frac{\sqrt{E-2.051}}{0.15}} \tag{B.5}$$

This is the green curve in Figure B.6. H is the Heaviside step function.

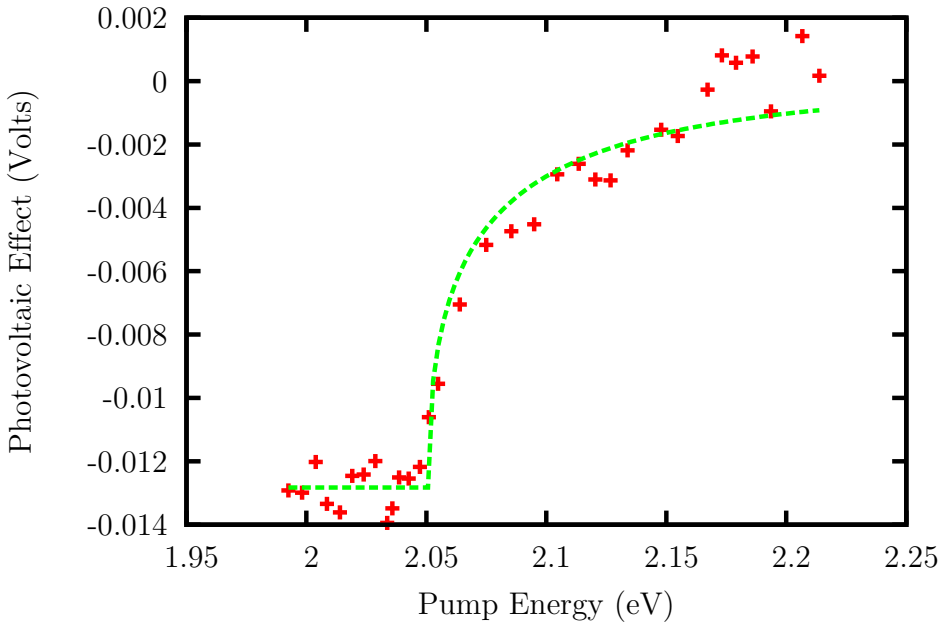

Figure B.6. Device photovoltaic spectrum in the back cell geometry.

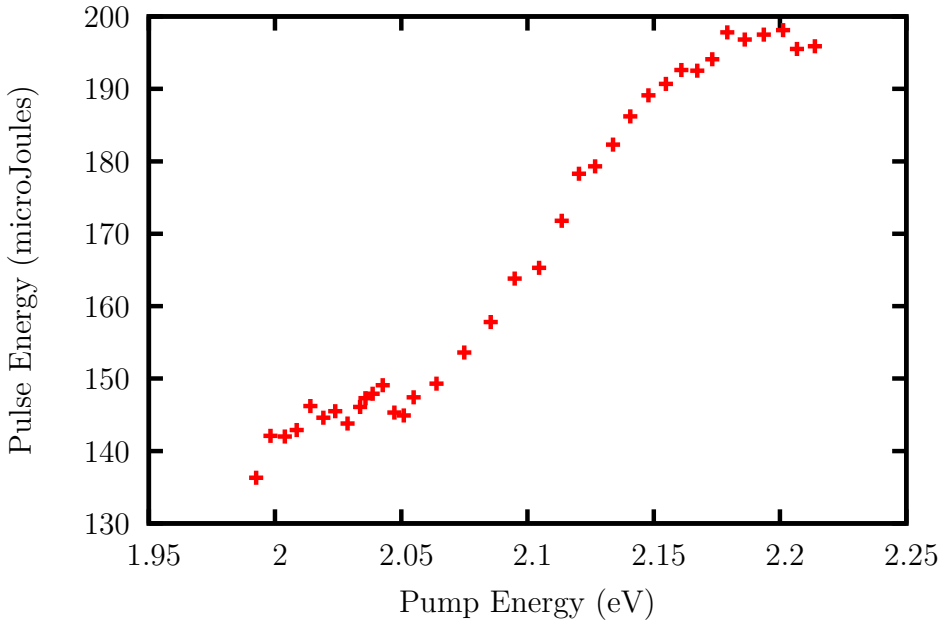

Figure B.7. Energy of the OPA output pulses as a function of the OPA center photon energy.

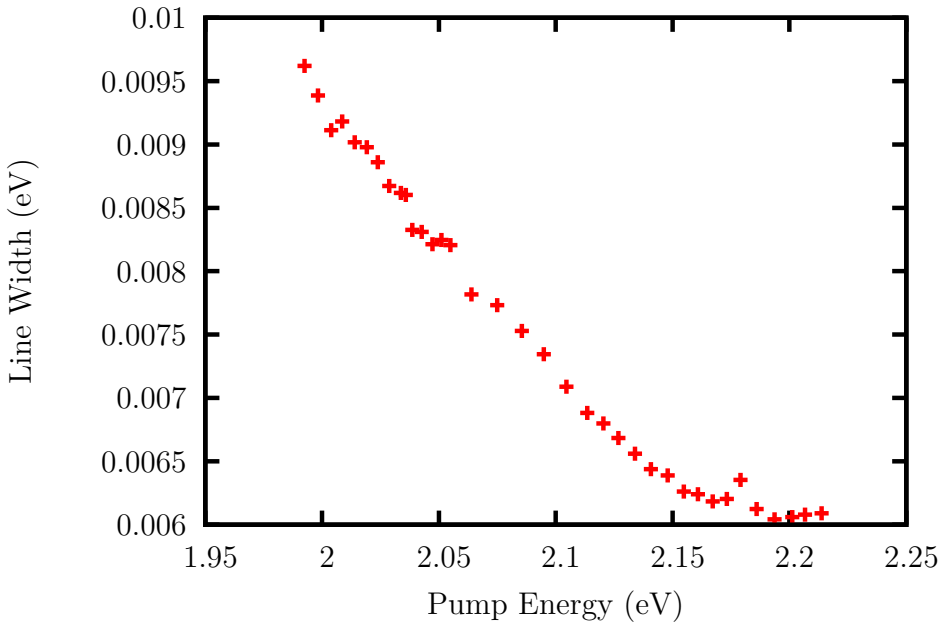

Figure B.8. OPA spectral linewidth as a function of the OPA center photon energy.

B.7. IV curves

The current-voltage characteristic curve of the copper/cuprous oxide/gold device for room temperature is plotted in Figure B.9. The curve is non-Ohmic and also not rectifying. The purpose of the red line is to emphasize the non-Ohmic shape. The characteristic curve is qualitatively similar to back-to-back Schottky diodes [173]. At 1.4±0.5 Kelvin, the resistance of the device is much greater (Figure B.10).

B.8. Power Dependence

The response of the photovoltaic device was nonlinear. Curves similar to Figure B.5 were recorded at 185.3± 0.5 K with the OPA set to a center energy of 1.96 eV. Figure B.11 shows the peak voltage across a 50 Ω load for a variety of laser pulse energies. The

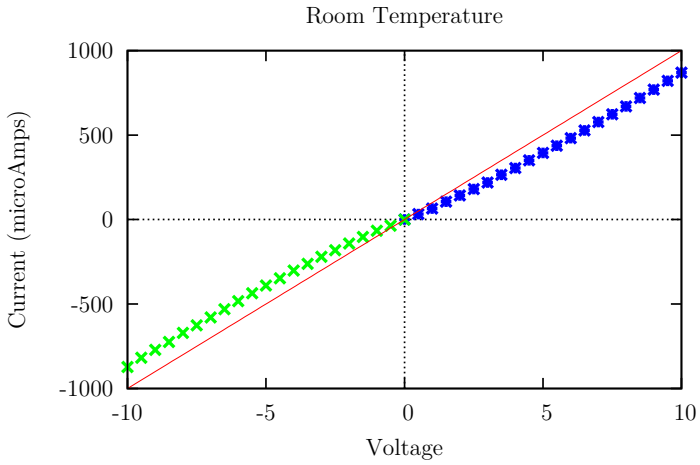

Figure B.9. Current/Voltage curve at room temperature.

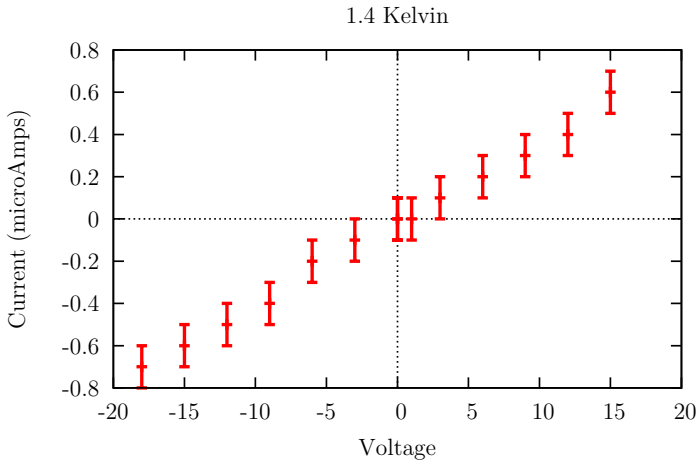

Figure B.10. Current/Voltage curve at 1.4 Kelvin.

less-than-linear pattern of the data suggests the detector may become saturated at higher currents.

Exciton solitons only form at sufficiently high exciton densities. Since no exciton solitons were observed, it is important to consider whether sufficient laser power was used to excite the crystal. I used the second harmonic generation directly produced by the

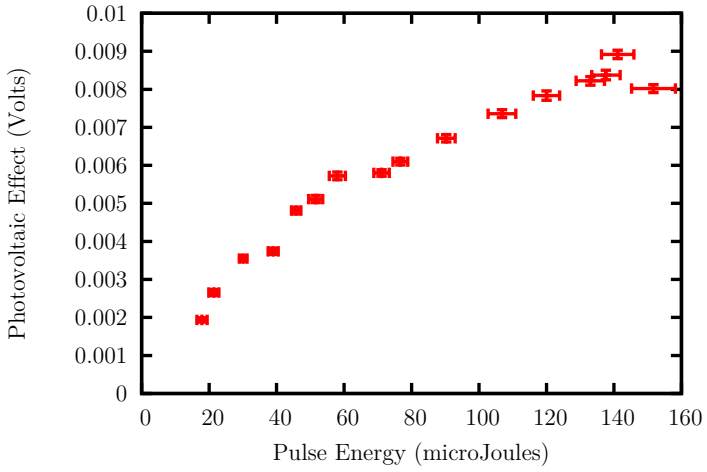

Figure B.11. Photovoltaic signal versus laser pulse energy.

laser to eliminate this concern. Typically the 2.033 eV second harmonic light produces no signal in the back cell geometry. With the sample at 1.4 Kelvin, I increased the laser power until a signal appeared in the back cell geometry; only a prompt signal, and not a soliton signal, was observed. The cause of this photovoltaic signal was optically induced cleaving of the crystal. A [111] faceted, truncated pyramid was removed from the [100] crystal wafer by high power laser pulses (Figure B.12). This allowed the light from the laser to pass through the crystal to reach the photovoltaic device. The laser spot was evidently not centered on the device when the cleaving occurred. These results show that further increases in laser power are not beneficial since they break the sample. Cleaving of the crystal into clean faces is surprising since normally cuprous oxide has poor cleavage. Laser cleavage may provide a more precise method of orienting cuprous oxide wafers than Laue diffraction.

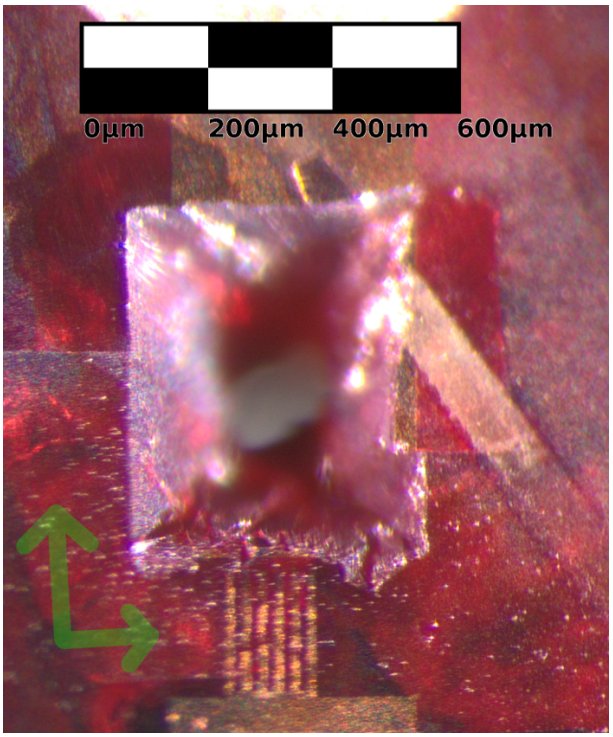

Figure B.12. Cuprous oxide wafer with photovoltaic device, cleaved by intense laser light. The view is towards the laser beam. The truncated pyramid cleaved from the sample is deeper than the microscope depth of field. The green arrows indicate equivalent [110] crystal lattice axes. The cleavage planes are along [111].

B.9. Photoconductivity

The sample was illuminated with a continuous wave, intracavity doubled 2.33 eV Nd:YVO_4 laser. Three Watts of laser beam power were chopped by a Stanford Research Systems SR540 optical chopper set to 20 Hz. The sample was cooled to 230 K so that the photoconductivity of the sample would be sufficiently large. At lower temperatures, the photoconductivity changed too slowly to be measured with this optical chopper. The sample was connected in series to an 85 V power supply and a 36.8 kOhm resistor. The resistivity of the sample in darkness was 335 kΩ, so the circuit forms an poor quality

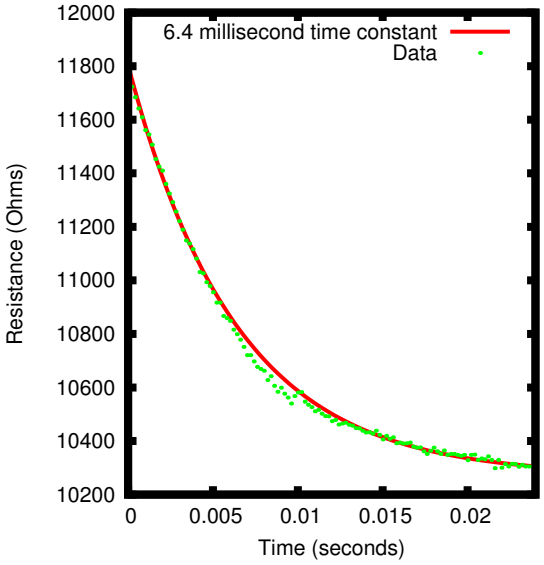

Figure B.13. Time-resolved photoconductivity of cuprous oxide.

constant current source. The sample was illuminated from the side opposite the electrodes. The voltage across the device after the laser pulse was turned on by the chopper was recorded with the oscilloscope and the implied resistance of the sample was calculated (Figure B.13). The oscilloscope was triggered by the optical chopper controller. The resistance of the sample decayed exponentially in time with a time constant of 6.35±0.08 ms.

B.10. Continuous Wave Attenuation

A final tool to use to try and find exciton solitons is amplification of solitons by a continuous wave light source [164]. I found that the 2.33 eV continuous wave laser actually reduced prompt photovoltaic signals from 1.96 eV OPA light at 1.4 Kelvin owing to increased photoconductivity of the sample. Figure B.14 shows a reduction in the amplitude of the observed photovoltaic pulses from 0 to 2 Watts of continuous wave

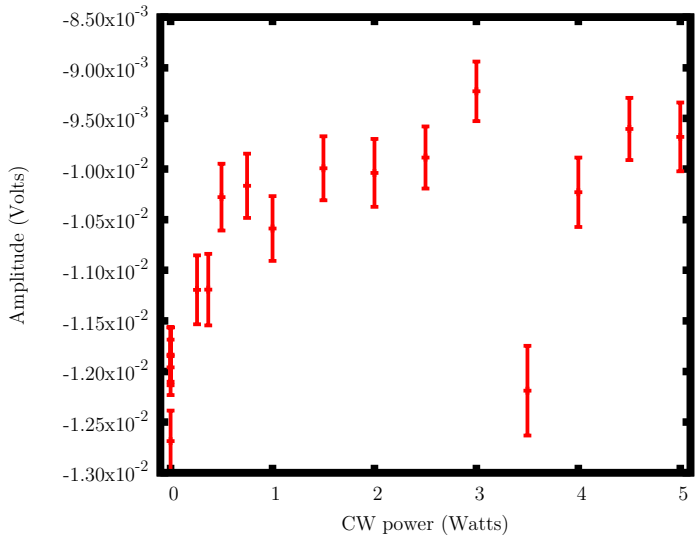

Figure B.14. Addition of a continuous wave, above the gap pump to a below the gap photovoltaic signal decreases the signal amplitude because of an increase in photoconductivity which penetrates the bulk.

power, with little change above 2 Watts. In this experiment the photovoltaic device is illuminated through the crystal. Since the continuous wave light is absorbed on the crystal surface but the pulsed light passes through the sample to the detector, this data shows transport across the sample is occurring. Paraexcitons are the only known means of transport across such large distances.

APPENDIX C

Photovoltaic DAQ Program

The photovoltaic data acquisition system relied on the components listed below. Their documentation was essential to assembling the system.

- Tektronix TDS340 oscilloscope
- Agilent 82357b GPIB/USB interface
- Phidgets servo controller
- Firgelli L12 100 mm linear actuator
- Windows Vista 64 bit
- Visual Studio Express 2012 (compile for x64)
- Gnuplot
- Agilent Connection Expert

```
1  #include <stdio.h>              // for printf()
2  #include "sicl.h"               // Standard Instrument Control Library routines,
       Agilent
3  #include <windows.h>
4  #include <tchar.h>
5  #include <stdlib.h>
6  #include <assert.h>
7  #include "stdafx.h"
8  #include <phidget21.h> //motor control library, Phidgets
9
10 #define DEVICE_ADDRESS "gpib0,1"    // Modify this line to match your setup
```

```
11
12 #define READS 1//how much averaging to do on the computer
13 //more than 249 causes a stack overflow on my system
14
15 #define AVERAGENUM "ACQUIRE:NUMAVG 256"
16 //how much averaging to do on the oscilloscope, 256 maximum, must be a power of 2
17
18 //motor configuration
19 #define OPENPOS 85.00
20 #define CLOSEDPOS 115.00
21 //time it takes motor to move
22 #define DWELLTIME 3300
23
24 //responds to attachment of phidget
25 int CCONV AttachHandler(CPhidgetHandle ADVSERVO, void *userptr)
26 {
27         int serialNo;
28         const char *name;
29
30         CPhidget_getDeviceName (ADVSERVO, &name);
31         CPhidget_getSerialNumber(ADVSERVO, &serialNo);
32         printf("%s %10d attached!\n", name, serialNo);
33
34         return 0;
35 }
36
37 //responds to disconnection of phidget
38 int CCONV DetachHandler(CPhidgetHandle ADVSERVO, void *userptr)
39 {
40         int serialNo;
```

```
41          const char *name;
42
43          CPhidget_getDeviceName (ADVSERVO, &name);
44          CPhidget_getSerialNumber(ADVSERVO, &serialNo);
45          printf("%s %10d detached!\a\n", name, serialNo);
46          getchar();
47
48          return 0;
49  }
50
51  //responds to error
52  int CCONV ErrorHandler(CPhidgetHandle ADVSERVO, void *userptr, int ErrorCode, const
        char *Description)
53  {
54          printf("Error handled. %d - %s\n", ErrorCode, Description);
55          getchar();
56          return 0;
57  }
58
59  //start of program
60  int main(void)
61  {
62          INST id;                        // device session id
63          char buf[256] = { 0 };          // read buffer for idn string
64          char buf2[256] = { 0 };
65          char buf3[256] = { 0 };
66          char buf4[256] = { 0 };
67
68          char curvebuf[10000] = { 0 }; //big buffer for data from oscilloscope
69          char busybuf[256] = { 0 };
```

```
70          char one[1] = {0};
71          char voltage[1024] = {0}; //voltage scale
72          char time[1024] = {0}; //time scale
73          int i=0;
74          int j=0;
75          int k=0;
76          long int number=0; //for strtol
77          char * charptr; //for strtol
78          long int array[READS][1000];//signal data
79          long int barray[READS][1000];//background data
80          double average[1000] = {0};//signal average
81          double baverage[1000] = {0};//background average
82          errno_t error;
83
84          //command line access variables
85          STARTUPINFO si;
86          PROCESS_INFORMATION pi;
87
88          //file management
89          FILE * data;
90          FILE * gnuplot;
91
92          //phidget declarations
93          int result;
94          const char *err;
95          double maxVel, maxAccel;
96
97          //Declare an advanced servo handle
98          CPhidgetAdvancedServoHandle servo = 0;
99
```

```
100         //create the advanced servo object
101         CPhidgetAdvancedServo_create(&servo);
102
103         //Set the handlers to be run when the device is plugged in or opened from
                software, unplugged or closed from software, or generates an error.
104         CPhidget_set_OnAttach_Handler((CPhidgetHandle)servo, AttachHandler, NULL);
105         CPhidget_set_OnDetach_Handler((CPhidgetHandle)servo, DetachHandler, NULL);
106         CPhidget_set_OnError_Handler((CPhidgetHandle)servo, ErrorHandler, NULL);
107
108         //open the device for connections
109         CPhidget_open((CPhidgetHandle)servo, -1);
110
111         //get the program to wait for an advanced servo device to be attached
112         printf("Waiting for Phidget Advanced Servo to be attached....\n");
113         if((result = CPhidget_waitForAttachment((CPhidgetHandle)servo, 10000)))
114         {
115                 CPhidget_getErrorDescription(result, &err);
116                 printf("Problem waiting for attachment: %s\n", err);
117                 getchar();
118                 return 0;
119         }
120
121         //read event data
122         printf("Reading.....\n");
123
124         //This example assumes servo motor is attached to index 0
125
126         //Set up some initial acceleration and velocity values
127         CPhidgetAdvancedServo_getAccelerationMax(servo, 0, &maxAccel);
128         CPhidgetAdvancedServo_setAcceleration(servo, 0, maxAccel/200);
```

```
129         CPhidgetAdvancedServo_getVelocityMax(servo, 0, &maxVel);
130         CPhidgetAdvancedServo_setVelocityLimit(servo, 0, maxVel/100);
131
132         //power up motor
133         CPhidgetAdvancedServo_setEngaged(servo, 0, 1);
134
135         // Access oscilloscope
136         //
137         // Install a default SICL error handler that logs an error message and
                exits.  On Windows NT use the Windows NT Event Viewer.
138         ionerror(I_ERROR_EXIT);
139
140         // Open a device session using the DEVICE_ADDRESS
141
142         id = iopen(DEVICE_ADDRESS);
143
144         // Set the I/O timeout value for this session to 1 second
145         itimeout(id, 1000);
146
147         // Write the *IDN? string and send an EOI indicator, then read
148         // the response into buf.
149
150         ipromptf(id, "*IDN?\n", "%t", buf);
151
152         printf("%s\n", buf);
153
154         ipromptf(id,"ACQUIRE:STATE_OFF",buf4);//stop acquisition
155         ipromptf(id,AVERAGENUM, buf2);//set number of traces to average
156         ipromptf(id,"ACQUIRE:MODE_AVERAGE",buf2);//set averaging mode
```

```
157         ipromptf(id,"DATA:WIDTH 2",buf2);//read 2 bytes of data, only works when
                averaging
158         ipromptf(id,"ACQUIRE:STOPAFTER SEQUENCE",buf3);
159         //oscilloscope stops after data is collected
160
161         for(k=0;k<READS;k++){
162                 //move servo
163                 CPhidgetAdvancedServo_setPosition(servo, 0, OPENPOS);
164
165                 Sleep(DWELLTIME);
166
167                 printf("Collecting signal.\a");
168                 ipromptf(id,"ACQUIRE:STATE ON",buf4);//start acquisition
169
170                 Sleep(10);
171                 ipromptf(id,"BUSY?","%t",busybuf);
172                 one[0]=busybuf[0];//assumes oscilloscope is busy, measures the busy
                        message
173
174                 //while oscilloscope is busy, sleep
175                 i=0;
176                 while(one[0]==busybuf[0]){
177                         i++;
178                         if(1==i%10){
179                                 printf("\nBusy for %i seconds with message ",i);
180                                 printf("%s",busybuf);
181                         } else {
182                                 printf(".");
183                         }
184                         Sleep(1000);
```

```
185                     ipromptf(id,"BUSY?","%t",busybuf);
186
187             }
188             printf("\nDone after %i seconds with message ",i);
189             printf("%s",busybuf);
190
191             Sleep(10);
192
193             ipromptf(id, "CURV?\n", "%t", curvebuf);//read curve from
                    oscilloscope
194             //printf(curvebuf);
195
196             j=0;
197             for(i=0;(i<sizeof(curvebuf));i++){//gnuplot formatting
198
199                     //handle first number
200                     if((i==0)){
201                             array[k][j]=strtol(&curvebuf[i],&charptr,0);
202
203                             j++;
204                     }
205
206                     //handle remaining numbers
207                     if(curvebuf[i]==*","){
208                             assert(i!=0);
209                             curvebuf[i]='\n';
210                             array[k][j]=strtol(&curvebuf[i],&charptr,0);
211                             j++;
212                     }
213                     //else we're done
```

```
214                 }
215
216                 //move servo
217                 CPhidgetAdvancedServo_setPosition (servo, 0, CLOSEDPOS);
218
219                 Sleep(DWELLTIME);
220
221                 printf("Collecting background.\a");
222                 ipromptf(id,"ACQUIRE:STATE ON",buf4);//start acquisition
223
224                 Sleep(10);
225                 ipromptf(id,"BUSY?","%t",busybuf);
226                 one[0]=busybuf[0];//assumes I'm busy, measures the busy message
227
228                 i=0;
229                 while(one[0]==busybuf[0]){
230                         i++;
231                         if(1==i%10){
232                                 printf("\nBusy for %i seconds with message ",i);
233                                 printf("%s",busybuf);
234                         } else {
235                                 printf(".");
236                         }
237                         Sleep(1000);
238                         ipromptf(id,"BUSY?","%t",busybuf);
239
240                 }
241                 printf("\nDone after %i seconds with message ",i);
242                 printf("%s",busybuf);
243
```

```
244                 Sleep(10);
245
246                 ipromptf(id, "CURV?\n", "%t", curvebuf);//read curve from
                        oscilloscope
247
248                 j=0;
249                 for(i=0;(i<sizeof(curvebuf));i++){//gnuplot formatting
250                         //handle first number
251                         if((i==0)){
252                                 barray[k][j]=strtol(&curvebuf[i],&charptr,0);
253
254                                 j++;
255                         }
256
257                         //handle remaining numbers
258                         if(curvebuf[i]==*","){
259                                 assert(i!=0);
260                                 curvebuf[i]='\n';
261                                 barray[k][j]=strtol(&curvebuf[i],&charptr,0);
262                                 j++;
263                         }
264                 }
265
266                 printf("%i reads remaining.\n",READS-k-1);
267
268         }
269
270         //sum up measurements
271         for(k=0;k<READS;k++){
272                 for(i=0;i<1000;i++){
```

```
273
274                         average[i]+=(double)array[k][i];
275                         baverage[i]+=(double)barray[k][i];
276                 }
277         }
278
279         //divide to get average
280         for(i=0;i<1000;i++){
281                 average[i]=average[i]/((double)READS);
282                 baverage[i]=baverage[i]/((double)READS);
283
284         error=fopen_s(&data,"signal.csv","w");
285         if(error!=0){
286                 printf("Data file not opened.\n");
287         }
288
289         error=fopen_s(&gnuplot,"plot.gp","w");
290         if(error!=0){
291                 printf("Plot file not opened.\n");
292         }
293         ipromptf(id, "CH1:SCA?\n", "%t", voltage);//measure voltage per division
294         printf("%s", voltage);
295         ipromptf(id, "hor:mai?\n", "%t", time);//measure time per division
296         printf("%s", time);
297
298         //make gnuplot file
299         fprintf(gnuplot,"set terminal windows position 1,1\n");
300
301         //only valid for 2 byte mode
```

```
302         fprintf(gnuplot,"plot \"subtract.csv\" using ($0*%s/50):($1*%s/25/256) with
                lines\n", strtok(time,"\n"),strtok(voltage,"\n"));
303
304         //display graph briefly
305         fputs("pause 3",gnuplot);
306
307         //make data file
308         for(i=0;i<1000;i++){
309                 fprintf(data,"%f\n",average[i]);
310         }
311
312         //close files
313         if(fclose(data)!=0){
314                 printf("File not closed.");
315         }
316         if(fclose(gnuplot)!=0){
317                 printf("File not closed.");
318         }
319
320         //make background file
321         error=fopen_s(&data,"back.csv","w");
322         if(error!=0){
323                 printf("Data file not opened.\n");
324         }
325         for(i=0;i<1000;i++){
326                 fprintf(data,"%f\n",baverage[i]);
327         }
328         if(fclose(data)!=0){
329                 printf("File not closed.");
330         }
```

```
331
332         //make subtracted file
333         error=fopen_s(&data,"subtract.csv","w");
334         if(error!=0){
335                 printf("Data file not opened.\n");
336         }
337         for(i=0;i<1000;i++){
338                 fprintf(data,"%f\n",average[i]-baverage[i]);
339         }
340         if(fclose(data)!=0){
341                 printf("File not closed.");
342         }
343
344         //reset si
345         ZeroMemory( &si, sizeof(si) );
346         si.cb = sizeof(si);
347         ZeroMemory( &pi, sizeof(pi) );
348
349         //draw graph
350         if( !CreateProcess(NULL,     // No module name (use command line)
351                 "C:\\Program Files (x86)\\gnuplot\\bin\\gnuplot.exe -e \"load \\\"
                    plot.gp\\\"\"",// Command line
352                 NULL,           // Process handle not inheritable
353                 NULL,           // Thread handle not inheritable
354                 FALSE,          // Set handle inheritance to FALSE
355                 0,              // No creation flags
356                 NULL,           // Use parent's environment block
357                 NULL,           // Use parent's starting directory
358                 &(si),            // Pointer to STARTUPINFO structure
359                 &(pi) )           // Pointer to PROCESS_INFORMATION structure
```

```
360                     )
361             {
362                     printf( "CreateProcess failed (%d).\n", GetLastError() );
363             }
364
365             //turn off motor
366             CPhidgetAdvancedServo_setEngaged(servo, 0, 0);
367
368             //disconnect phidget control board
369             CPhidget_close((CPhidgetHandle)servo);
370             CPhidget_delete((CPhidgetHandle)servo);
371
372             //close session with GPIB device
373             iclose(id);
374
375             //let user check output
376             printf("\nDone.\a\a\a\a\n");
377             getchar();
378
379             return(0);
380     }
```

APPENDIX D

Imaging Programs

D.1. Acquisition

This program for Andor spectrometers collects hyperspectral images. The program waits for a TTL trigger pulse before collecting each spectrum. The language is Andor's proprietary variant of BASIC. The program maintains most instrument settings previously set by the user.

```
print("Area Miscroscopy Program")
start=time()
input("Enter the x step size in micrometers: ",xstepsize)
input("Enter the number of x spectrum sites: ",xsteps)
input("Enter the y step size in micrometers: ",ystepsize)
input("Enter the number of y spectrum sites: ",ysteps)
input("Enter experiment folder name: ",name$)
directory$="C:\Users\Public\automatic_data\"
SetTriggerMode(0) :rem Trigger mode for background only.
SetAcquisitionMode(1)
SetReadoutMode(0)
:rem 4 is full, 0 is fast binned data

SetDataType(2):rem Background corrected data type is 2

SetAcquisitionType(1):rem Background
key("To collect background, press a key")
```

```
18 run()
19 SetAcquisitionType(0):rem Signal
20
21 :rem y loop
22 j=0
23 key("To collect signal, press a key, then start stage script.")
24 while(j<ysteps)
25         j=j+1
26         i=0
27         :rem x loop
28         while(i<xsteps)
29                 i=i+1
30                 print("Waiting for trigger ",i)
31                 :rem Important
32                 SetTriggerMode(1)
33                 :rem 1=external 0=internal
34
35                 run()
36                 SetTriggerMode(0) :rem workaround for triggering bug
37                 run()
38
39                 :rem pad file names
40                 pad$=""
41                 if((len(str$(xsteps*ysteps))-len(str$(i+(j-1)*xsteps)))<0) then
42                         print("Filename padding error!")
43                 else
44                         while(len(pad$)<(len(str$(xsteps*ysteps))-len(str$(i+(j-1)*
                               xsteps))))
45                                 pad$=pad$+"0"
46                         wend
```

```
47                      endif
48
49                      filename$=directory$+name$+"\"+pad$+str$(i+(j-1)*xsteps)+"x"+str$((
                            i-1)*xstepsize)+"y"+str$((j-1)*ystepsize)+"t"+str$(time())
50                      print(filename$)
51                      save(#0,filename$+".sif")
52
53                      :rem Potentially slows us down because we write to disk twice.
54                      SaveAsciiXY(#0,filename$+".txt",2):rem tab separated value
55
56                      CloseWindow(#1)
57              wend
58  wend
59
60  CloseWindow(#0)
61
62  print("Done.  Saved data in ",directory$)
63  print("Total time required in seconds: ",time()-start)
```

D.2. Analysis

This program, written for R 3.0.3, shows in part how I reduced the data collected with the previous program. I avoided using the array paradigm typically found in R programming because of difficulty debugging nonlinear regressions.

```
1  library(Hmisc)
2  filelist=list.files("./",pattern="[0-9].txt"); #find all spectrum files in the
       working directory
3
4  range <- 454:586# set region of interest rows for phonon-linked luminescence
```

```
5  #regions of interest depend on wavelength center selected in spectrometer
6
7  data <- do.call(data.frame, lapply(filelist , function(x) read.table(x)[[2]][range])
       ); #read spectra
8  scale <- 1239.84193/read.table(filelist[[1]])[[1]][range]; #get wavelength scale
       from first file , convert to electron volts
9  xpos <- sub("y[0-9]*t[0-9]*.txt","",sub("[0-9]*x","",filelist)); #get x positions
10 ypos <- sub("t[0-9]*.txt","",sub("[0-9]*x[0-9]*y","",filelist)); #get y positions
11
12 #initial guess depends on temperature and exposure
13 initials <- list(amp=270000,center=2.018230,T=46)
14
15 prange <- 72:133#area where no polariton luminescence
16 roi <- 54:72 #area where the polariton line is 609.75 to 611 nm
17 total <- {} #integrated residuals
18 meanenergy <- {} #peak location
19 sdenergy <- {} #peak width
20 fits <- {}
21
22 for (i in 1 : dim(data)[2]){
23          print(i);
24          df<-data.frame(dscale=scale[prange],ddata=data[[i]][prange]);#apply region
               of interest for phonon fit
25          newdf=data.frame(dscale=scale[roi]);#for predicting values in polariton
               area
26
27         #perform regression of Maxwell-Boltzmann model
28         #Poisson weighting
```

```
29          model<-nls (ddata~ amp*sqrt(abs(dscale-center))*exp(-(dscale-center)/
                (8.6173323*10^(-5)*T)),data=df,weights=1/sqrt(Mod(ddata)+1),start=
                initials,nls.control(tol=6e-5));
30          fits<-cbind(fits,summary(model)$coefficients[1:3]);
31
32          #polariton analysis
33          total<-append(total,sum(data[[i]][roi]-predict(model,newdf))); #compute sum
                 of residuals
34          meanenergy<-append(meanenergy,
35                             wtd.mean(scale[roi],(data[[i]][roi]-predict(model,newdf))^2
                                  #residual square weights
36                            )
37                  ); #compute center of peak
38          sdenergy<-append(sdenergy,sqrt((wtd.var(scale[roi],(data[[i]][roi]-predict(
                model,newdf))^2)))); #compute width of peak
39  }
40
41  #save results
42  alldata <- rbind(xpos,ypos,fits,total,meanenergy,sdenergy);
43  write.table(t(alldata),"residual.gp",row.names=FALSE,col.names=c("#x position (
        microns)","y position (microns)","phonon amplitude (arbitrary)","phonon energy (
        eV)","temperature (K)","sum of residuals (aribtrary)","residual peak (eV)","
        peak width (eV)"),quote=FALSE)
```